Interzonal Air and Moisture Transport through Large Horizontal Openings: An Integrated Experimental and Numerical Study

Sergio Vera Araya

A Thesis

in the Department

of

Building, Civil and Environmental Engineering

Presented in Partial Fulfillment of the Requirements

for the Degree of Doctor of Philosophy (Building Engineering) at

Concordia University

Montreal, Quebec, Canada

April, 2009

ABSTRACT

Interzonal Air and Moisture Transport through Large Horizontal Openings:
An Integrated Experimental and Numerical Study

Sergio Vera Araya, Ph.D.

Concordia University 2009

In the current design and operation of residential houses, indoor humidity is often left unregulated because, unlike temperature, it is more difficult to sense, quantify, and control. High indoor RH may increase the risk of respiratory problems such as rhinitis and asthma, reduce perceived air quality, propitiate mold growth, and cause building damages. Low indoor RH may cause discomfort due to dryness of nose, eyes and skin.

Indoor humidity in each room of multizone buildings depends on the moisture generation by sources, moisture transport by air leakage and ventilation, moisture buffering by indoor finishing materials and furniture, moisture transport through the envelope, and moisture transport between rooms due to interzonal airflows. Most of these aspects have been extensively studied, but the moisture transport due to interzonal airflows through doorways or staircase openings has received less attention.

The aim of this investigation is to study the interzonal air and moisture transport through a large horizontal opening in a full-scale two-story test-hut involving buoyancy-driven flows (due to temperature differences only) and combined buoyancy and forced airflows (due to mechanical ventilation). To accomplish this objective, experiments and Computational Fluid Dynamics (CFD) simulations are performed. The main parameters tested are the temperature difference between the lower and the upper rooms, ventilation strategies, ventilation rates and locations of the moisture source.

Interzonal moisture exchange and interzonal airflows are analyzed based on two quantities that represent both phenomena, the difference between the average humidity

ratios of the two rooms and the interzonal mass airflows, respectively. Experimental and CFD simulation results show that higher interzonal mass airflows and moisture exchanges through the horizontal opening are found when the upper room is colder than the lower room, while lower interzonal mass airflows and moisture exchanges occur when the upper room is warmer. Also, it is shown that the mechanical ventilation significantly restricts interzonal mass airflows in comparison with cases without ventilation. Based on CFD results, empirical equations representing the upward mass airflow through the horizontal opening are developed at different ventilation rates and ventilation strategies.

To my beloved wife,
Gabriela.

ACKNOWLEDGEMENTS

Building Envelope Laboratory and gave me the opportunity to finish the experimental investigation.

TABLE OF CONTENTS

LIST OF FIGURES

LIST OF TABLES

LIST OF ACRONYMS AND SYMBOLS

List of Acronyms

ACH   Air Change per Hour

CFD   Computational Fluid Dynamics

DAS   Data Acquisition System

HAM   Heat, Air and Moisture

HR   Humidity Ratio

RH   Relative Humidity

RTD   Resistance Temperature Detector

UDS   Upwind Differencing Scheme

English symbols

A Area (m^2)

c_p Specific heat capacity at constant pressure (J/kg°K)

D Diameter of the opening (m)

D_v Diffusion coefficient of the water vapor (m^2/s)

Dif Mass flow rate due to diffusion across the envelope (kg/s)

F Mass airflow rates (kg/s)

$\bar{F}$ Measured average mass airflow rates through the horizontal opening (kg/s)

$\bar{F}^e$ Average mass airflow rates through the horizontal opening estimated from the measured average air speed across the opening (kg/s)

F_{12} Upward mass airflow through the horizontal openings (kg/s)

F_{21} Downward mass airflow through the horizontal openings (kg/s)

g Acceleration due to gravity (m/s^2)

G Moisture generation rate (kg/s)

H Thickness of the horizontal opening (m)

l Length scale to calculate turbulent viscosity (m)

L Air leakage rate (kg/s)

m_v Water vapor flow through the horizontal opening due to diffusion (kg/s)

M_c Combined permeance of the east and west walls (kg/s·m^2·Pa)

p Pressure (Pa)

P	Atmospheric pressure at sea level (Pa)
Pr	Prandtl number
p_{sat}	Vapor saturation pressure (Pa)
$p_{sat,s}$	Vapor saturation pressure at surfaces (Pa)
p_v	Partial water vapor pressure (Pa)
$p_{v,s}$	Partial water vapor pressure at surfaces (Pa)
Q	Volumetric airflow rate (m³/s)
S_C	Source term for concentration in Navier-Stokes equations (kg/m³s)
Sc	Schmidt number
S_q	Thermal source term in Navier-Stokes equations (W/m³)
S_ϕ	Source or sink term of variable ϕ in Navier-Stokes equations
t	Time (s)
T	Temperature (°K)
$\bar{T}$	Mean temperature of the lower and the upper rooms (°K)
u	Standard uncertainty
u_c	Combined uncertainty
U	Expanded uncertainty
V	Air or room volume (m³)
V_i, V_j	Mean velocity component in the x_i or x_j direction (i, j = 1, 2 and 3)
V_z	Velocity component in the z direction at the middle plane of the horizontal opening (m/s)
$\bar{V}$	Mean air speed (m/s)
$\bar{V}_{opening}$	Measured average air speed across the horizontal opening by omnidirectional anemometers (m/s)
w	Humidity ratio (kg/kg)

Greek symbols

β	Thermal expansion coefficient (1/°K)
β_v	Surface film coefficient for water vapor (kg/Pa·m²·s)
Γ_ϕ	Diffusion coefficient term of variable ϕ in the Navier-Stokes equations
ΔHR	Difference between the average humidity ratios of the two rooms (g/kg or kg/kg)

$\Delta\rho$	Density difference between the two compartments (kg/m^3)
ΔT	Temperature difference between the lower and the upper rooms (°C). ΔT is negative when the upper room is warmer than the lower room, while ΔT is positive when the upper room is colder than the lower room.
μ	Laminar or molecular viscosity (Pa·s)
μ_{eff}	Effective viscosity (Pa·s)
μ_t	Turbulent viscosity (Pa·s)
ρ	Fluid density (kg/m^3)
$\bar{\rho}$	Mean density of the lower and the upper compartments (kg/m^3)
τ	Duration of moisture generation period (s)

Subscripts

a	Air
c	Environmental chamber
i	Room or cell i
i, j	Room or cell j
o	Outdoor
$1e, 2e$	Exhaust air of the lower room, the upper room
$i1, i2$	Supply air of the lower room, the upper room
1	Lower room
2	Upper room

CHAPTER 1

INTRODUCTION

1.1 Importance of indoor humidity in buildings

In the current design and operation of residential houses, indoor humidity is often left unregulated because, unlike temperature, it is more difficult to sense, quantify, and control. Therefore, relative humidity (RH) can fluctuate significantly in indoor environments. For example, RH above 80% can be found in highly airtight dwellings with low ventilation rates and high occupancy. On the other hand, combined low outdoor humidity and overheating in winter season can decrease RH to as low as 20% or less in cold climates. High indoor RH (> 50%) and low indoor RH (< 20% - 30%) may impact negatively human comfort and health, indoor air quality, building durability and energy consumption. The influence of indoor humidity on some of these aspects and acceptable humidity levels are reviewed below.

1.1.1 Human comfort

Thermal comfort, one of the main aspects associated to human comfort, is not influenced by indoor RH between 30% and 70% because humidity is difficult to sense since humans do not posses sensors for RH. For this reason ANSI/ASHRAE Standard 55, *Thermal Environmental Conditions for Human Occupancy* (ASHRAE, 2004), allow a very wide range for the operative humidity level to meet thermal comfort requirements. Figure 1.1 shows the operative temperature and humidity ranges for spaces with air speed lower than 0.2 m/s according to ANSI/ASHRAE Standard 55. It can be observed that only the upper humidity limit is specified to be 0.012 kg/kg, which corresponds to a maximum RH of 86% in winter and 67% in summer. In contrast, ANSI/ASHRAE Standard 55 does not establish a minimum humidity level.

1
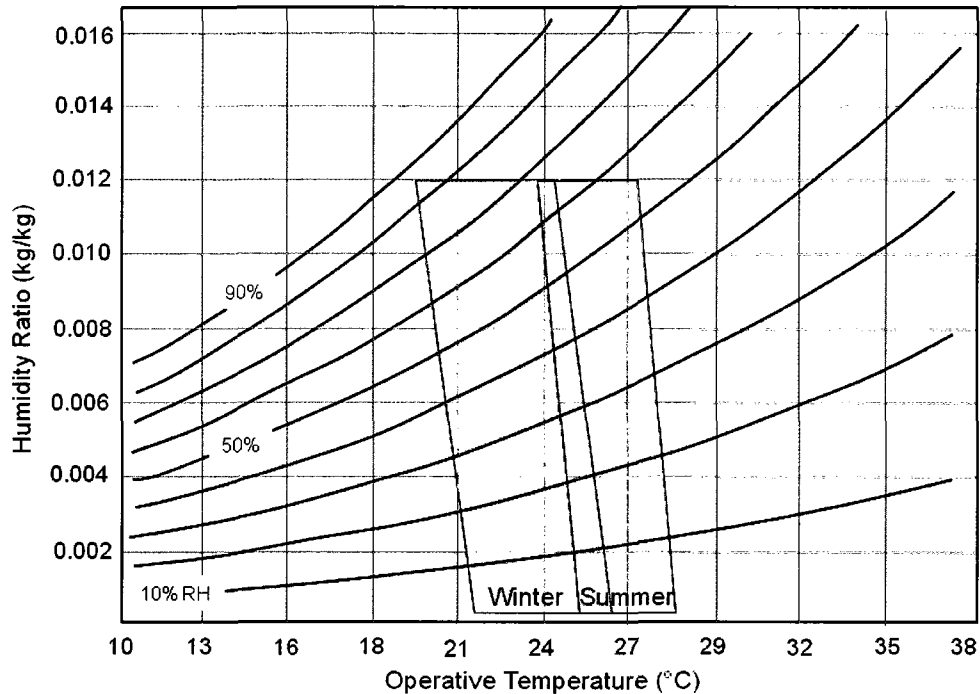
Figure 1.1: Acceptable range of operative temperature and humidity for winter and summer conditions (ASHRAE, 2004).

Although RH does not influence significantly thermal comfort, other aspects of human comfort may be influenced negatively by very low or high RHs. At one end, very low humidity causes discomfort due to dry noses, eyes and skin. Green (1982) found that absenteeism in schools increased because of these symptoms due to low indoor humidity in winter, and correspondingly absenteeism decreased as these low indoor humidity levels increased. Similarly, Reinikainen et al. (1991) found that complaints about dryness of skin, throat and nose, nasal obstruction and sensation of air dryness from office workers in rooms with humidification were significantly less in comparison with the complaints of workers in similar rooms without humidification. At the other end, high humidity may cause discomfort due to high level of skin humidity at higher air temperatures (Berglund and Cunningham, 1986) and due to the inhalation of humid and warm air (Toftum et al., 1998).

1.1.2 Occupant's health and indoor air quality

Several epidemiological population studies have been carried out to analyze the relationship between dampness in buildings and health problems. Review studies done by Bornehag et al. (2001, 2004) have shown that moisture in buildings increases the risk of health problems such as cough, wheeze and asthma. Also based on a literature review, Davies et al. (2004) concluded that a link exists between moisture related respiratory hazards, such as house dust mites and mold, with respiratory problems such as asthma and rhinitis.

Arundel et al. (1986) found that the optimum RH ranges between 40% and 60% (Figure 1.2). In this range, the growth and spread of pathogens (e.g. bacteria, viruses) are reduced, accompanied by a reduction of respiratory infections. Figure 1.2 also shows that fungi and dust mites do not proliferate below 60% RH, which reduces the respiratory problems associated with mold and house dust mites.
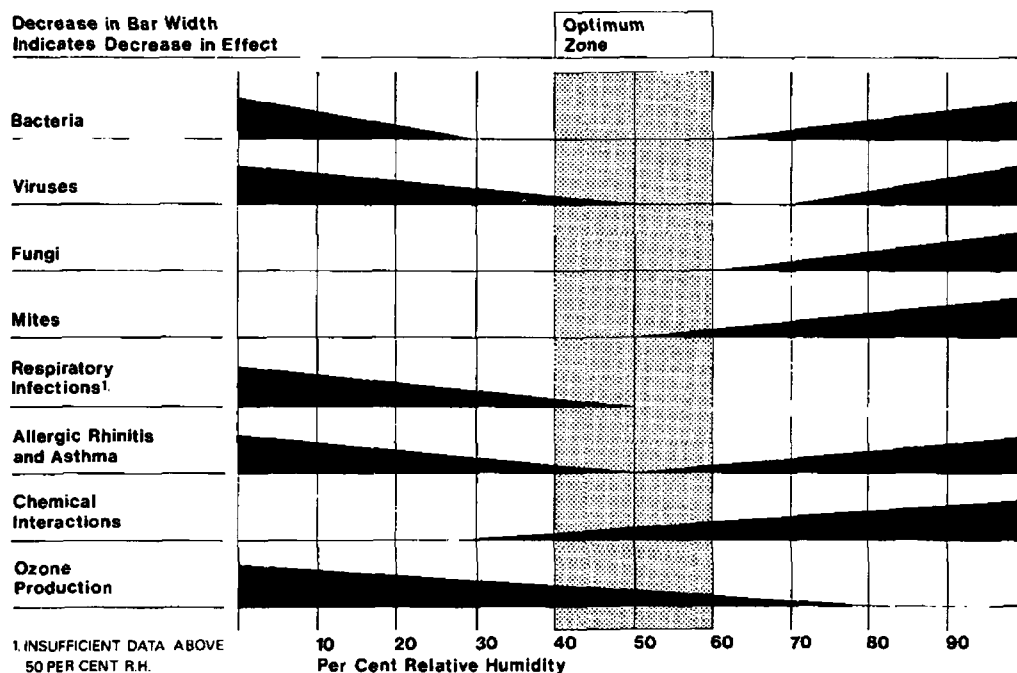
Figure 1.2: Effect of RH on health problems (Arundel et al., 1986).

Additionally, RH influences indoor air quality in several ways. High RH promotes off-gassing of volatile organic compounds present in building products. For example, off-gassing of formaldehyde found in plywood, paper and wood products, textiles and carpets may result in the irritation of skin and respiratory track (Arundel et al., 1986). Also, RH influences the perceived air quality. Fang et al. (1998a) studied the influence of temperature and RH on the perceived air quality for face exposure. They found that the temperature and RH had significant impact on the perceived air quality at any air pollution level, and at constant pollution level, the perceived air quality decreased with increasing air temperature and RH. Similar results were found for whole-body exposure (Fang et al., 1998b) as shown in Figure 1.3.
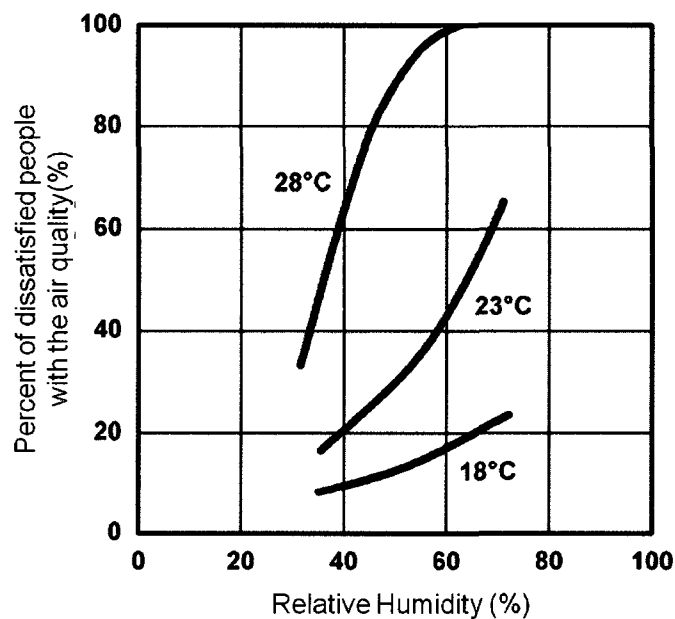
Figure 1.3: Influence of temperature and RH on perceived air quality (Fang et al.,1998b).

1.1.3 Building durability

Indoor moisture can migrate by diffusion and convection as vapor through the envelope, which can cause severe damage when moisture accumulates, especially in cold climates (Trechsel, 1994). Although, the main moisture related problems are mold growth, frost damage, steel corrosion, wood decay and aesthetical problems, structural

4

damage can also occur due to high indoor RH (Merrill and TenWolde, 1989). Figure 1.4 shows significant damages caused by higher indoor RH in steel stud rain screen walls without vapor barrier in condominiums in Vancouver (Finch, 2007). Additionally, high indoor RH in microclimates can cause aesthetical damages on indoor surfaces such as moisture stains, fungal attack and deterioration of finishing materials (e.g. paint, wall paper).
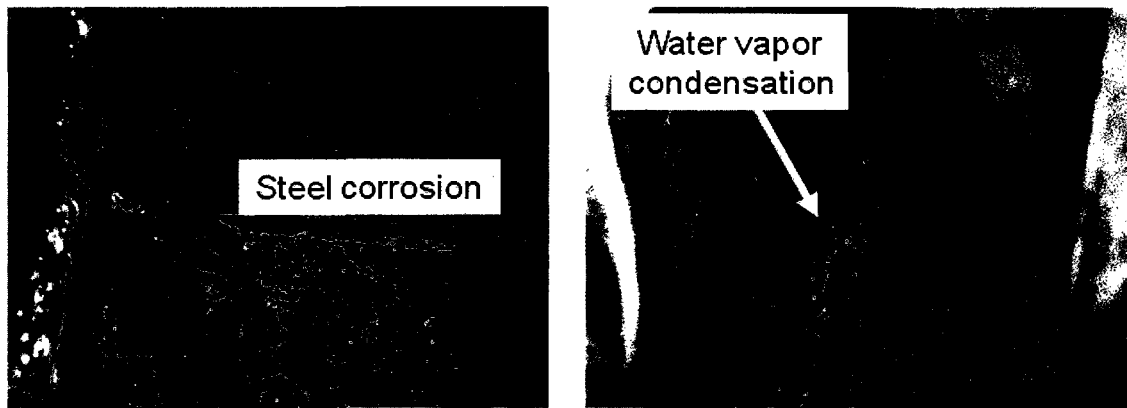
Figure 1.4: Damages reported in the steel-stud cavity (Finch, 2007).

RH higher than 80% provides excellent conditions for mold growth (Hukka and Viitanen, 1999). This problem can be found in a significant portion of dwellings. For example, a study carried out in 1,095 houses in England showed that above 40% of the houses surveyed had significant mold when "the standardized indoor RH" was above 80% (Oreszczyn et al., 2006). Since mold growth problems are mainly related to high RH on surfaces, several studies, such as TenWolde (1994), HUD (2004) and Oreszczyn et al. (2006), show that this problem occurs at indoor RH between 40% and 50% measured in the center of the rooms.

1.1.4 Energy consumption

Moisture is important in energy analysis and its influence is most significant in warm moist regions, where the latent load represents up to over 50% of the annual cooling load. Here, mechanical ventilation and cooling are the most common methods to

control indoor humidity. However, mechanical ventilation influences the energy consumption, and cooling is very energy intensive. For instances, Simonson (2000) indicates that "ideal cooling of air from 30°C and 60% RH to 25°C and 50% RH requires over 4 times as much energy as cooling air from 30°C to 25°C with no change in moisture level".

1.2 Whole-building HAM balance

The RH in a space (zone or room) is the result of the whole-building heat, air and moisture (HAM) balance, which depends on the moisture transport mechanism and moisture sources/sinks shown in Figure 1.5. This moisture balance can be expressed by Eq. 1.1 (adapted from Hens, 2005). The term on the left side represents the variation of the total moisture mass in the room air expressed in terms of humidity ratio[1], w.

$$\underbrace{\rho_a V \frac{dw_i}{dt}}_{\substack{\text{Variation} \\ \text{of indoor} \\ \text{humidity}}} = G + \underbrace{\left(w_o F_{o,i} - w_i F_{i,o}\right)}_{\substack{\text{Moisture exchange} \\ \text{with the exterior due} \\ \text{to infiltration}}} + \underbrace{\sum_{n=1}^{p} \beta_{v,n}\left(p_{v,s_n} - p_{v_i}\right)A_n}_{\substack{\text{Moisture absorption/} \\ \text{desorption of "}n\text{"} \\ \text{surfaces and furniture}}} +$$

where the braces under G read "Water vapor sources and sinks".

(1.1)

$$\underbrace{\sum_{m=1}^{q} \beta_{v,m}\left(p_{sat,s_m} - p_{v_i}\right)A_m}_{\substack{\text{Surface} \\ \text{condensation and} \\ \text{evaporation in "}m\text{"} \\ \text{surfaces}}} + \underbrace{\left(\sum_{j=1}^{k} w_j F_{j,i} - w_i \sum_{j=1}^{k} F_{i,j}\right)}_{\substack{\text{Moisture exchange} \\ \text{between adjacent} \\ \text{rooms}}}$$

where w is the humidity ratio (kg/kg), ρ_a is the air density (kg/m^3), V is the volume of the room (m^3), p_v is the partial water vapor pressure (Pa), $p_{v,s}$ is the partial water vapor pressure at surfaces (Pa), $p_{sat,s}$ is the vapor saturation pressure at surfaces (Pa), A is

---

[1] Humidity ratio is defined as the ratio between the mass of water vapor and the mass of dry air.

the surface area (m^2), G is the vapor generation rate from moisture sources (kg/s), β_v is the surface film coefficient for water vapor transfer (kg/Pa·m^2·s), and F is the mass airflow (kg/s).
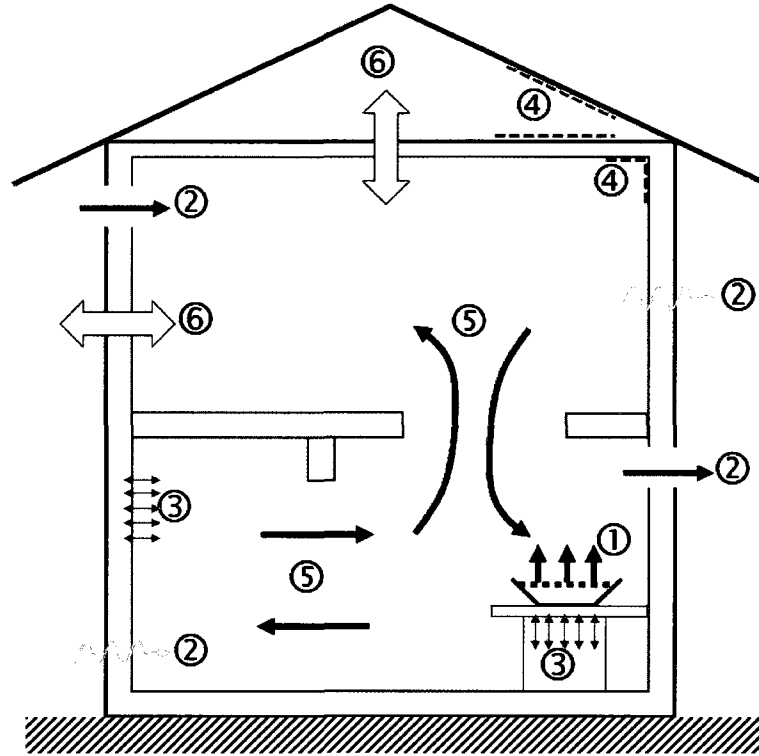
Figure 1.5: Schematic representation of moisture flows, sources and sinks.

The first term on the right-hand side of Eq. 1.1 is the water vapor generation (① in Figure 1.5) in the room by occupant's activities (e.g. cooking, bathing, breathing, washing). This term can also represent moisture sinks in the room. In dwellings, moisture generation by occupancy is the main indoor moisture load when rain penetration is well controlled. IEA Annex 14, *Energy and Condensation*, showed that the moisture generated in a house is 4.3 kg/day and 13.7 kg/day for a family of two and four, respectively (Hens, 1991). More recently, Kalamees et al. (2006) studied the moisture production in Norwegian detached houses during winter. They found that moisture production fluctuated between 1 and 14 kg/day (Figure 1.6), which is consistent with values presented by Hens (1991). It can be observed in Figure 1.6 that higher moisture

production occurs during the nighttime and decreases after people leave the houses at around 8 AM. Moisture production increases in the evening when people return to their homes.
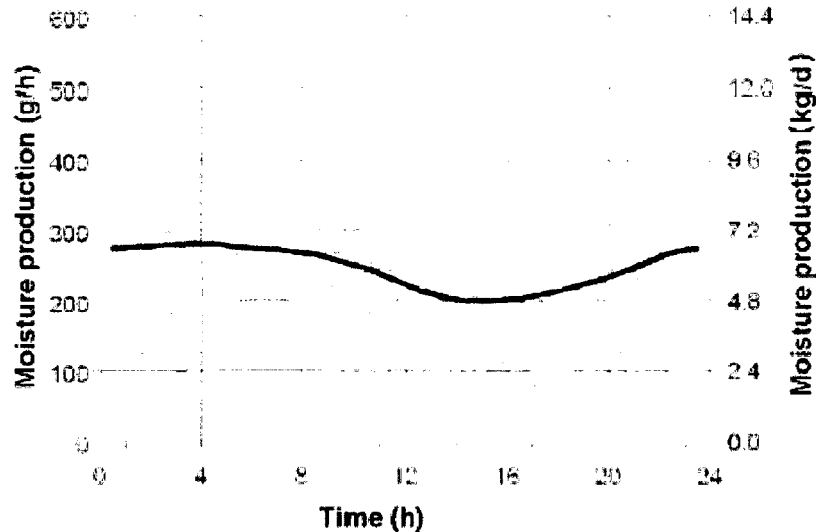
Figure 1.6: Moisture production measured in detached houses in Norway during winter (Kalamees et al, 2006).

The second term on the right-hand side of Eq. 1.1 corresponds to the moisture exchange with the exterior by air infiltration/exfiltration and ventilation (② in Figure 1.5). Infiltration can be significant in old houses, but after the oil crisis in the 1970s, houses have become more airtight to reduce energy consumption. Ventilation is the main mechanism to remove moisture from indoor spaces. Usually, mechanical ventilation in houses provides inlet air in the living rooms and bedrooms and exhaust vents in the kitchen and bathroom zones. Huang et al. (2004) indicates that low air change rates between 0.3 and 0.8 ACH can be reached considering the construction techniques used nowadays in cold climate countries. TenWolde (1994) found that manufactured houses have air change rates lower than the 0.3 ACH recommended by standards.

The third term on the right-hand side of Eq. 1.1 represents the moisture absorption/desorption by building materials and furnishing (③ in Figure 1.5). Indoor finishing materials and furnishing can absorb moisture when relative humidity increases,

8

and release it when the air dries again. This mechanism is known as moisture buffering and can have significant impact on indoor RH due to the high amount of water vapor that can be absorbed by certain finishing materials and furniture. For example, Plathner and Woloszyn (2002) reported that more than one third of the airborne moisture is absorbed by indoor surfaces.

The fourth term on the right-hand side of Eq. 1.1 corresponds to moisture sinks and sources due to surface condensation and drying processes, respectively (④ in Figure 1.5). For instances, condensation was the main aspect studied in IEA Annex 14, *Energy and Condensation*; and Hohota (2003) and Liu et al. (2004) evaluated surface condensation experimentally and numerically in test rooms.

Finally, the last term on the right-hand side of Eq. 1.1 stands for the interzonal moisture transport between connected zones through large openings, such as doorways and staircase openings (⑤ in Figure 1.5). The interzonal moisture transport depends on the airflows through these openings. Moisture transport through doorways and staircases allows the moisture exchange between connected zones. Moisture is spread from the moisture source across the entire room where the moisture source is placed, and from here, moisture is transported to other rooms through vertical and horizontal openings that connect different zones of the building. This phenomenon helps moisture migration from the moisture-source room to other rooms, influencing the indoor RH not only in the moisture-source room but also in the rest of the house.

Figure 1.5 also shows the moisture transport through the envelope by diffusion and convection (⑥ in Figure 1.5). In most of cold climate countries the use of vapor barriers and air barriers are required to control this moisture migration. Several models and experimental work have been carried out to study the HAM transport at material and enclosure levels. Although this moisture flow mechanism does not appear explicitly in Eq. 1.1, the air, moisture and energy balances in the envelope provide the surface

temperatures and related partial and saturation vapor pressures at surfaces shown in Eq. 1.1.

1.3 Whole-building HAM research focus

Most of the moisture transport mechanism and sources/sinks showed in Eq. 1.1 and Figure 1.5 have been and are being studied extensively. IEA Annex 14, *Condensation and Energy* (Hens, 1991), includes detailed information on moisture sources and vapor production rates in rooms. Most recently, several studies have measured indoor conditions in hundreds of houses in Europe to get a better understanding of the actual indoor conditions in dwellings (Oreszczyn et al., 2006; Janssen and Vandepitte, 2006; Kalamees et al., 2006; Ridley et al., 2007). Also, IEA Annex 14 addressed moisture related problems such as surface condensation and mold growth, and there are many studies focused on mold growth and its spread, on the evaluation of indoor conditions related to this problem, and on the building durability problems associated with it. The most recent review of these aspects was carried out by Holm (2008) in Volume 4 of IEA Annex 41, *Applications – Indoor environment, Energy, Durability*.

The study of HAM transfer through the envelope has been investigated extensively in the last two decades by means of experimental and modeling studies (Rode, 1990; Hens, 1996; Treschel, 2001; Haghentoft, 2002). Several simulations tools of the HAM transfer through envelopes have been developed such as MOIST (Burch and Chi, 1997), LATENITE (Salonvaara and Kariagozis, 1994), WUFI (Kuenzel et al., 2001) and hygIRC (Maref et al., 2003). These tools consider the indoor humidity as a fix input, thus the indoor humidity variation is not predicted.

Since Tscuchiya in 1980, several studies (e.g. Hens, 1991; Cunningham, 1992; Padfield, 1998) have proved that moisture absorption/desorption by indoor finishing

surfaces and furniture may significantly influence indoor humidity. Most recently, IEA Annex 41, *Whole Building Heat, Air and Moisture Response* (ECBCS, 2008) has consolidated and expanded the study of the moisture interactions between indoor air and building constructions. This IEA Annex has concluded with a better understanding of the influence of moisture buffering on indoor humidity via experimental investigations, measurement of associated material properties, and the development and validation of simple and advanced modelling tools that take into account this phenomenon.

Furthermore, IEA Annex 41 has prompted significant developments in the modeling of the whole-building HAM response and its validation. Unlike HAM simulation tools that are focused on the hygrothermal performance of the envelope, new generation simulation tools let the indoor humidity floating. Thus predictions of the indoor humidity are the results of the whole-building HAM balance. Some of these simulation tools are WUFI+ (Holm et al., 2003), BSim (Rode and Grau, 2003) and PowerDomus (Mendes et al., 2003). These types of models are being called whole-building HAM models (Woloszyn and Rode, 2008).

1.4 Problem statement

It can be seen from the previous section that most of the factors that influence the indoor humidity level have been and are being studied extensively by means of experimental works and were implemented in simulation tools. However, the interzonal moisture transport through large openings is absent in the previous studies in terms of experimental and modeling investigations. Most of the whole-building HAM models are one zone models, thus they do not include interzonal moisture transport. However, in more realistic conditions such as in multizone buildings, this moisture transport mechanism must be considered since the air humidity behavior of room i is dependent on the air moisture conditions in adjacent rooms as shown in Eq. 1.1. The airflow rates

across the flow paths connecting adjacent rooms or zones (e.g. doorways, staircase openings) are the main factors that influence the whole-building air humidity response and the degree of interaction between the different building spaces. Therefore, to predict the indoor humidity variation in each room, the airflow rates through these large openings have to be known.

The airflows across vertical openings (e.g. doorways, windows) are a relatively well known phenomenon and have been studied extensively (e.g. Brown and Solvason, 1962; Shaw, 1972; Shaw and White, 1974; Barakat, 1987; Riffat, 1989; Allard and Utsumi, 1992; van der Mass, 1992; Riffat and Kohal, 1994; Santamouris et al., 1995). Empirical equations for the airflow through vertical openings have been developed and have been integrated in simulation tools to account for the moisture carried by interzonal airflows to predict indoor humidity level in rooms. For example, El Diasty et al. (1993) studied the air humidity behavior in a multizone building with vertical openings. They included into their numerical model the flow equation through vertical openings derived by Brown and Solvason (1962) to account for the interzonal moisture transport.

Unlike the extensive studies of interzonal airflows through vertical openings, very few studies have been carried out for the airflow through horizontal openings, and most of them only considered buoyancy-driven flows through horizontal opening (e.g. Brown, 1962; Epstein, 1988; Riffat et al. 1994; Peppes et al., 2001; Blomqvist and Sandberg, 2004; Li, 2007). Some of these studies have derived empirical equations for the airflow through the opening. Furthermore, only one study (Klobut and Sirén, 1994) has been carried out with combined buoyancy and forced flow through horizontal openings, and no empirical equations were derived for the airflow rate through the opening under this condition. Empirical equations representing the airflow through horizontal openings are essential to predict indoor humidity variations in multizone buildings. Good prediction of indoor humidity is crucial for the assessment of indoor air quality, mold growth, surface

condensation, and moisture buffering of indoor finishing materials and furniture. Moreover, indoor humidity is one of the boundary conditions for HAM transfer through envelopes, thus better understanding and predictions of indoor humidity may lead also to better predictions of the hygrothermal performance of building enclosures.

Therefore, experimental studies considering more realistic conditions such as mixed ventilation are needed. Experimental data with air and moisture transport through horizontal openings not only contributes to the better understanding of the transport mechanism of this phenomenon, but also they are essential to validate indoor humidity predictions by means of whole-building HAM models.

1.5 Research objectives and methodology

The overall aim of this research is to study the interzonal air and moisture transport through a large horizontal opening in a full-scale two-story test-hut involving buoyancy-driven flows only and combined buoyancy and forced driven flows. The specific objectives of this investigation are:

i. Evaluate the impact of temperature differences between two rooms connected by a large horizontal opening, ventilation strategies, locations of moisture source and ventilation rates on the interzonal air and moisture transport through the horizontal opening.

ii. Develop empirical correlations representing the airflow through the horizontal opening for cases with buoyancy-driven flows only and cases with combined buoyancy and forced driven flows, which may be implemented in whole-building HAM models to predict indoor humidity variations in multizone buildings.

iii. Study the capabilities of the indoor zero-equation model (Chen and Xu, 1998)

13

implemented in a commercial Computational Fluid Dynamics[2] (CFD) simulation package, Airpak, to model the interzonal air and moisture transport through horizontal opening under steady-state conditions.

iv. Generate datasets with extensive experimental results that allow other researchers to validate ongoing and future developments of multizone whole-building HAM models to improve predictions of indoor humidity in multizone buildings.

This thesis research is carried out by means of experiments and CFD simulations. The experimental study, the major investigation work carried out in this thesis research, is performed in a full-scale test-hut consisting of two rooms connected by a large horizontal opening. The two-story test-hut is built inside the Environmental Chamber at Concordia University. Here, the air speed, temperature and humidity ratio (herein abbreviated as HR) across both rooms and at the opening are measured for different test conditions. Also, boundary conditions such as wall surface temperatures, ventilation flow rates and air conditions of the supply air and exhaust air are monitored. The main parameters tested include the temperature difference between the lower and the upper rooms that ranges from -2.7°C to +3.5°C (negative temperature differences mean that the upper room is warmer than the lower room, while positive temperature differences mean that the upper room is colder than the lower room); ventilation strategies (no ventilation, single ventilation with downward net flow through the opening, and independent ventilation in each room); ventilation rates (0.3 ACH, 0. 5 ACH, and 0.75 ACH); and locations of the moisture source (lower room or upper room). From the experimental data, the moisture exchanges and interzonal airflows through the horizontal opening are studied by means of two physical quantities that represent these phenomena: (*i*) the steady-state difference between the average humidity ratios of the

---

[2] A CFD model is a computer-based model that can predict the air movement, temperature and contaminant distribution, as well as many other parameters of air distribution (Axley and Nielsen, 2008).

two rooms, and (*ii*) the measured interzonal mass airflow through the horizontal opening. Both quantities are defined in *Chapter 5*.

The numerical study via CFD simulations complements the experimental results. The numerical study consists, first, in validating the CFD model with the measured air speeds, temperatures and HRs across the two-story and at the opening, and with measured interzonal mass airflows for some cases tested with mechanical ventilation. Once the CFD model is validated, it is used to investigate additional scenarios and to provide detailed spatial data for the analysis of the velocity field across the opening and the influence of the ventilation rates on interzonal mass airflow and moisture exchanges.

1.6 Outline of this thesis

Chapters 2 and *3* present the literature surveys. Since interzonal airflows carry the moisture along large internal air paths, *Chapter 2* reviews the main studies on interzonal airflow through horizontal openings. The review reveals that few experimental and numerical studies have been carried out to study this phenomenon. Moreover, the few existing studies consider buoyancy-driven flows only, which is not realistic in buildings because forced flows due to mechanical ventilation and wind also occur in buildings. *Chapter 3* reviews CFD fundamentals and how this technique has been used to study interzonal airflow through horizontal openings and moisture distribution in rooms. Also, this chapter provides details of the indoor zero-equation turbulence model used in the CFD model, and reviews the application of this turbulence model to study airflow and distribution of temperature and species (e.g. water vapor, pollutants) in indoor environment.

Chapter 4 provides a detailed description of the experimental setup, including the envelope components of the two-story test-hut, sensor specifications, monitoring and

data acquisition system, measurement uncertainty analyses, and cases tested and test conditions.

Chapter 5 presents the experimental results in terms of the steady-state difference between the average humidity ratios of the two rooms, which represents the moisture exchange between the two rooms, and in terms of the measured interzonal mass airflows. Results are presented and analyzed for a total of 20 cases tested.

Chapter 6 focuses on the CFD modeling and its validation. First, this chapter describes the main aspects of modeling the two-story test-hut, and the airflow pattern and the distributions of temperature and humidity in the test-hut with Airpak, version 3.012 (Fluent, 2007). Then, a detailed validation of the CFD model for some experimental cases tested with combined buoyancy and forced driven flows is provided. This validation is performed by comparing the predicted and measured air speeds, temperatures and HRs in both rooms and at the opening, and by comparing the computed interzonal mass airflows with those estimated from experimental data.

Chapter 7 presents the results for the extended scenarios that were simulated in Airpak. Especially, additional ventilation rates and temperature differences between the two rooms are simulated. The CFD simulations allow visualizing the airflow pattern and distribution of temperature and humidity across the two rooms and at the opening, and obtaining the interzonal mass airflow through the opening. The influences of the temperature differences between the two rooms, ventilation rates and ventilation strategies on the interzonal air and moisture exchange are analyzed too. Also, from the CFD results, equations representing the mass airflow through horizontal openings are developed for combined buoyancy and forced driven flows at different ventilation rates.

Finally, *Chapter 8* draws the main conclusions and contributions obtained in this thesis; some suggestions for future work are also addressed.

CHAPTER 2

REVIEW OF INTERZONAL AIR AND MOISTURE FLOW THROUGH HORIZONTAL OPENINGS

2.1 Introduction

The airflow through large vertical openings, such as doorways, is a well understood phenomenon. Subtask 2 of IEA Annex 20, *Air flow through large openings in buildings*, brought together researchers from 5 countries that investigated experimentally and numerically the interzonal airflow though doorways and windows (van der Mass, 1992). In the case of vertical openings, the pressure difference between both sides of the opening causes a well known velocity distribution along the opening as shown in Figure 2.1. Figure 2.1a shows the case representing basic gravitational flows through vertical openings. This case involves only buoyancy-driven flows. On the other hand, Figure 2.1b shows the case with supply air in one zone, thus forced driven flows also exist. Several empirical equations for the airflow through vertical openings have been derived since Brown and Solvason in 1962, and good reviews of these equations have been carried out by Barakat (1987), Allard and Utsumi (1992) and Santamouris et al. (1995).
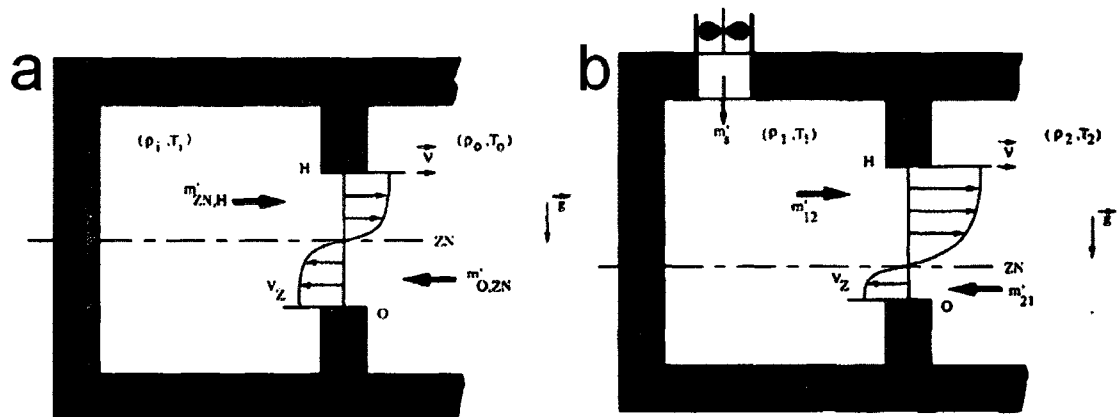
Figure 2.1: Velocity distribution through vertical openings: a) basic gravitational flow, and b) coupling with supply air in one zone (Allard and Utsumi, 1992).

Unlike the airflow through vertical openings, the airflow through horizontal opening still needs to be well understood. Since moisture is carried by the interzonal airflows through horizontal openings in multizone buildings, good understanding of that airflow is crucial to predict the humidity level and moisture distribution in each building zone. Only a few investigations have studied the airflow through stairwells and horizontal openings, which are reviewed later in this chapter. Furthermore, most of these studies only included buoyancy-driven flows, in which the upward and downward airflow rates through the opening are equal. In these cases, the pressure across the opening is constant and the pressure difference between both sides of the horizontal opening is zero. Therefore, theoretically there is no driving force for the interzonal airflows. However, warmer and lighter air under colder and heavier air is inherently unstable (Brown, 1962), thus air velocity is randomly distributed in the opening plane (Blomqvist and Sandberg, 2004) and highly transient and unstable air exchange between the two sides of the opening occurs (Riffat and Shao, 1995; Li, 2007).

In more complex situations, mechanical ventilation and wind may induce pressure differences between both sides of the horizontal opening that may cause net flow through the opening. Only one of the experimental studies, carried out by Klobut and Sirén (1994), investigated the flow through horizontal openings with combined buoyancy and forced driven flows. They imposed a net flow through horizontal openings by means of mechanical ventilation in a small two-compartment setup. Consequently, it can be seen that the interzonal air and moisture exchange through horizontal openings with combined buoyancy and forced driven flows is not well-known and further investigation is needed.

This chapter reviews the experimental investigations of the airflow through horizontal openings and in stairwells. These investigations have included a large diversity of experimental setups, such as scale-model tests or full scale-tests; stairwells

18

or horizontal openings dividing two floors; small opening or large horizontal openings; and the use of water or air as fluid. Additionally, this chapter reviews two experiments that studied the interzonal moisture transport in a two-story and three-story houses.

2.2 Interzonal airflow through horizontal openings

When buoyancy-driven flows (or natural convection) exist due to temperature differences between floors, equal upward and downward mass airflows through horizontal openings are found. Thus, the net flow through the opening is zero (Figure 2.2a). All studies considering this condition have been carried out with warmer or lighter fluid in the lower zone and colder or heavier fluid in the upper zone. The studies found in the literature have been carried out in small two-compartment setups, in one-half scale models of a stairwell, and in full-scale setups.

$$F_{12} = F_{21} \qquad F_N = F_{21} - F_{12}$$
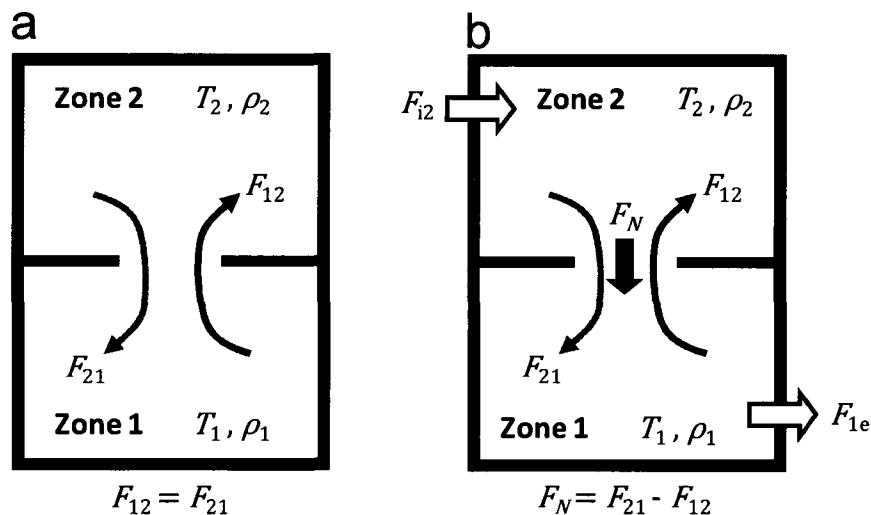
Figure 2.2: Illustration of the airflow through horizontal openings: a) pure buoyancy-driven flows, and b) combined buoyancy and forced flows.

On the other hand, when mechanical ventilation and wind are also involved, combined buoyancy and forced flows (or mixed ventilation) are present, and a net flow through horizontal openings may exist, as shown in Figure 2.2b.

2.2.1 Review of studies carried out in small two-compartments setups

The earliest studies of buoyancy-driven flows through horizontal openings were carried out in small two-compartment setups using air or water as fluid. The first study was carried out by Brown (1962), who studied buoyancy-driven flows through small square horizontal openings using air as fluid. Tests were carried out in a small apparatus with two compartments of 0.9 m^3 each connected by a square opening. The opening side ranged from 15 cm to 30 cm; the thickness of the opening (H) varied from 2.5 cm to 20 cm; and the temperature differences across the opening ranged from 11°C to 50°C. Brown interpreted the air exchange between both sides of the opening as a heat transfer phenomenon.

Epstein (1988) carried out a test in a small apparatus with two-compartment connected by a small circular horizontal opening. Brine (heavier fluid) in the upper compartment and water (lighter fluid) in the lower compartment were used to induce density-driven exchange flows. Epstein carried out tests in which the average density difference ratio ($\Delta\rho/\bar{\rho}$) ranged from 0.024 to 0.17, and the aspect ratios between the opening thickness and the opening diameter (H/D) varied from 0.01 to 10. Epstein found that the volumetric flow rate was given by the following equation:

$$Q = f(H/D)\sqrt{D^5 g \Delta\rho/\bar{\rho}} \qquad (2.1)$$

where Q is the volumetric flow rate (m^3/s), H is the opening thickness (m), D is the opening diameter (m), g is the acceleration due to gravity (m/s^2), $\Delta\rho$ is the density difference between the two compartments (kg/m^3), and $\bar{\rho}$ is the mean density of the two compartments (kg/m^3).

Figure 2.3 shows the experimental results found by Epstein and the lines represent Eq. 2.1. Epstein found four typical flow regimes characterized by a specific function $f(H/D)$: (*i*) oscillatory exchange flow (Regime I), (*ii*) Bernoulli flow (Regime II), (*iii*)

turbulent diffusion (Regime III), and (*iv*) combined turbulent diffusion and Bernoulli flow (Regime IV). Based on the typical dimensions of real staircase openings in dwellings, the predominant airflow regime in staircases openings should be regimen I or II. Regime I occurs when the partition height (H) is very small, thus the pressure is the same on both sides of the partition. However, a thin layer of the heavier fluid (brine) over a layer of lighter fluid (fresh water) exists, which causes disturbance and instability. This instability, called Taylor's instability, triggers the fluid movement and flow exchange between both sides of the opening. This flow exchange was visualized as upward plumes or fingers of fresh water entering the upper compartment, while downward fingers of brine were entering the lower compartment.
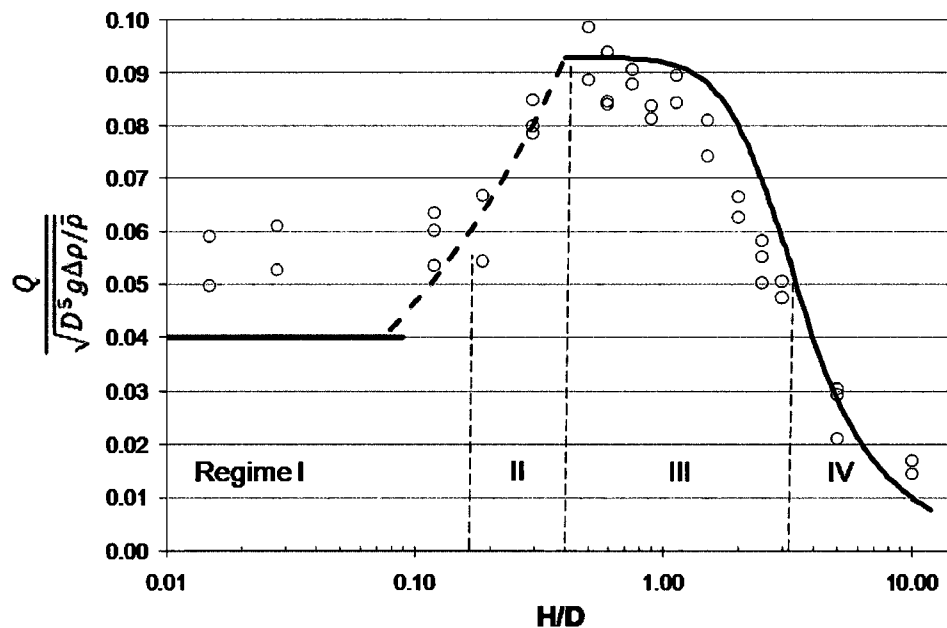
Figure 2.3: Experimental results for the volumetric airflow rate, Q, as function of the ratio H/D. Lines represent the relationship between the flow rate, Q, and the function $f(H/D)$ for different flow regimes (Epstein, 1988).

Regime II is inherently unstable and no steady flow distribution can be assumed. However, Brown (1962) derived a relationship between the pressure difference on both sides of the opening, geometry of the opening and fluid properties above and under the

opening. He considered that at any flow distribution, the lighter fluid flows upward and the heavier fluid flows downward. Then, considering the pressure at the bottom and top of the partition as uniform, the pressure difference driving the upward and downward flows can be calculated. This approach has been used by other researchers to obtain empirical equations for the airflow through horizontal openings in their own studies (Klobut and Sirén, 1994; Kohal, 1995; Woloszyn, 1999).

Similarly to Epstein's experiment, Blomqvist and Sandberg (2004) studied flow exchange through square horizontal openings in a scale model test. Water was used as the operating fluid, and density differences between the upper and lower compartments were generated using salt water (the heavier fluid) in the upper compartment. They measured the flow exchange through the free square opening of 80 mm x 80 mm and 10 mm thick, and the flow exchange through the same opening with a sloped plane under it to simulate a staircase. It was found that the flow through the free square opening is given by Eq. 2.2. It can be observed that the Eq. 2.2 is similar to Eq. 2.1 with a proportionality coefficient of 0.063 instead of $f(H/D)$ and with the opening area (A) instead of the opening diameter (D).

$$Q = 0.063 A \sqrt{A^{0.5} g \Delta \rho / \bar{\rho}} \tag{2.2}$$

where Q is the volumetric flow rate (m³/s), A is the opening area (m²), g is the acceleration due to gravity (m/s²), $\Delta \rho$ is the density difference between the two compartments (kg/m³), and $\bar{\rho}$ is the mean density of two compartments (kg/m³).

Blomqvist and Sandberg also measured the flow rates for cases with a sloped plane under the horizontal opening, which tried to simulate a stair. They found that the flow rate through the opening with the sloped plane increased only by 13% in comparison with the flow rate through the opening without the sloped plane.

2.2.2 Review of studies carried out in a half-scale model of stairwells

The study of buoyancy-driven flows in half-scale models of stairwells was carried out by a number of researchers, such as Zohrabian et al. (1989), Ergin-Özkan et al. (1995) and Mokhtarzadeh-Dehghan (2007). Zohrabian et al. (1989) studied the airflow in a half-scale model of a stairwell. Air movement was induced by a heater placed in the lower compartment of the stairwell. Figure 2.4 shows the airflow pattern found in the stairwell. Three different regions can be observed. The first region is located in the lower compartment, where warm air rises from the heater and propagates along the ceiling, and cold returning air enters the lower part of the heater. The second region is the upper compartment, where warm air enters this zone and forms two large eddies. The third region is the throat. Here, a two-way airflow exists, the upflow of warm air above the downflow of cold air. Zohrabian et al. (1989) also studied the velocity and temperature distribution along the throat region and the influence of different heating powers (e.g. 100 W, 300 W, 600 W and 900 W).
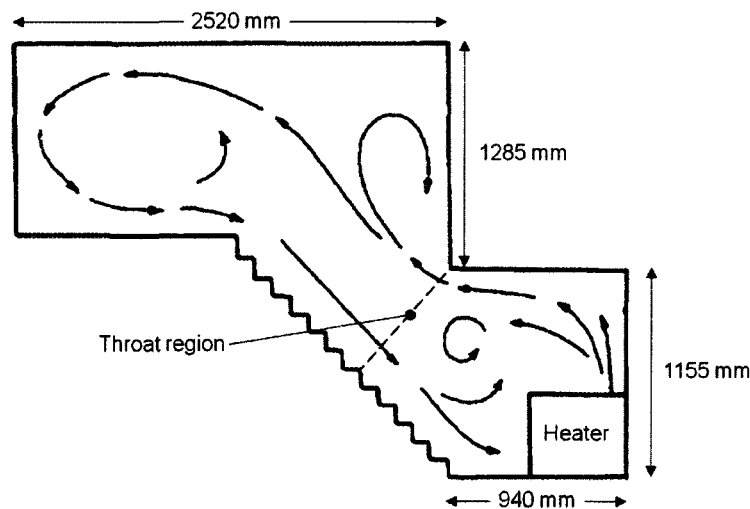
Figure 2.4: Airflow pattern in the half scale model of the stairwell of Zohrabian et al. (1989).

Ergin-Özkan et al. (1995) extended the work by Zohrabian et al. (1989) to include through-flow across the stairwell via two small openings, one as the air inlet in the lower

compartment and the other as the air outlet in the upper compartment. The power of the heater was set at 300 W and different outlet sizes were tested. The airflow pattern in the stairwell is shown in Figure 2.5. It can be seen that the airflow pattern is similar to that found in the closed staircase (Figure 2.4); the inlet mainly disturbs the airflow in the lower compartment. The recirculating airflow rate is between 0.011 and 0.04 m³/s for temperature differences between the lower and the upper compartments between 1.0°C and 5.5°C.
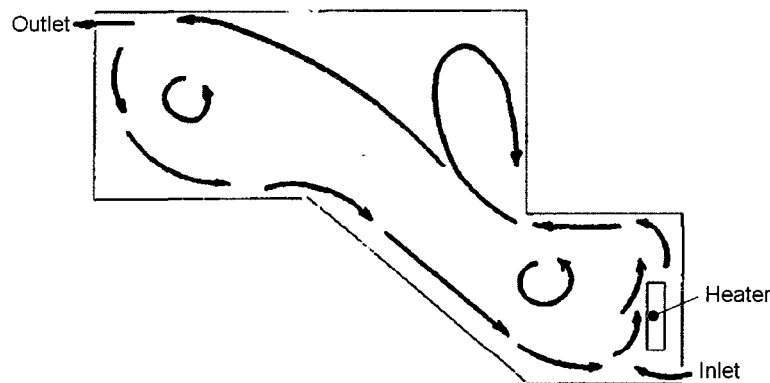
Figure 2.5: Airflow pattern in the half scale model of the stairwell of Ergin-Özkan et al. (1995).

The designed features of the half scale-model used by Zohrabian et al. (1989) and Ergin-Özkan et al. (1995) resulted in predominantly 2D airflow pattern. To study the airflow pattern under more realistic conditions, Mokhtarzadeh-Dehghan (2007) studied buoyancy-driven flows in a half-scale model of a stairwell constituted by a lower floor, the stairwell and an upper floor. The resulting airflow pattern was fully 3D, which is more representative of airflows occurring in buildings. The experimental setup is shown in Figure 2.6.

The heating power of the heater was set between 300 and 750 W. This study focused on the heat losses through the walls of the stairwell and heat transfer between the upper and lower compartments of the stairwell. Also, measurements of temperature and air speed were taken at the middle plane of the opening. These measurements are

shown in Figure 2.7. It was found that the interface between the upward and downward airflows occurs between X_1 equal to 0.9 and X_1 equal to 1.0 (X_1 can be seen in Figure 2.6b). The upward airflow shows higher velocities than the downward airflow. Because mass balance should be accomplished at the opening and due to the 3D airflow pattern, Mokhtarzadeh-Dehghan indicated that downward airflows should have existed in other zones of the opening.
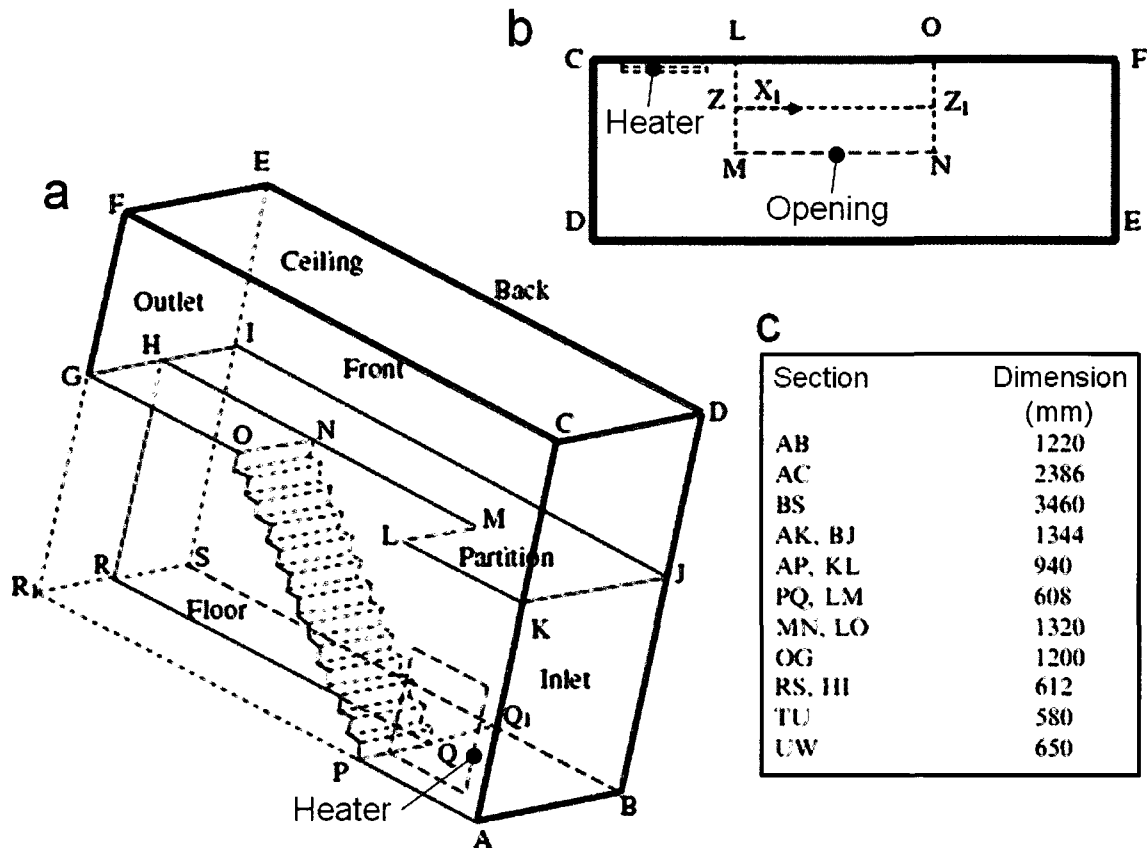
Figure 2.6: One half scale-model used by Mokhtarzadeh-Dehghan (2007): a) Isometric view, b) plan view, and c) dimensions.

2.2.3 Review of studies carried out in full-scale setups

A few full-scale experimental investigations have been carried out with buoyancy airflows in full-scale two-room setups where the lower and upper rooms were connected by a large horizontal opening (Riffat et al., 1994; Li, 2007), and in real stairwells in two-story and three-story buildings (Peppes et al., 2001, 2002).

25
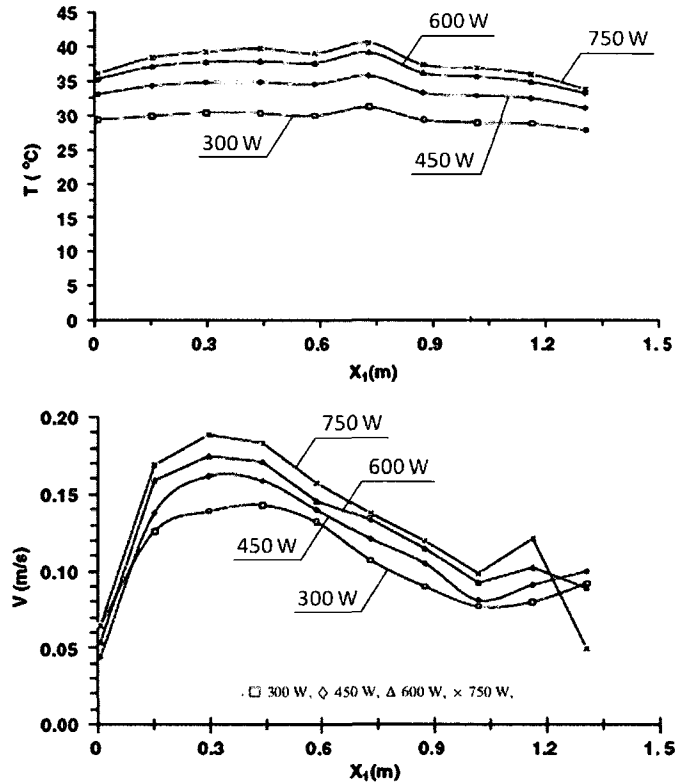
Figure 2.7: Measured temperatures and air velocities by Mokhtarzadeh-Dehghan (2007) in the middle plane of the opening.

The experiments of Riffat et al. (1994) were carried out in the two-room setup shown in Figure 2.8. The two rooms were connected by a large square horizontal opening of 1.69 m^2 and 0.3 m thick. The lower room was heated by means of thermostatically controlled heaters, while the upper room was unheated. Several experiments were carried out for temperature differences, between the average temperatures of the lower and the upper rooms or ΔT, ranging from 0.5°C to 4°C (the lower room was heated to temperatures between 18°C and 33°C).

The airflow rate between the two rooms was estimated from tracer gas (Sulfur Hexaflouride - SF$_6$) concentration data. Applying Bernoulli's equation and an empirical equation for the discharge coefficient as function of ΔT, Riffat et al. (1994) found that the mass flow rate (upward and downward mass flow rates were assumed equal) through the opening was given by:

$$F = 0.57\bar{\rho}Ae^{-0.23\Delta T}\sqrt{gH\Delta T/\bar{T}} \qquad (2.3)$$

where F is the mass flow rate (kg/s), $\bar{\rho}$ is the mean density of the upper and the lower rooms, A is the opening area (m^2), g is the acceleration due to gravity (m/s^2), H is the opening thickness (m), ΔT is the temperature difference between the lower and the upper rooms (°C), and $\bar{T}$ is the mean temperature of the lower and the upper rooms (°K).
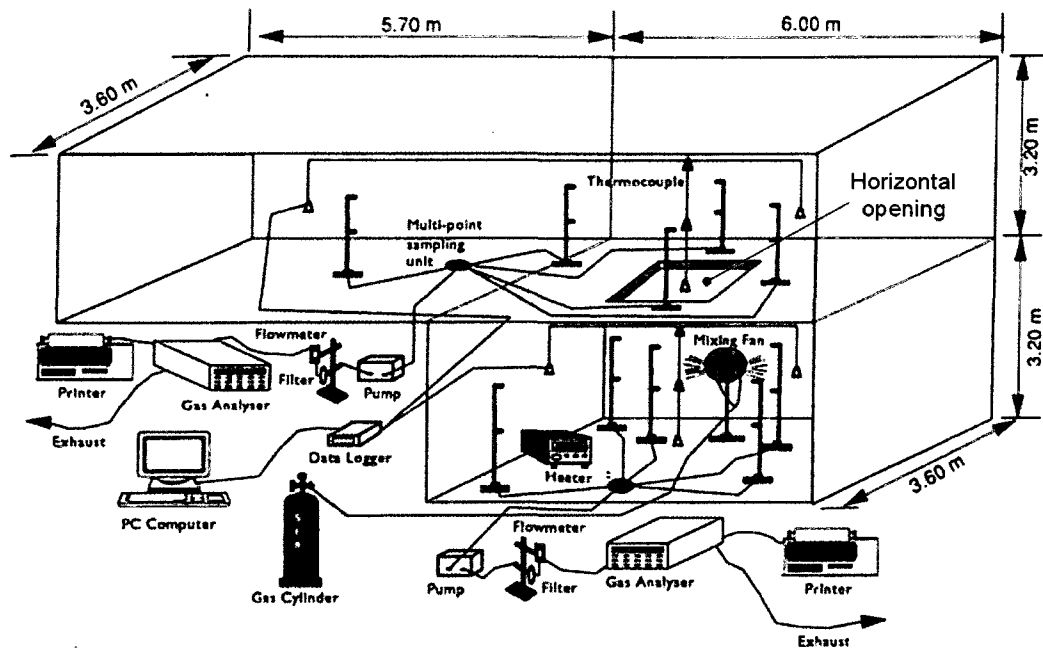
Figure 2.8: Full-scale two-room setup of Riffat et al. (1994).

Figure 2.9 shows the five mass flow rates obtained by Riffat et al. (1994) and the mass flow rate given by Eq. 2.3 for ΔT between 0°C and 4°C. Good agreement can be observed between the measured and estimated mass flow rates up to ΔT equal to 1.5°C. After this point, the mass flow rate decreases due to the negative exponential coefficient of Eq. 2.3. This reduction in mass flow rate does not have physical explanation and none reason is given in Riffat et al. (1994).

Additionally, it should be noted that Eq. 2.3 is similar to the flow relationships found by Epstein (1988) and Blomqvist and Sandberg (2004). While Eq. 2.3 is expressed in terms of mass flow rates and temperature differences, Eqs. 2.1 and 2.2 are expressed in

volumetric flow rates and density differences. Furthermore, Eq. 2.3 includes the area of the opening outside the square root, whereas the area of the opening is expressed in terms of the opening diameter inside the square root in Eq. 2.1.
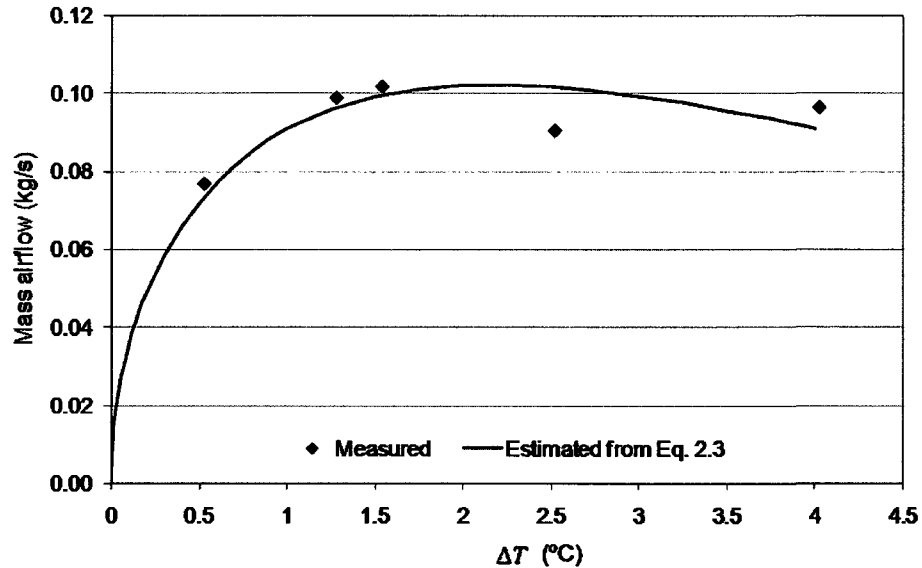
Figure 2.9: Measured and estimated mass flow rates through the horizontal opening based on results published by Riffat et al. (1994).

Li (2007) studied the influence of the ratio between the thickness and side of a square opening and ΔT on the buoyancy-driven flows through a horizontal opening. In his test setup, the horizontal opening connected a test room with a thermostatic chamber as shown in Figure 2.10. The opening side was varied between 0.2 m and 1 m, while the thickness of the opening was varied between 0.133 m and 1 m. The test room was heated, whereas the thermostatic chamber was unheated.

According to the experimental results presented by Li, ΔT was varied between 2°C and 30°C. Airflow measurements were carried out by means of the single tracer gas (CO_2) technique. Li compared his results with those obtained by Epstein (1988) for each flow regime. Main differences were found in the flow equation for Regime III, and no flow equation was found for regime IV. Also, Li found that highly transient and unstable two-way airflow existed through the horizontal openings.
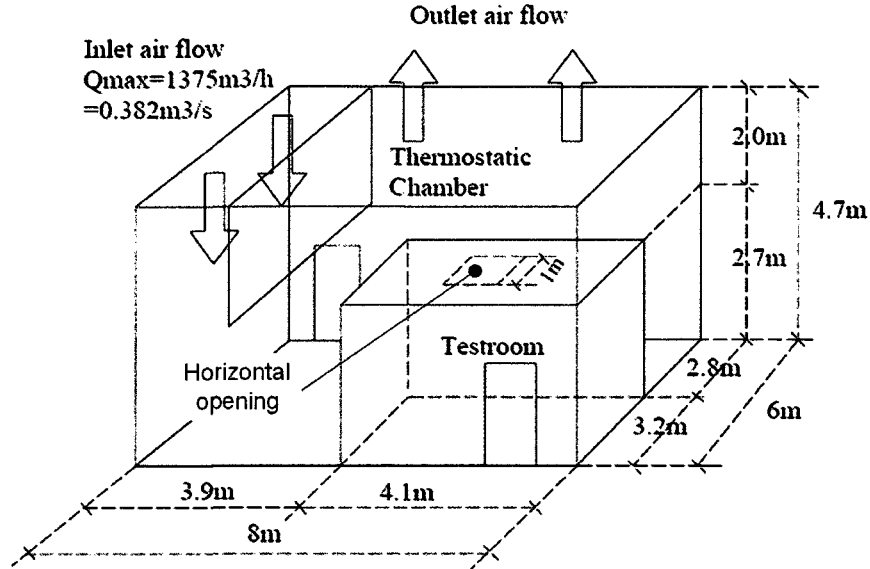
Figure 2.10: Test setup of Li (2007).

Peppes et al. (2001, 2002) studied buoyancy driven flows in real two-story and three-story stairwells as shown in Figure 2.11. Peppes et al. (2001) studied two different size openings, 2.5 m x 1.5 m and 2.15 m x 1.5 m, and ΔT ranging from 0.1°C to 6.2°C. Airflow across the opening was measured using tracer gas (N_2O) technique. Based on the experimental measurements of the airflow rate and ΔT, Peppes et al. (2001) found that the mass airflow rate may be expressed by:

$$F = 0.1469\bar{\rho}A\sqrt{gH}(\Delta T/\bar{T})^{0.3} \tag{2.4}$$

where F is the mass flow rate (kg/s), $\bar{\rho}$ is the mean density of the upper and the lower rooms (kg/m³), A is the opening area (m²), g is the acceleration due to gravity (m/s²), H is the opening thickness (m), ΔT is the temperature differences between the lower and the upper rooms (°C), and $\bar{T}$ is the mean temperature of the lower and the upper rooms (°K).

Eq. 2.4 is similar to the previous Eqs. 2.1 to 2.3. The main difference is that the mass flow rate is proportional to $(\Delta T/\bar{T})^{0.3}$ in Eq. 2.4 instead of $(\Delta T/\bar{T})^{0.5}$ as shown in Eqs. 2.1 to 2.3.

29
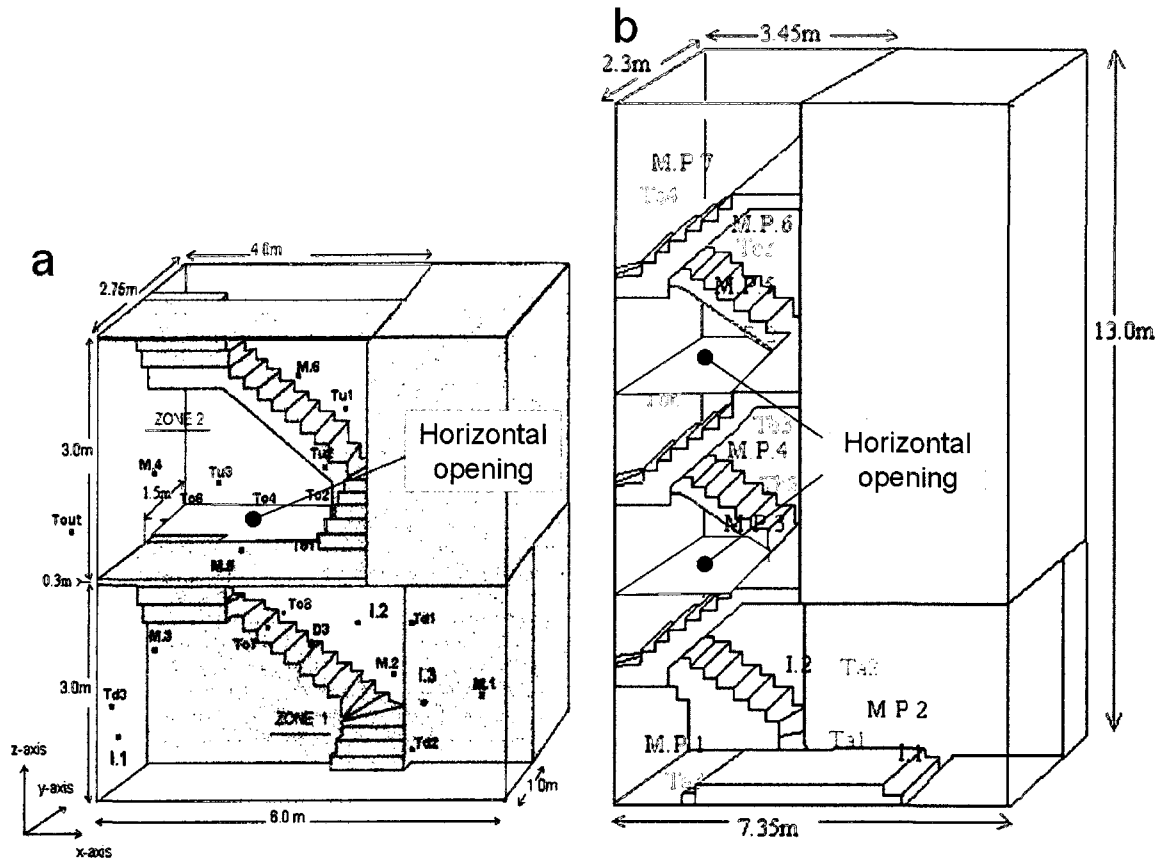
Figure 2.11: Stairwell of a) a two-story building by Peppes et al. (2001),and b) a three-story building by Peppes et al. (2002).

Also, Peppes et al. (2001) found that the mass flow rate increased with the opening size. Peppes et al. (2002) studied buoyancy-driven flows in a three-story stairwell (Figure 2.11b) consisting of a basement, first floor and second floor. The size of the opening was 2.3 m x 2.15 m. Five tests were carried out with ΔT ranging from 0.4°C to 4.5°C between the basement and the first floor, and ΔT ranging from 0.1°C to 1.2°C between the first floor and the second floor. Airflow rates through the openings were not estimated from tracer gas technique. Instead, Eq. 2.4 was used to calculate the mass flow rates across the openings.

2.2.4 Review of a study of combined buoyancy and forced flows

A unique experimental study carried out by Klobut and Sirén (1994) investigated the interzonal airflow through a horizontal opening with net flow through the opening. Figure 2.12 shows the small-scale two-compartment setup. The openings on the bottom and top of the two-compartment setup served as the supply air opening and exhaust air opening. A tracer gas (SF$_6$) was released in the compartment with the exhaust opening to estimate the airflow through the opening. Klobut and Sirén (1994) studied two opening sizes (0.455 m x 0.455 m and 0.64 m x 0.64 m), air change rate between 0.4 ACH and 2.3 ACH, downward and upward net flow through the opening, and ΔT between -3°C and 2°C. Negative values of ΔT indicate that this experiment also included cases with the upper compartment warmer than the lower compartment.
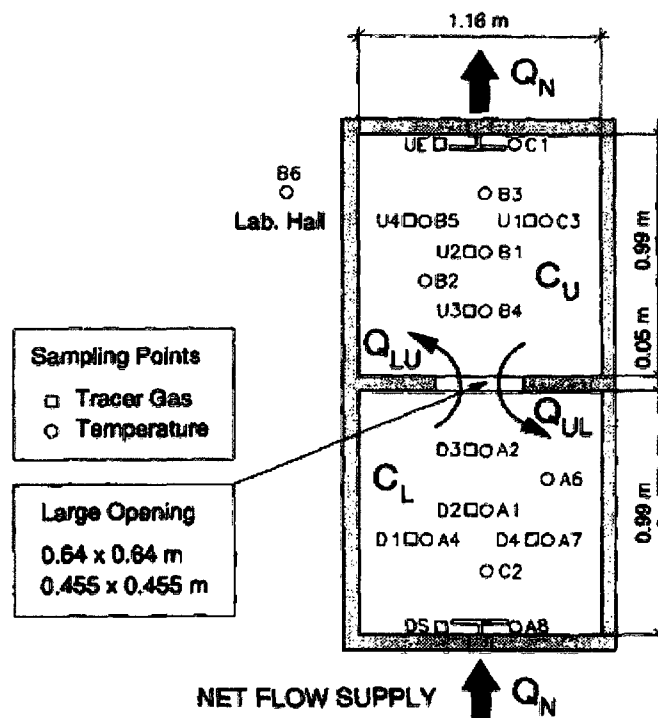
Figure 2.12: Two-compartment setup of Klobut and Sirén (1994).

Klobut and Sirén discussed their results in terms of "minor-flow", which was defined as the flow from the zone with the exhaust opening to the zone with the supply opening. It means that the minor flow is the airflow opposite to the net flow. Klobut and Sirén

31

(1994) found that all the parameters studied influenced the minor flow rate. For example, they found that the minor flow decreased with decrease in ΔT, thus minor flows were significantly smaller with warmer upper compartment than those with colder upper compartment. The existence of minor flows when the upper compartment was warmer could not be explained by Klobut and Sirén and they indicated that more studies were needed. Also, it should be noted that Klobut and Sirén's study did not derive any airflow equation representing the interzonal airflow through the opening.

2.3   Interzonal moisture transport through horizontal openings

Only two studies that included interzonal moisture transport between floors were found in the literature, Oldengarm and de Gids (1991) and Woloszyn (1999). However, both investigations were mainly focused on airborne moisture distribution and moisture storage capacity of indoor finishing and furnishing.

Oldengarm and de Gids (1991) carried out their test in a three-story field house. They used the tracer gas technique (SF_6) and short moisture generation (800 g over 30 min) to study the moisture transport from the kitchen to the rest of the house. Since SF_6 is an inert and non- absorbing gas, the comparison between the decay curves for SF_6 and water vapor allowed the study of the moisture absorption/desorption of wall surfaces and furniture as well as its impact on airborne moisture distribution and inter-zonal moisture transport.

Figure 2.13 shows the measured SF_6 concentration and the water vapor concentration difference (with respect to the outdoor air) in each room. Shown values correspond to the maximum values after the maximum peak concentration was reached in the kitchen. In this test 4% of the produced moisture was removed by exfiltration and 56% was stored by surfaces close to the moisture source during the moisture production. Therefore, only 40% of the moisture produced ended into the indoor air. This

moisture was spread mainly across the kitchen and adjacent living room, while only a small amount went up through the staircase, resulting in very low vapor concentration differences on the first and attic floors (0 to 0.7 g/kg). In contrast to the vapor concentration measurements, SF_6 measurements showed that it is transported mainly to the upper floors, where the gas concentration is 54% and 19% in the staircase and attic, respectively.
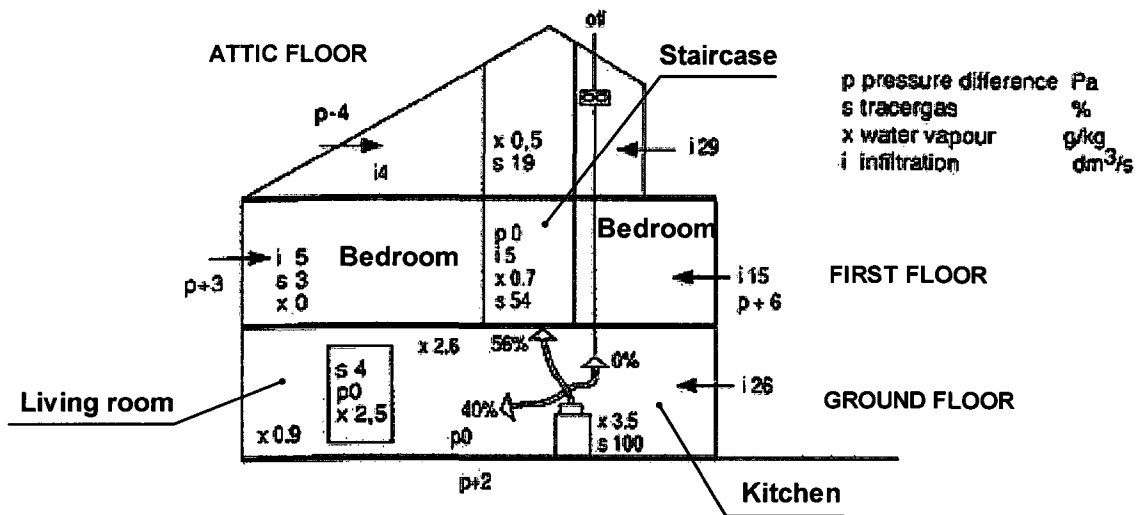
Figure 2.13: Three-story test house and measurements by
Oldengarm and de Gids (1991).

Comparing SF_6 and vapor concentration difference, Oldengarm and de Gids concluded that interzonal moisture transport is mainly restricted by the moisture absorption of indoor surfaces and furniture close to the source when short term moisture generation exists.

Like Oldengarm and de Gids (1991), Woloszyn (1999) used simultaneously the tracer gas (SF_6) and moisture release in the kitchen to study the interzonal airflow in a two-story dwelling and the influence of moisture absorption/desorption on interzonal moisture transport. The two-story test house shown in Figure 2.14 was instrumented with temperature and RH sensors located in the center of each room. A multi-sampler system was used to measure the SF_6 concentration in all six rooms. Temperature in all

rooms was set to be 22°C, doors were kept open and there was no mechanical ventilation.

Water vapor was produced in the kitchen at a rate of 1.7 kg over one hour. Simultaneously, SF_6 was injected in the same place. It was found that SF_6 concentration decayed significantly during the first 30-40 minutes while it was transported to the other rooms. The higher concentration of SF_6 occurred in the living room, about 27% (SF_6 concentration is given with respect to the maximum SF_6 concentration occurred in the kitchen). Additionally, the SF_6 concentration was lower than 5% on the floor above the kitchen during the first 20 min, and all the rooms on this floor reached the peak concentration between 15% and 18% after one hour.
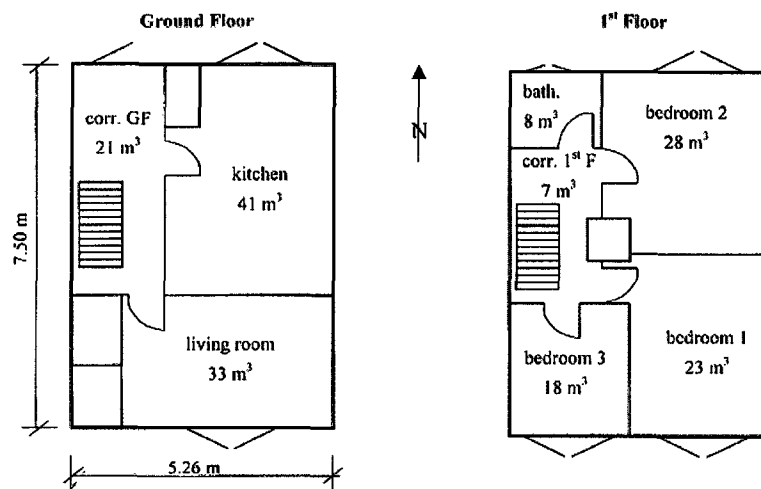
Figure 2.14: Floor plan view of the test house and zone arrangement (Woloszyn, 1999).

A different distribution was observed when vapor was released in the kitchen. Because of the high moisture generation, the moisture content in the kitchen increased about 12 g/kg, whereas in the rest of the rooms the moisture content increased only by 3 g/kg, approximately. The non-moisture source rooms showed similar vapor pressures. Woloszyn concluded that the moisture storage capacity of indoor surface materials and furniture in the kitchen restricted the moisture transport to the rest of the rooms. The small interzonal air and moisture transport in this study could have been caused by the

lack of temperature difference between connected rooms and due to the lack of mechanical ventilation. According to El Diasty et al. (1993), large temperature differences between zones and induced pressure differences due to wind are crucial for promoting interzonal moisture transport.

2.4 Discussion and closing remarks

From the literature review it can be seen that most of the investigations of airflow through horizontal openings dealt with buoyancy-driven flows, thus the driving force of interzonal mass airflow is the density difference ($\Delta\rho$) or temperature difference between the two zones (ΔT). A wide range of values of ΔT has been tested as shown in Table 2.1. This table shows that only five studies have derived empirical equations for the airflow through the opening as function of $\Delta T/\bar{T}$. Figure 2.15 compares the flow equations derived in these studies considering the following opening dimensions and tested conditions:

- Opening dimensions: the opening is rectangular with dimensions of 0.91 m x 1.19 m and 0.22 m thick. To establish the flow regime according to Epstein, the equivalent opening diameter, D, is considered to be equal to $\sqrt{4A/\pi}$, which yields a value of D equal to 1.17 m, and then, H/D is 0.19. This opening ratio corresponds to flow Regime II (see Figure 2.3) and $f(H/D)$ is equal to $0.147(H/D)^{0.5}$. Flow equation derived by Epstein and Li for flow Regime II are the same.

- Mean air density ($\bar{\rho}$) is considered to be 1.2 kg/m^3.

- Mean air temperature of the lower and upper rooms is 293.15°K (20°C).

Figure 2.15 shows that large variations exist among the relationship between mass flow rate through the horizontal opening and $\Delta T/\bar{T}$ found by previous studies for buoyancy-driven flow. For instance, at $\Delta T/\bar{T}$ of 0.008 (equivalent to ΔT of 2.3°C), the

35

interzonal mass airflow given by Peppes' flow equation is about 0.065 kg/s, while it is 0.032 kg/s in Epstein or Li's flow equation. This large variation may be the result of the different experimental setups and differences between scaled tests using water as fluid or full-scale tests using air as the fluid.

Table 2.1: Empirical flow equations and conditions tested in studies of buoyancy-driven flows through horizontal openings.

Study	Test scale/ fluid	ΔT (°C)	Mass flow equation
Epstein (1988)	Small/water &water brine	7 to 54[1]	$F = 0.187\bar{\rho}A\sqrt{gH\,\Delta T/\bar{T}}$
Riffat et al. (1994)	Full/air	0.5 to 4	$F = 0.57\bar{\rho}Ae^{-0.23\Delta T}\sqrt{gH\,\Delta T/\bar{T}}$
Peppes et al. (2001)	Full/air	0.1 to 6.2	$F = 0.1469\bar{\rho}A\sqrt{gH}(\Delta T/\bar{T})^{0.3}$
Blomqvist&Sandberg (2004)	Small/water &saline water	1 to 4[1]	$F = 0.063\bar{\rho}A\sqrt{A^{0.5}g\,\Delta T/\bar{T}}$
Li (2007)	Full/air	2 to 30	$F = 0.187\bar{\rho}A\sqrt{gH\,\Delta T/\bar{T}}$

[1] The temperature difference, ΔT, shown correspond to the equivalent values of the actual density differences ($\Delta\rho$) tested.
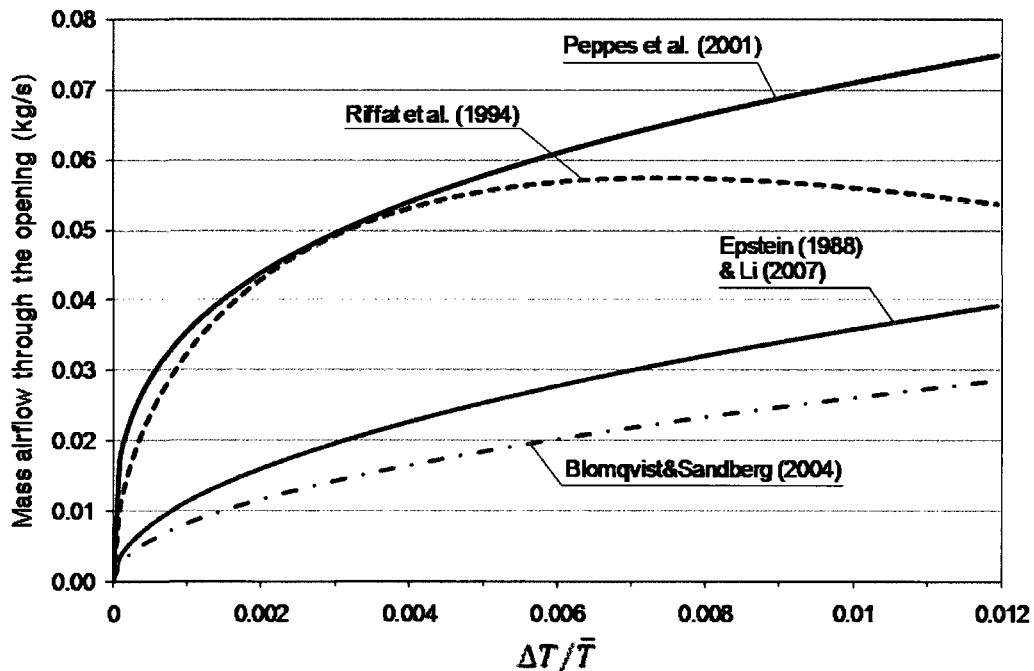
Figure 2.15: Empirical flow equations derived by previous studies of buoyancy-driven mass airflows through horizontal openings.

Also, Figure 2.15 shows that the curves from Peppes et al. (2001) and Riffat et al. (1994) are close up to $\Delta T/\bar{T}$ = 0.005. After this value, the mass flow rate given by Riffat starts to decrease, which shows a behavior different from those of other studies. This different pattern of Riffat's empirical correlation is due to the exponential term in Eq. 2.3. Furthermore, if the scale of the test is the main parameter influencing the derived flow equations, it is expected that the curve found by Li et al. (2007) would be close to the curves of the other full-scale tests (Peppes et al., 2001; Riffat et al., 1994), but it is the same curve found by Epstein who carried his studies in a small-scale two-compartment test setup. In conclusion, more studies are needed to obtain a general equation representing the airflow through horizontal opening even for cases with pure buoyancy flows only.

Besides buoyancy-driven flows through horizontal opening, mechanical ventilation and wind may cause net flow through the opening. Only the study of Klobut and Sirén (1994) was carried out considering net flow through a horizontal opening. Unfortunately, they did not obtain an airflow equation under this condition that includes the impact of ΔT and the ventilation rate.

Moreover, the previous literature review indicates the limited work done on the moisture transport through horizontal openings. The two investigations presented were carried out with a short term moisture generation and with small or no temperature difference between zones, which significantly reduce the interzonal airflow and then, the interzonal moisture transport.

The limited studies on full-scale on combined buoyancy and forced driven flows through horizontal openings and on interzonal moisture transport and moisture distribution prompted this thesis research. Understanding and quantifying the interzonal air transport through horizontal openings is essential not only to predict moisture levels in each zone of multi-story buildings, but also (i) to predict heat transfer and pollutant

transport and their distribution in each building zone, and (*ii*) to advance the science of total building response of HAM movement which was the Exercise 6 of Annex 41 of the International Energy Agency to which this writer participated.

CHAPTER 3

REVIEW OF CFD AND ITS APPLICATION TO RELATED STUDIES

3.1 Introduction

Computational fluid dynamics (CFD) is the most sophisticated airflow modeling method that can simultaneously provide temporal-spatial information of airflow, pressure, temperature, moisture and contaminant concentration. This information can be used to evaluate thermal comfort, indoor air quality, and energy efficiency of building systems, which are necessary and crucial aspects of the building design for architects, building and HVAC engineers, and researchers (Zhai, 2006).

Nielsen (1974) was the first one who applied CFD for airflow predictions in a room. After more than 30 years since this first application, CFD has gained popularity as an efficient and useful tool in the design and study of indoor environment (Chen and Zhai, 2004), which has been triggered by the rapid advances in computer capacity and speed. Furthermore, compared with experimental studies of indoor environment, CFD, once validated, is less expensive and results may be obtained much faster. This is the motivation of using CFD to complement the experimental study and extend the study to conditions that were not tested experimentally.

The governing equations of mass, momentum and energy that control the airflow, convective heat transfer and species transport are presented in section 3.2. The indoor zero-equation model developed by Chen and Xu (1998) is used in this research thesis to carry out the CFD simulations. This turbulence model was chosen among others because:

- It has been extensively validated and it provides good prediction of indoor airflow pattern and the distribution of temperature and species, especially for mixed convection cases. Section 3.3 reviews the main applications and validation studies

found in the literature.

- The computing time is much shorter than for other models, which allow performing a large number of simulations to extend the conditions tested experimentally in a reasonable period of time.

The aim of the application of CFD in this thesis is to predict the moisture distribution in the two-story test-hut and to compute the interzonal mass airflows through horizontal openings. In the literature, only a few studies have applied CFD to study interzonal airflows through horizontal openings, and none of them have studies the interzonal moisture exchange. On the other hand, some studies have used CFD to predict moisture distribution but only in single rooms. These studies are reviewed in sections 3.4 and 3.5.

3.2 Governing equations

Most of indoor airflows are turbulent and their nature is complex. Turbulent flow is 3D and random with many vortices or eddies. Turbulent eddies enhance mixing in the flow field, which increases diffusion of mass, momentum, temperature and species. Therefore, the indoor airflow can have effective heat transfer and distribution of species (Srebric, 2000). The airflow and related phenomena in the indoor environment are described by the governing equations of mass, momentum, energy and species concentration (so-called Navier-Stokes equations) that can be expressed in a common form as shown by Eq. 3.1. The generic variable ϕ represents the predicted air velocity, temperature or species concentration (Veersteg and Malalasekera, 1995).

$$\underbrace{\frac{\partial}{\partial t}(\rho\phi)}_{\substack{\text{Rate of} \\ \text{increase of} \\ \phi \text{ in the fluid} \\ \text{element}}} + \underbrace{\frac{\partial}{\partial x_i}(\rho V_i \phi)}_{\substack{\text{Net rate flow of} \\ \phi \text{ out of the} \\ \text{fluid element} \\ \text{(convection)}}} = \underbrace{\frac{\partial}{\partial x_i}\left(\Gamma_\phi \frac{\partial\phi}{\partial x_i}\right)}_{\substack{\text{Rate of} \\ \text{increase of } \phi \\ \text{due to} \\ \text{diffusion}}} + \underbrace{S_\phi}_{\substack{\text{Rate of} \\ \text{increase of} \\ \phi \text{ due to} \\ \text{sources}}}$$

(3.1)

40

where ϕ is 1 for mass continuity, ϕ is V_i (i = 1,2 and 3) for three components of momentum, ϕ is T for energy conservation, ϕ is C for species concentration (water vapor concentration or humidity ratio in this thesis research); t is time; ρ is air density; x_i is coordinate (i = 1,2 and 3); Γ_ϕ is the diffusion coefficient term; and S_ϕ is the source or sink term.

Eq. 3.1 can not be solved analytically except for special cases (Ferziger and Perić, 2002). Therefore, numerical computer simulations are needed to solve the Navier-Stokes partial differential equations. The solution of Navier-Stokes equations provides the field distribution of air temperature, velocity, relative humidity and contaminant concentrations. This is called the Computational Fluid Dynamics technique or CFD (Srebric et al., 1999). CFD predicts turbulent flows through three approaches: direct numerical simulation (DNS), large-eddy simulation (LES), and Reynolds-averaged Navier-Stokes (RANS) equations simulation with turbulence models. The CFD application in this research thesis involves only the RANS approach as shown below.

RANS uses approximations to simplify complex turbulent flows by means of solving time-averaged Navier-Stokes equations with turbulence models. The steady-state indoor airflow is described by the following Navier-Stokes equations for the conservation of mass, momentum, energy and species concentration (Chen and Xu, 1998):

- Mass continuity

$$\frac{\partial}{\partial x_i}(\rho V_i) = 0 \tag{3.2}$$

where ρ is the air density, V_i is the mean velocity component in the x_i-direction, and x_i is coordinate (for i = 1,2 and 3; x_i corresponds to three perpendicular axes).

- Momentum conservation

$$\frac{\partial}{\partial x_j}(\rho V_i V_j) = -\frac{\partial}{\partial x_i}(p) + \frac{\partial}{\partial x_j}\left[\mu_{eff}\left(\frac{\partial}{\partial x_j}(V_i) + \frac{\partial}{\partial x_i}(V_j)\right)\right] + \rho\beta(T_0 - T)g_i \qquad (3.3)$$

where ρ is the air density, V_j is the mean velocity component in the x_j-direction, p is the mean pressure, μ_{eff} is effective viscosity, β is the thermal expansion coefficient of air, T_0 is the temperature at the reference point, T is the mean temperature, and g_i is the acceleration due to gravity in the i-direction.

The last term in the right-hand side of Eq. 3.3 is the buoyancy term. In this study the Boussinesq approximation was implemented. This approximation treats density as constant in all solved equations, except in the buoyancy term of the momentum equation. This approximation introduces errors in the order of 1% if the air temperature differences are below 15°C (Ferziger and Perić, 2002).

The turbulent influences are lumped into the viscosity as the sum of the turbulent viscosity, μ_t, and the laminar viscosity, μ, as follows:

$$\mu_{eff} = \mu_t + \mu \qquad (3.4)$$

- Energy conservation

$$\frac{\partial}{\partial x_j}(\rho V_j T) = \frac{\partial}{\partial x_j}\left(\Gamma_{T,eff}\frac{\partial}{\partial x_j}(T)\right) + \frac{S_q}{c_p} \qquad (3.5)$$

where $\Gamma_{T,eff}$ is the effective diffusion for temperature, S_q is the thermal source, and c_p is the specific heat. Chen and Xu (1998) estimated the effective diffusion coefficient as:

$$\Gamma_{T,eff} = \frac{\mu_{eff}}{Pr_{eff}} = \frac{\mu}{Pr} + \frac{\mu_t}{Pr_t} \qquad (3.6)$$

where the laminar Prandtl number, Pr, is 0.71, and the turbulent Prandtl number, Pr_t, is 0.9.

- Species concentration conservation

$$\frac{\partial}{\partial x_j}(\rho V_j C) = \frac{\partial}{\partial x_j}\left(\Gamma_{C,eff}\frac{\partial}{\partial x_j}(C)\right) + S_c \tag{3.7}$$

where C is the species concentration, which, in this study, corresponds to the concentration of water vapor in the air or humidity ratio; $\Gamma_{C,eff}$ is the effective diffusion coefficient for C; and S_c is the species source term.

The effective diffusion coefficient for concentration is analogous to the effective diffusion coefficient for temperature as follows:

$$\Gamma_{C,eff} = \frac{\mu_{eff}}{Sc_{eff}} = \frac{\mu}{Sc} + \frac{\mu_t}{Sc_t} \tag{3.8}$$

where the effective Schmidt number, Sc, and the laminar Schmidt number, Sc_t, are equal to 1.0. Therefore, the first term on the right-hand side of Eq. 3.8 corresponds to the molecular diffusion given by:

$$\frac{\mu}{Sc} = \rho D_v \tag{3.9}$$

where D_v is the diffusion coefficient of the water vapor and it is equal to 2.5×10^{-5} m^2/s at 20°C.

The solution of Eqs. 3.2 to 3.8 provides the field distribution of velocities, temperature and water vapor concentration. To solve these transport equations, mathematical expressions for the turbulent viscosity (μ_t) are needed. The additional equation(s) needed to calculate the turbulent viscosity is(are) provided by the eddy viscosity turbulence models or so-called turbulence models. The most common turbulence models used in indoor environments are the k-ε models, such as the standard k-ε (Launder and Spalding, 1974), renormalization group (RNG) k-ε (Yakhot and Orzag, 1986) and realizable k-ε (Shih et al., 1995). All these turbulence models solve two additional equations for the turbulent kinetic energy, k, and the dissipation rate

of turbulence energy, ε. However, there are simpler models that solve only one additional equation. They are called one-equation eddy-viscosity models. Among these models, the indoor zero-equation model developed by Chen and Xu (1998) has been used in different indoor environment applications because of significant savings in computing time in comparison with the two-equation turbulence models. The indoor zero-equation model is explained in the following section as well as its applications for indoor environment.

3.3   Indoor zero-equation model and its applications

Standard k-ε and the RNG k-ε models are widely used for indoor airflow simulations because they have proven to provide successful predictions of the indoor airflow field, temperature and species concentration for different typical indoor scenarios. In searching for a simpler turbulence model that saves computing time in comparison with the k-ε models, Chen and Xu (1998) developed a new zero-equation model. This model considers the turbulent viscosity, μ_t, as a function of the local mean velocity, $\bar{V}$, and a length scale, l, as follows:

$$\mu_t = 0.03874\rho\bar{V}l \tag{3.10}$$

The constant 0.03874 is an empirical constant that applies to different flows. The length scale, l, is the distance to the nearest wall surface. Using Eq. 3.10 allows closing the set of conservation Eqs. 3.2-3.8.

While the k-ε model solves two additional transport equations for turbulence, the indoor zero-equation model does not need to solve any transport equation for turbulence and thus saves computing time. Although the indoor zero-equation model was developed to reduce computing time and to assist HVAC designers, it has proven to provide as good results as the standard k-ε model, or even better in some cases.

Chen and Xu (1998) applied the model to predict indoor airflows of natural convection, forced convection, mixed convection and displacement ventilation. They concluded that the indoor zero-equation model was able to predict indoor airflow patterns and distributions of temperature and contaminant concentration with reasonable accuracy. Srebric et al. (1999) applied successfully the model to more complex indoor airflow scenarios, such as natural convection with air infiltration, forced convection with a partition wall, mixed convection and displacement ventilation. The 3D room model included furniture and heat sources (e.g. lighting, baseboard heaters, computers and persons). Morrison (2000) implemented the indoor zero-equation model in ESP-r, an energy simulation program. He found that the model gave reasonable airflow predictions, but provided inaccurate surface heat convective coefficients for buoyancy-driven flows.

More recently, Zhang et al. (2007) evaluated several turbulence models, such as most of Reynolds-averaged Navier-Stokes (RANS) models and the LES model, to predict airflow and turbulence for four types of flows, natural convection, forced convection, mixed convection and strong buoyant flow in a fire room. The comparative evaluation shows that among the RANS models, the three-equation eddy viscosity model ($\overline{v^2} - f$ –dav or v2f-dav) developed by Davidson et al. (2003) and the RNG k-ε model showed the best overall performance. Although the overall performance of the indoor zero-equation model was found to be lower than that of the most advanced models, it was also found that the indoor zero-equation model performed better than the RNG k-ε for mixed convection, and provided results as good as the v2f-dav model for this type of flows. This is important because mixed convection flows are the types of flows studied in this thesis by means of CFD simulations.

Additional applications of indoor zero-equation turbulence model can be found in Chen et al. (2005) and Zhou (2007). Chen et al. (2005) applied this turbulence model to investigate the influence of the contaminant source location, occupant distribution and air distribution on emergency ventilation strategy. Zhou (2007) used the CFD results for different conditions in conjunction with a generic algorithm to optimize the ventilation system design and operation in office environments.

3.4   CFD applications to study interzonal mass airflows

Only a few studies exist concerning the CFD modeling of airflows in stairwells or through horizontal opening. Several of these studies involved experimental research previously outlined in *Chapter 2*. Zohrabian et al. (1988) and Mokhtarzadeh et al. (1995) investigated buoyancy driven flows in a scale-model of a stairwell, while Peppes et al. (2001, 2002) investigated the buoyancy-driven airflows in real stairwells in two-story and three-story buildings. A simplification of the stairwells in buildings is to consider only a horizontal opening. Riffat and Shao (1995) and Li (2007) investigated buoyancy driven flows through horizontal openings.

Zohrabian et al. (1988) investigated numerically the buoyancy-driven flows in a half-scale model of a stairwell. The performed CFD simulation was steady-state and 2D. The standard k-ε model was applied and a non-uniform mesh of 56x37 was used. The velocity vector field, air speed and temperature were predicted and compared with measurements carried out by Zohrabian et al. (1989). Figure 3.1 compares the measured (via smoke visualization) and predicted airflow pattern across the stairwell. Good agreement between both airflow patterns can be observed. The main features of the airflow field are the rising column of warm air above the heater (left side of low compartment), followed by nearly parallel flow in the lower compartment. One part of the warm air arising from the lower compartment moves toward the ceiling, whereas the

other part forms a recirculation zone. Cold air goes down along the steps to the lower compartment.
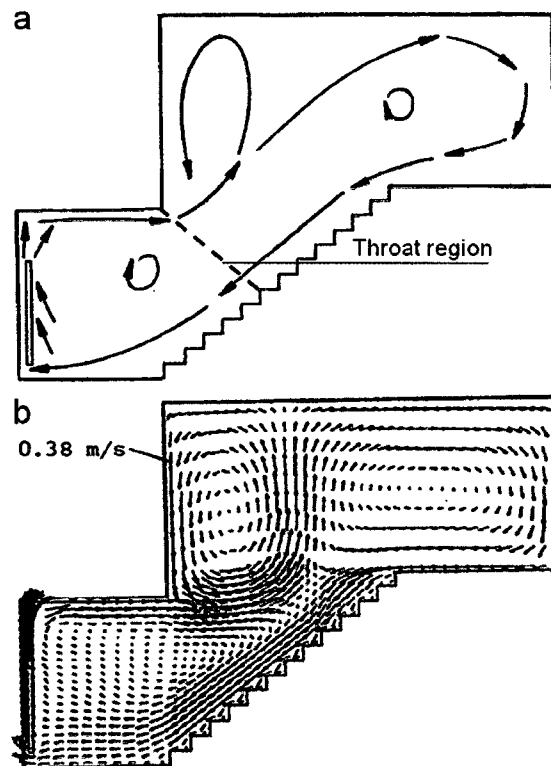
Figure 3.1: Airflow pattern in a half-scale model of a stairwell by Zohrabian et al. (1988): a) measured, and b) predicted.

The comparison between the measured and predicted air speed in the throat showed that the CFD underpredicts the air speed of the upflow and downflow. Also, the CFD overpredicts significantly the temperature by about 30°C in the throat region. Zohrabian et al. (1989) indicate that this difference in temperatures is because of significant heat losses through the sides of the stairwell that occurred during the experiment, which were not included in the 2D CFD model. They did not explain why the airflow pattern predicted by the CFD model agreed well with that measured even when extremely high temperatures were predicted by the CFD model. The work of Zohrabian et al. (1988) was extended by Mokhtarzadeh et al. (1995) by means of including an inlet in the lower compartment and outlet in the upper compartment of the stairwell.

Additionally, they performed 2D and 3D CFD simulations. Good agreement was obtained between the measured and predicted airflow pattern, air speed and temperature in the middle longitudinal plane of the stairwell.

Peppes et al. (2001) performed CFD simulations in the two-story stairwell shown in Figure 2.11a for 11 different temperature differences between the lower and the upper floors of the stairwell. They investigated the airflow rate through the horizontal opening as well as the temperature and gas concentration (N_2O) in the lower and upper floors of the stairwell. They used their own CFD algorithm and the well established CFD commercial software called PHOENICS to perform the 3D and transient CFD simulations. The RNG k-ε was applied and a coarse grid-mesh with 12,600 cells was used. The airflow rates through the horizontal opening were computed from the CFD results at each time step and averaged over the duration of the experiment, and compared with the measured airflow rates obtained with the tracer gas technique. The absolute relative difference between the computed and measured airflow rates was between 1.2% and 11.6% for all cases. Peppes et al. (2001) attributed these differences to the turbulence model, experimental errors and boundary conditions.

Additionally, the simulated and measured average temperatures in the lower and upper floors agreed closely with relative differences up to 0.6°C. Comparison between the simulated and measured average gas concentrations indicated that the CFD predictions overestimated the average N_2O concentration up to 17.5%. Part of this difference was attributed to the presence of air leakage during the measurements, while this phenomenon was not included in the CFD simulations.

Peppes et al. (2002) extended the previous study to the three-story stairwell shown in Figure 2.11b, thus the airflow was predicted via CFD simulation through the openings between the basement and the first floor and between the first floor and the second floor. The predicted CFD airflows through the openings were compared with those

48

theoretically calculated using Eq. 2.4. The absolute relative differences between the theoretical and predicted interzonal airflows were up to 10% in both openings. Figure 3.2 shows a contour plot of the vertical velocity component in both openings. Since there is no net flow through the openings, it can be observed that warmer air from the lower floors flows up through nearly half of each opening, while the colder air from the upper floors flows down to the other half of the opening. Unlike the studies of Riffat and Shao (1995) and Li (2007), this study found that the airflow pattern remained quite stable over time.

Additionally, Peppes et al. (2002) compared the relative differences between the measured and predicted average N_2O concentrations in each compartment. Differences between 3.6% and 6.9% were found in the basement, between 11.2% and 14.6% in the first floor, and between 11.5% and 15.3% in the second floor.
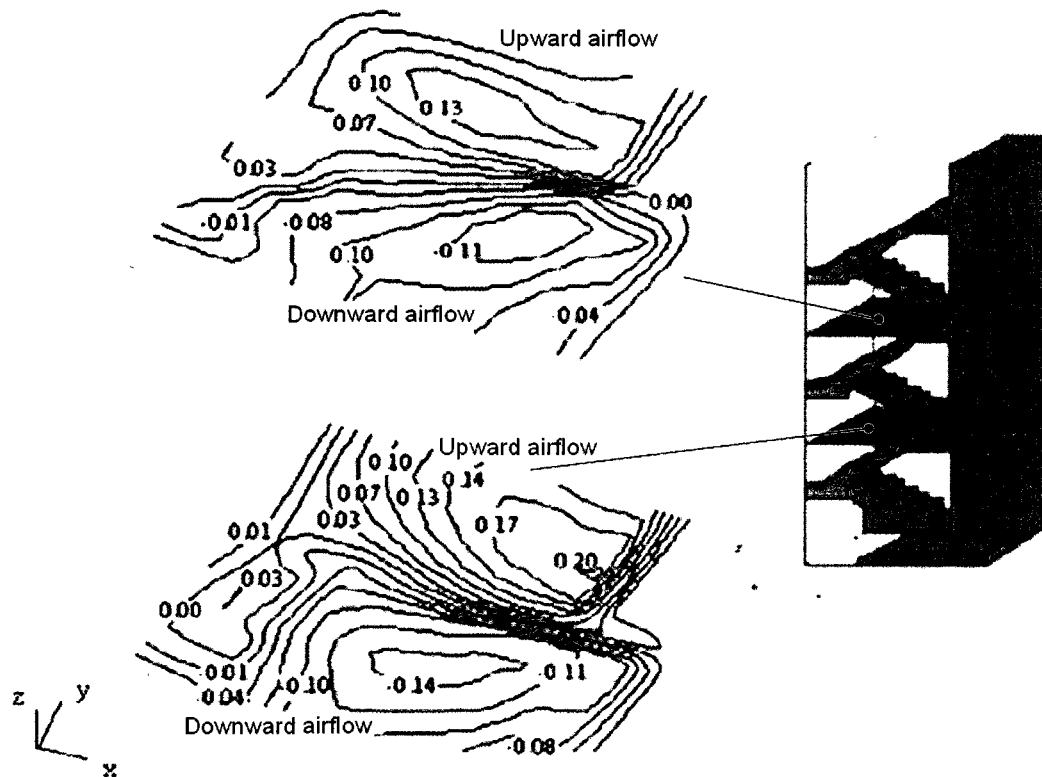
Figure 3.2: Contour plot of the vertical velocity component in the openings of the stairwell by Peppes et al. (2002)

Riffat and Shao (1995) carried out a simplified, 2D and transient CFD simulation of the experimental setup shown in Figure 2.8. The model of the building consisted of two rooms (3 m x 2 m each) connected by a horizontal opening of 1 m wide and 0.1 m thick. The initial air temperatures of lower and upper room were 27°C and 10°C, respectively. The temperature of the ceiling of the upper room was set to 10°C and the floor of the lower room was set to 27°C, whereas the temperature of the rest of the surfaces was set to 0°C.

The CFD simulation was performed over 20 minutes. Figure 3.3 shows the velocity vector field at different times. It can be observed that the airflow is chaotic and the flow field changes considerably across the opening over time. The occurrence of two-way airflow through the opening is clear. In the first frame (t = 210 s), the warmer air goes up through the right half of the opening, while the colder air goes into the lower room through the left half of the opening. The airflow pattern changes considerably for the other cases, for example at t = 1090 s, warmer air goes up through the center of the opening, while colder air goes down close to the edges of the opening.

Also, Riffat and Shao (1995) computed the instantaneous airflow through the horizontal opening over 1000 seconds as shown in Figure 3.4. It can be observed that the airflow rate is continuously oscillating, thus the dominant mode of air exchange between the two zones is intermittent pulses. Between two pulses the airflow through the opening is very small, such as the case shown in Figure 3.2 at t = 650 s, and mainly air exchange occurs at pulse movements, such as the frame at t = 210 s shown in Figure 3.2.

Comparison of the airflow through the horizontal opening between measurements and CFD results was carried out by Riffat et al. (1994). The computed airflow rate from the CFD results was obtained by averaging the instantaneous airflow rate over 20 minutes. The relative difference between the computed and measured airflows through

the horizontal opening was 10.5%, which is an excellent result considering that the CFD model was 2D.
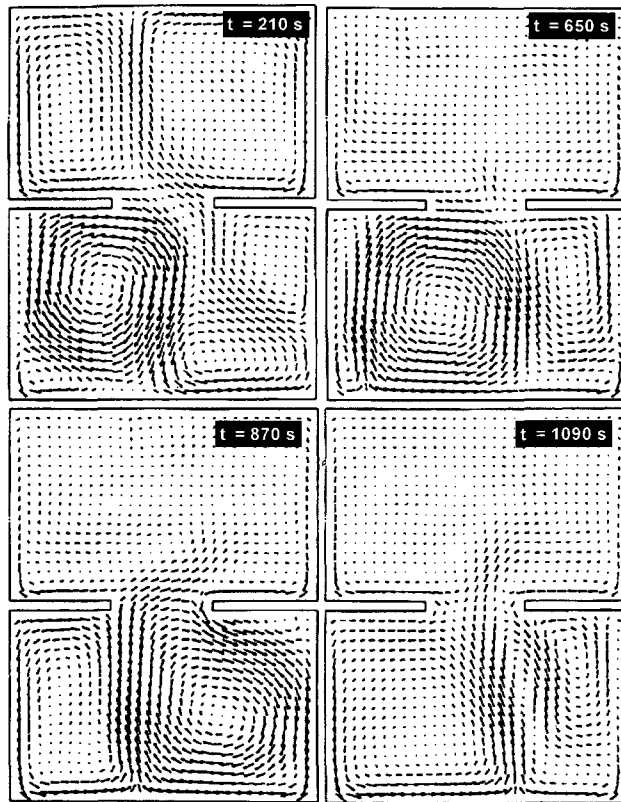
Figure 3.3: Flow pattern in two rooms connected by a horizontal opening at different times by Riffat and Shao (1995).
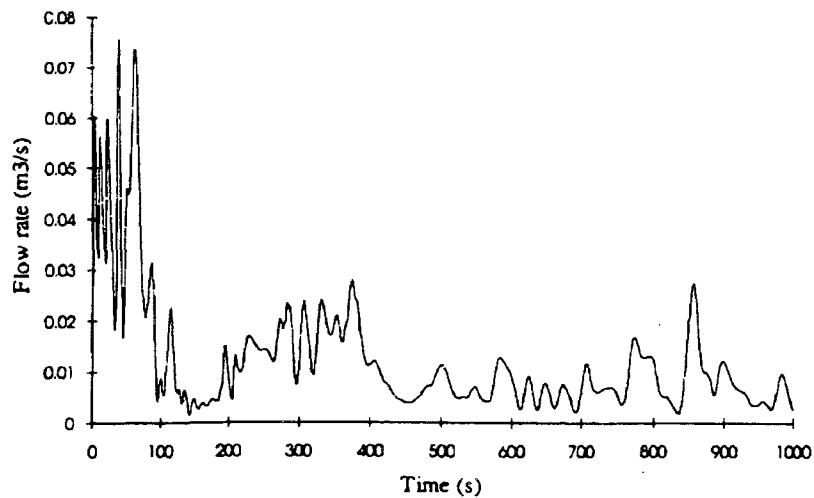
Figure 3.4: Transient airflow rate through the horizontal opening computed from CFD results by Riffat and Shao (1995).

Most recently, Li (2007) calculated the interzonal airflow through horizontal openings by means of 3D and transient CFD simulations using the CFD software called Fluent. He carried out the simulation using the standard k-ε model and LES when the temperature difference between the test room and the thermostatic chamber was 15.3°C. The CFD model of the experimental setup presented in Figure 2.10 is shown in Figure 3.5. It can be observed that the entire test room was modeled but only one part of the thermostatic chamber was included in the CFD model.
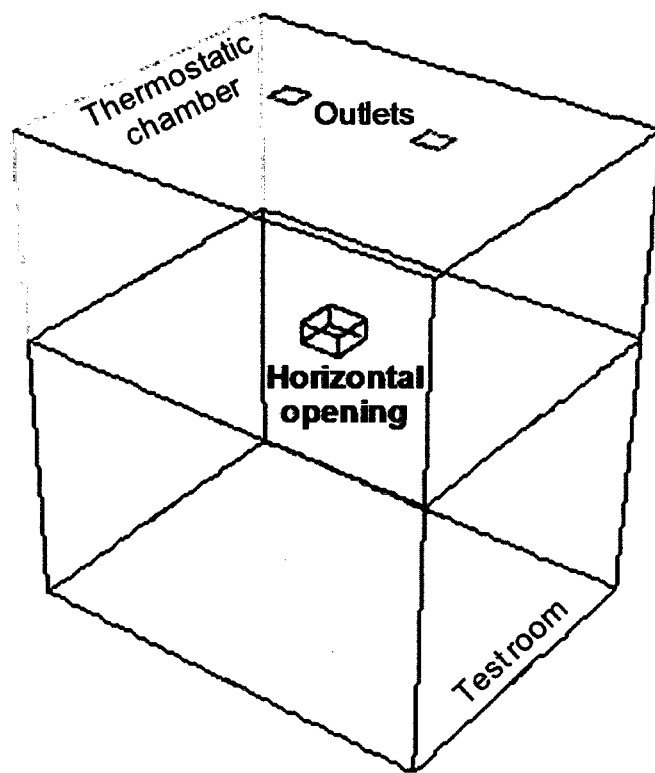
Figure 3.5: CFD model of the test-setup of Li (2007).

Like Riffat and Shao (1995), Li (2007) found that airflow through the opening was highly transient and unstable. Figure 3.6a and 3.6b show the transient airflow rates obtained from CFD simulations with the LES model and the standard k-ε model, respectively, and the measured average airflow rate using tracer gas technique. Since the measured average airflow rate seems to correspond well with the average airflow rate of CFD results for the LES model, Li concluded that the LES model was suitable to

predict detailed and accurate airflow rates through horizontal openings in cases of highly transient buoyancy-driven flows. In contrast the standard k-ε is inaccurate in predicting the airflow rates because the measured average airflow rate is much lower than the predicted transient airflow rates.
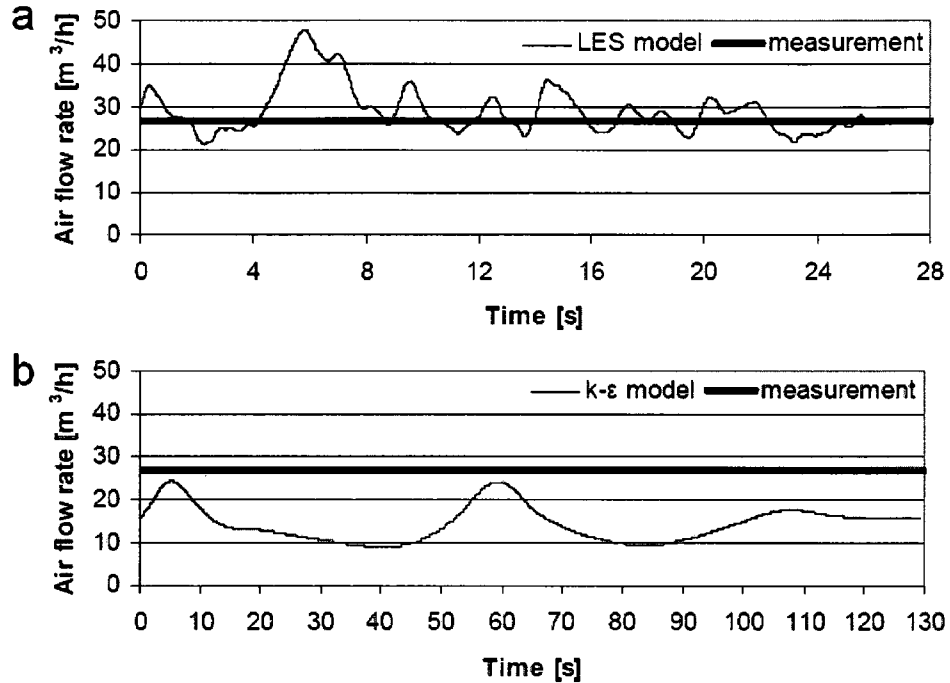
Figure 3.6: Comparison between the measured and computed airflow rates through the opening by Li (2007): a) LES model and b) the standard k-ε model.

3.5 CFD applications to study moisture distribution in single rooms

Several studies have used CFD to predict moisture distribution in single rooms. Most probably, the first study was carried out by Kolokotroni et al. (1992). In their test setup, a moisture source was placed in a small room that was connected to a large room via a small rectangular vertical opening. The transient moisture distribution in the large room was modeled using FloVent at the end of two different periods: (*i*) After a vapor production of 150 g over 30 minutes, and (*ii*) 90 minutes after the moisture production finished. No details about the turbulence model used are provided in Kolokotroni's study and it is only indicated that molecular diffusion was not included in the CFD model, thus

the moisture was transported only by the airflow. Results showed that significant humidity gradients occurred not only vertically but also horizontally in both periods. Differences of up to 3 g/kg and 2.2 g/kg were found at the end of the moisture production period and the decay period, respectively. Kolokotroni (1992) neither provides detailed information about the experimental setup nor about the validation of the CFD model.

Liu et al. (2002; 2004) used a Japanese CFD code, STREAM 4.0, to study the moisture distribution in a small room and to predict surface condensation on walls. In their tests the moisture source was placed inside the room and two ventilation strategies with 3.8 ACH were studied. Figure 3.7a shows the dimension of the small test-room, and locations of the vents and the moisture source. The CFD simulations were performed applying the standard k-ε model. The room was divided in 71500 cells approximately. Water vapor was modeled as a contaminant. To simplify the moisture and heat release from the water source, it was assumed that the moisture and heat flux were constant from the water surface towards the surrounding indoor air.
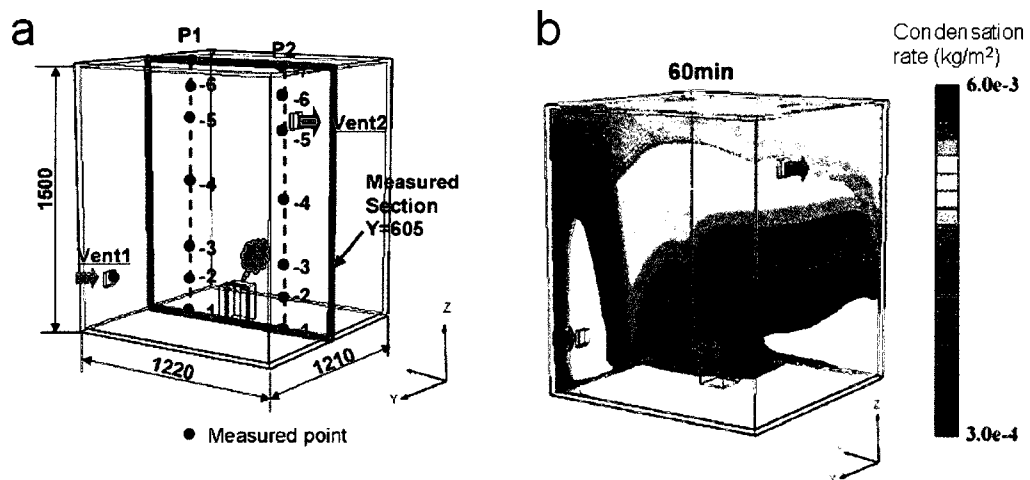
Figure 3.7: Test setup and results of Liu et al. (2004): a) Dimensions (in meters) of the small test-room, and b) condensation rate and location after 60 minutes.

Simulation results showed that differences in humidity distribution across the small room existed between the two ventilation strategies. Also, it was proved that the CFD

model was able to predict the locations where surface condensation occurs as well as the condensation rate (kg/m^2) as shown in Figure 3.7b. In addition, it was found that the buoyancy plume from the water source significantly influences the airflow pattern across the small test room. Although measurements were carried out, it should be noticed that no comparison with the simulation results was presented in these studies.

Hohota (2003) modeled the moisture distribution in a single room (3.1 m x 3.1 m x 2.5 m) using the realizable k-ε model in Fluent, and showed the capability of the CFD application in predicting condensation on wall surfaces. The humidity in the air supply was the only moisture source and different supply air conditions were simulated. The boundary conditions (average wall surface temperature and supply air conditions) were obtained experimentally. The air domain was divided into a large number of cells (about 1.3 million), and moisture was considered to be transported by convection and diffusion (water vapor diffusion coefficient of 2.55×10^{-5} m^2/s). Good agreement was obtained in comparing the numerical results for RH with measured RH in the test room. However, it should be noticed that RH within the test room was quite uniform because of the absence of indoor moisture source. For example, the RH ranged between 38% and 43.6% across the room for the case when warm air was supplied. Using Hohota's CFD model, Teodosiu et al. (2003) studied the influence of indoor air humidity on thermal comfort.

Since severe moisture problems can occur in microclimates, Mortensen et al. (2007) evaluated the capabilities of Hohota's CFD model to study the impact of different boundary conditions on microclimates, such as different location of furniture close to a cold exterior wall. In this case a microclimate was created by a thin air gap between a piece of furniture and the wall. A cubic room of 8 m^3 was modeled, and the space was subdivided in more than one million of cells. Unlike Hohota (2003), this study included a moisture source inside a room representing the moisture production 0.028 kg/h.

Additionally, the air supply and walls were moisture sources. Two different ventilation rates (0.5 and 1.5 ACH) were analyzed. Results showed that different placement of furniture near the colder external walls may affect the RH in the microclimate and that the highest RH values were found when the furniture was placed directly on the floor and had a small distance from the wall.

Most recently, Steeman et al. (2008) coupled a CFD model with the effective penetration model of Cunningham (1992) in Fluent to account for the moisture buffering effect on indoor humidity levels as well as the hygrothermal response of walls. Transient and 3D CFD simulation were performed considering the Hohota's test setup but including a uniformly distributed moisture source of 0.5 kg/h on the floor. A second-order two layer standard k-ε model was applied. A value of 2.55×10^{-5} m^2/s was assumed as diffusion coefficient of water vapor.

3.6 Discussion and closing remarks

The literature review shows that the CFD technique is suitable to study interzonal airflows through horizontal openings as well as the distribution of species (humidity ratio and gas concentrations). However, CFD has been applied only in cases with buoyancy-driven flows (natural convection), thus there are no studies considering combined buoyancy and forced flows (mixed convection), which represent conditions that are more realistic for dwellings. Also, studies of the moisture distribution in single rooms have been performed using CFD, and satisfactory results have been obtained. Therefore, the literature review shows that CFD may be a suitable technique to study interzonal air and moisture transport through horizontal openings in cases with combined buoyancy and forced driven flows.

One of the most important steps using CFD is the selection of the proper turbulence model for the physical phenomena to be studied. There are several

turbulence models, thus the selection should be based on balancing accuracy of the predicted results and computing time. In this thesis, the indoor zero-equation model was chosen. Despite the indoor zero-equation model is one of the simplest turbulence models, several studied have shown its applicability for indoor environments with mixed convection, which are the type of flows studies in this thesis by means of CFD simulations. Furthermore, the computing time of CFD simulations using the indoor zero-equation model is much shorter in comparison with more advanced turbulence model, which make it possible simulating many cases with different conditions. The validation of the CFD model is presented in *Chapter 6* for the specific conditions of this thesis research, while the CFD results are presented in *Chapter 7*.

CHAPTER 4

EXPERIMENTAL SETUP: FULL-SCALE TWO-STORY TEST-HUT

4.1 Introduction

This section describes the complex experiment setup to measure the air conditions across the two-story test-hut, to evaluate the moisture exchange between the two rooms, and to measure and analyze the mass airflows through the horizontal opening. In addition, the data obtained from this experiment provide input data for the CFD model and data to validate the CFD model.

Figure 4.1 shows a flow chart that illustrates how the experimental and CFD data are used. The main experiment measurements are:

- The distribution of temperatures (T), air speeds ($\bar{V}$) and humidity ratios across the two rooms and at the horizontal openings.

- Temporal humidity ratio (HR) profiles in each room over the moisture generation period, which are used to estimate the interzonal airflows through the horizontal opening.

- Steady-state average HRs in each room obtained from the temporal HR profiles in each room, which are used to analyze the interzonal moisture exchange.

- Boundary conditions, such as wall surface temperatures, supply airflow rate, moisture generation, heat generation, etc.

These experimental results are essential not only as input of the CFD model, but also as reference values to validate the CFD model. The boundary conditions measured experimentally are crucial for obtaining good CFD results because indoor airflow pattern and air conditions (temperature and humidity) are the results of boundary conditions. The validation of the CFD model is performed in two steps. In the step 1, the measured distribution of T, $\bar{V}$ and HR are compared with the corresponding computed values from

58

the CFD simulation. In addition, the temperatures and vertical component of the velocity at the opening obtained from the CFD simulations are used to predict the interzonal mass airflows, which are compared with those values measured. This comparison between the measured and predicted interzonal mass airflows corresponds to the Step 2 of the CFD model validation. Finally, the experimental data and the CFD data are used together to study the interzonal mass airflows and moisture exchange through the horizontal opening.

Figure 4.1: Flow chart of integrated experimental and CFD data.

4.2 Environmental Chamber

Tests were carried out in a full-scale two-story test-hut that was assembled inside the Environmental Chamber facility at Concordia University (Figure 4.2). This facility was built in the 1990s to investigate the hygrothermal performance of full-scale building envelope systems (Fazio et al., 1997). The Chamber consists of a cold box for simulating outdoor weather, a hot box for providing indoor conditions and two specimen frames to hold wall specimens between the two chambers. In the configuration of the

current investigation, the cold box, one specimen frame, and the hot box were joined without any wall specimen in between to form a single climatic chamber, with a large and continuous internal space of 7 m (H) × 4 m (W) × 6.6 m (L). The temperature condition in this large chamber can be controlled by two cooling systems and two electric heaters from -40 to 40°C. The fan (5.7 m³/s) that drives air through the evaporator also provides the air circulation for the large chamber. In addition, portable small fans are used to enhance air circulation in the chamber.
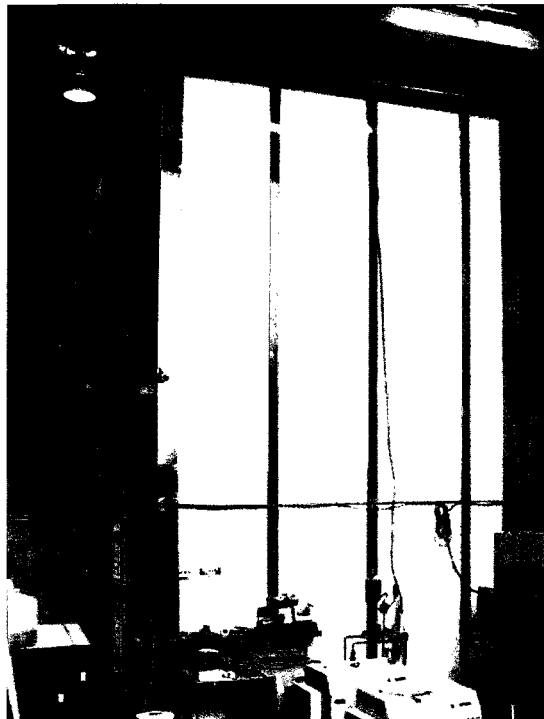
Figure 4.2: Environmental Chamber at Concordia University

4.3 Two-story test-hut

A two-story test-hut was pre-assembled in the Building Envelope Performance Laboratory (Figure 4.3) and then moved inside the Environmental Chamber (Figure 4.4). The test-hut consisted of two rooms with internal dimensions of 3.62 m x 2.44 m x 2.43 m each as shown in Figure 4.5a, which were connected by a horizontal opening with dimensions of 1.19 m x 0.91 m x 0.22 m (Figure 4.5b). The opening simulated a staircase opening through which heat, air and moisture are exchanged between the two

rooms. Larger staircase openings are found in dwellings; however, the ratio between the opening area and the floor area used in this experiment is similar to those found in real dwellings.
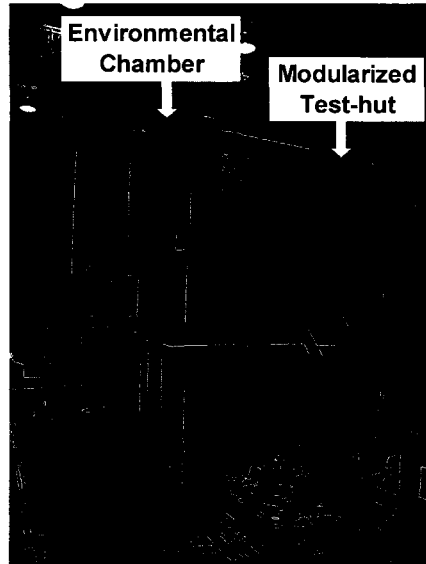
Figure 4.3: Pre-assembled under construction two-story test-hut.
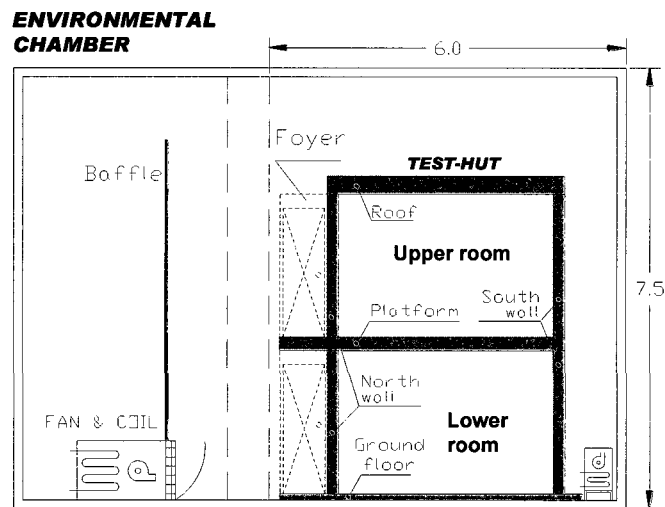
Figure 4.4: Location of the two-story test-hut inside the environmental chamber (dimensions are in meters).

The test-hut represents typical wood-framed construction of Canadian houses. The main features of the walls, ceilings and floors are shown in Table 4.1. The test-hut components are named in Figure 4.5a. A small foyer was built adjacent to the north wall

to house part of the Data Acquisition System and to reduce disturbance to the test rooms when doors were opened to set new conditions inside the rooms.
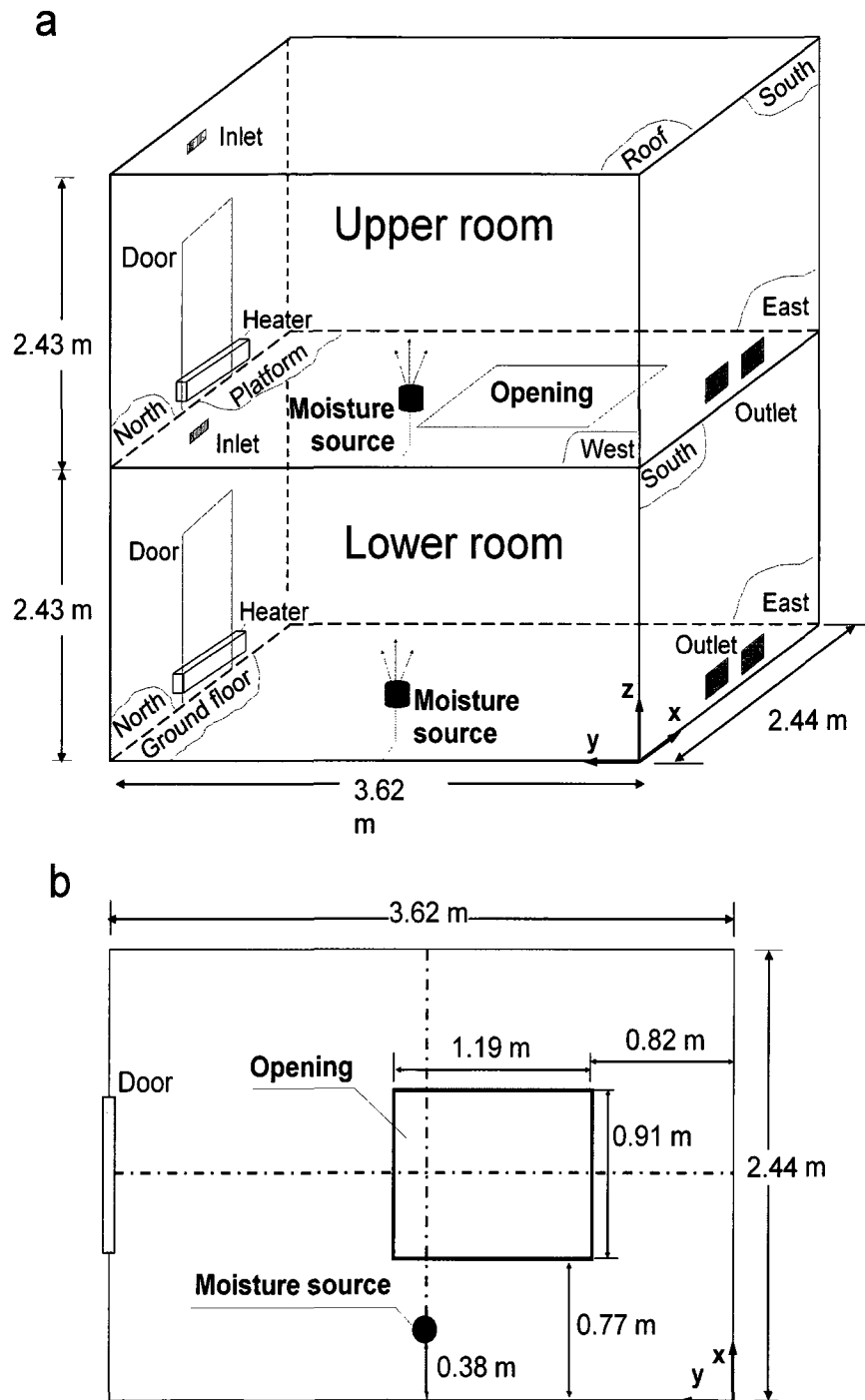
Figure 4.5: Two-story test hut: (a) isometric view and (b) plan view of opening with the moisture source location.

Table 4.1: Components of the test-hut.

Enclosure	Drawing	Details

East wall
West wall
		From outdoor to indoor:
		Vinyl siding
		Air cavity (19 mm)
		Air barrier (See Table 4.3)
		Sheathing:
		    Plywood: thickness, e = 12.5 mm
		Stud cavity:
		    Wood studs: 2x6 in @ 24 in
		    Glass fibre batt insulation (RSI = 3.34): e = 140 mm
		Vapor barrier:
		    Polyethylene sheets: 0.15 mm or 6 mil
		Finishing material:
		    Uncoated gypsum board (e = 12.5 mm) covered with polyethylene sheets

North wall
South wall
		From outdoor to indoor:
		Vinyl siding
		Air cavity (19 mm)
		Air barrier
		Sheathing:
		    Plywood: e = 12.5 mm
		Stud cavity:
		    Wood studs: 2x6 in @ 24 in
		    Glass fibre batt insulation (RSI = 3.34): e = 140 mm
		Vapor barrier:
		    Polyethylene sheets: 0.15 mm or 6 mil
		Plywood: e = 12.5 mm
		Aluminum sheet: e = 0.8 mm
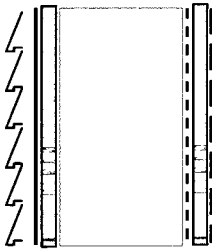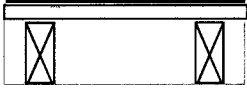
Ground floor		From indoor to chamber ground:
		Aluminum sheet: e = 0.8 mm
		Plywood: e = 15.9 mm (5/8 in)
		Insulation cavity:
		    Wood joists: 2x4 in @ 16 in
		    Glass fibre batt insulation (RSI = 2.1): e = 89 mm

Platform (floor between 1st and 2nd floors)		From the second floor to the first floor:
		Aluminum sheet: e = 0.8 mm
		Plywood: e = 15.9 mm (5/8 in)
		Insulation cavity:
		    Wood joists: 2x8 in @ 16 in
		    Glass fibre batt insulation: 2 layers of RSI = 2.1 each: e = 178 mm
		Polyethylene sheets: 0.15 mm or 6 mil
		Plywood: e = 15.9 mm (5/8 in)
		Aluminum sheet: e = 0.8 mm
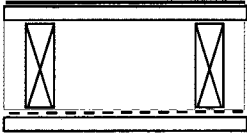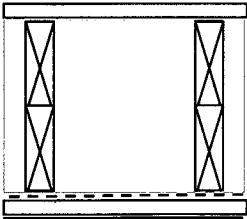
Roof		From outdoor to indoor:
		Plywood: e = 15.9 mm (5/8 in)
		Insulation cavity:
		    Wood joists: 2x6 in @ 24 in
		    Glass fibre batt insulation: 2 layers of RSI = 3.34 each: e = 280 mm
		Polyethylene sheets: 0.15 mm or 6 mil
		Plywood: e = 15.9 mm (5/8 in)
		Aluminum sheet: e = 0.8 mm

Table 4.1: Components of the test-hut (continued).

Enclosure	Drawing	Details
Doors		24-gauge galvanized steel facings Wood edges U-value: 1.08 W/m2·K Air gap between the door frame and wall was filled with sprayed polyurethane foam.
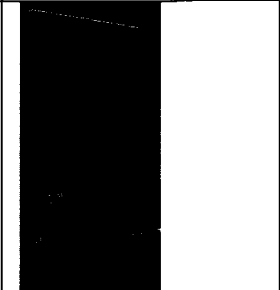
Interior surfaces of the east and west walls were made of unpainted gypsum board covered with polyethylene sheets (0.15 mm thick); very small vapor diffusion flows were estimated through these walls. The rest of the interior surfaces of both rooms were impervious to vapor (plywood covered with 0.08 mm thick aluminum sheets).

Additionally, emissivity of the interior finishing surfaces of the test-hut was measured using an Emissometer with Scaling Digital Voltmeter Model AE1 (Devices&Sevices Co.). The emissivity values obtained were:

- Uncoated gypsum board covered with polyethylene sheets: 0.65
- Aluminum sheets: 0.06

The air leakage was minimized by sealing all the indoor joints, door joints and holes for passing cables and wires (Figure 4.6). Wall cavities with large holes were sealed with polyurethane foam, silicone and aluminum tape, while the wall joints were sealed with latex sealant. Air leakage of the test-hut was measured at operating conditions, varying from 0.018 ACH to 0.027 ACH according to the procedure described in the Appendix D of Fazio et al. (2008).

4.4 Heating and ventilating system

4.4.1 Baseboard heaters

To provide the desired indoor temperature, an electric baseboard heater with a maximum power output of 1000 W was located at the base of the door in each room and

was controlled by an electronic thermostat (with a time proportional control for 0-100% capacity with a duty cycle of approximately 30 seconds). Figure 4.7 shows a picture of the heater and a schematic drawing of the heater dimensions and its location on the door.
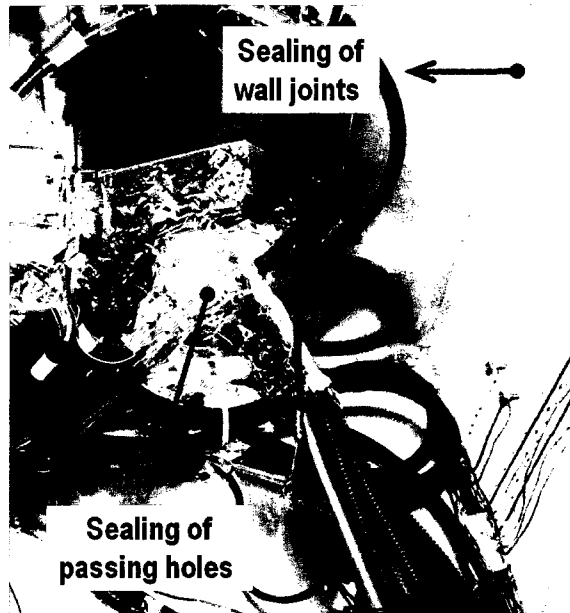
Figure 4.6: Sealing of passing holes and wall joints.
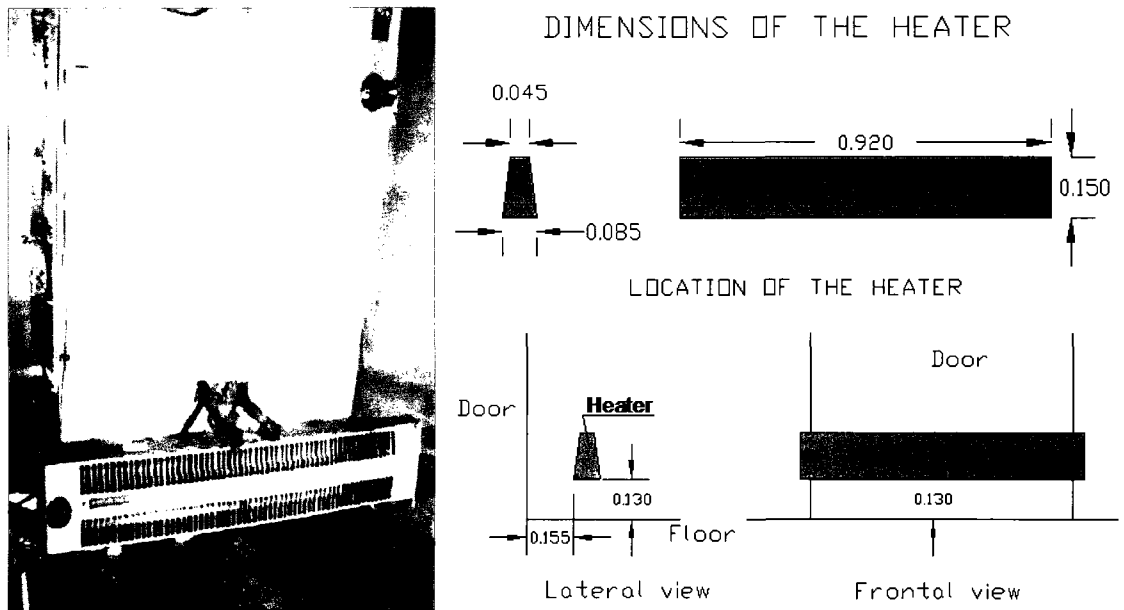
Figure 4.7: Baseboard heater (all dimensions are in meters).

4.4.2 Air Handling Unit

The ventilation system as well as the moisture generation system was designed by another Ph.D. student participating in the project, Xiangjin Yang, who carried out her thesis research on the same facility. These two systems are essential in this investigation and the description presented here is based on Fazio et al. (2008a). The ventilation system consisted of a closed system in which air was taken directly from the test-room (1 in Figure 4.8), treated by the Air Handling Unit (AHU), and then sent back to the test room (2). Each room had an independent ventilation system.
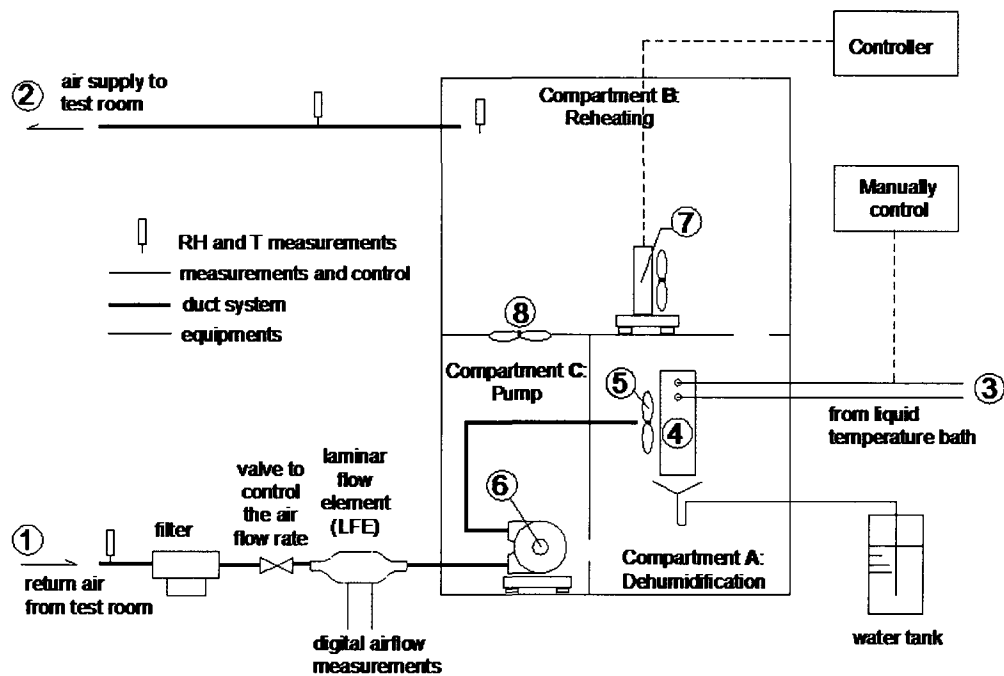
Figure 4.8: Components of the Air Handling Unit (Yang et al., 2007).

The AHU was specially designed to supply air at constant humidity and temperature. In the dehumidification compartment (A) of the AHU, cold water at a constant temperature from a liquid recirculation chiller (3) (NESLAB HX300w from Thermo Scientific, Inc.) was circulated in a water-to-air heat exchanger (4), which cooled the air. To remove the excess vapor in the return air so as to achieve a constant humidity ratio for the supply air for different test cases, the fan (5) within the heat

66

exchanger circulated the air through the coil many times inside the dehumidification compartment (A) before the air was pushed further into the upper compartment for reheating (B).

The air pump (6) (R3105, regenerative blower, Gast Manufacturing Inc.) was installed inside the AHU (Compartment C) to ensure that the minor shaft leakage of the pump did not compromise the air tightness of the air handling system. The electric heater (7) (1 kW with a time proportional control at 2 second duty cycle) in the compartment B was used to maintain the supply air within ±0.1°C of the designed temperature by a PID processing controller (Model 535 by Powers Process Controls). The small axial fan (8) in the middle divider circulated a small amount of the cold air into the pump compartment (C) to cool down the pump motor. The air flow rate through the entire unit was adjusted manually by a gate valve. The outside dimension of each AHU was about 2 m (H) x 1.5m (W) x 0.8m (D).

4.4.3 Inlets and outlets

Each room had one inlet and two outlets. The inlet face had a rectangular section with dimensions of 96.5 mm (W) and 21.8 mm (H). The inlet was installed in the middle plane of the north wall at 2.26 m height (distance between the floor and the center of the inlet). To verify that the air speed in the inlet face was homogenous, the air speed was measured at 7 points of the inlet face using an omnidirectional anemometer. The anemometer was placed about 5 mm from the inlet face. The results measured when the airflow rate was at 21.46 m^3/h and in the isolated single room are shown in Figure 4.9.

It can be observed that the air speed across the inlet face does not vary significantly and is close to the theoretical air speed of 2.83 m/s (flow rate/divided by cross section of the inlet face). Also, it can be observed that the turbulence intensity (TI) in the inlet is lower than 4%. Despite the uniform air speed across the inlet face, the

section change from circular to rectangular in a short distance (Figure 4.10) may have caused that the inflow spread in all direction. This was not confirmed via measurements and it should be taken into account during the CFD modeling of the inlets.

Point	V_{mean}	V_{rms}	TI (%)
1	2.89	0.092	3.2
2	2.89	0.102	3.5
3	2.82	0.042	1.5
4	2.79	0.041	1.5
5	2.70	0.063	2.3
6	2.82	0.037	1.3
7	2.71	0.024	0.9
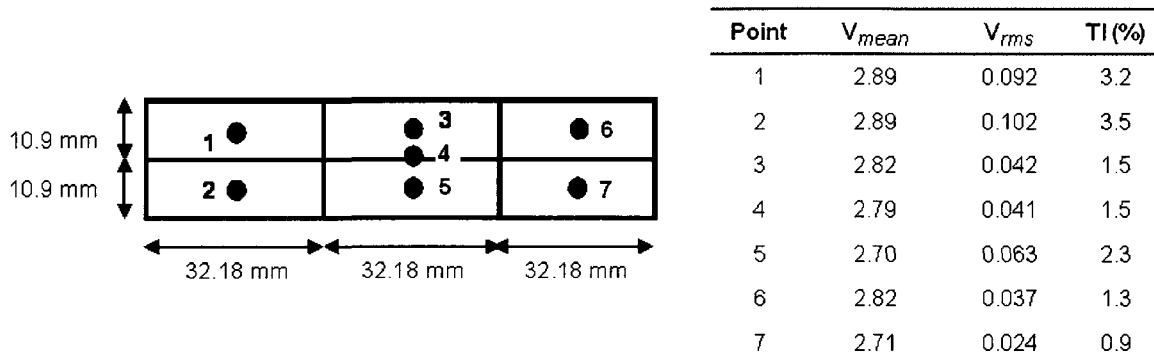
Figure 4.9: Characteristic air speed and turbulent air speed at the inlet.
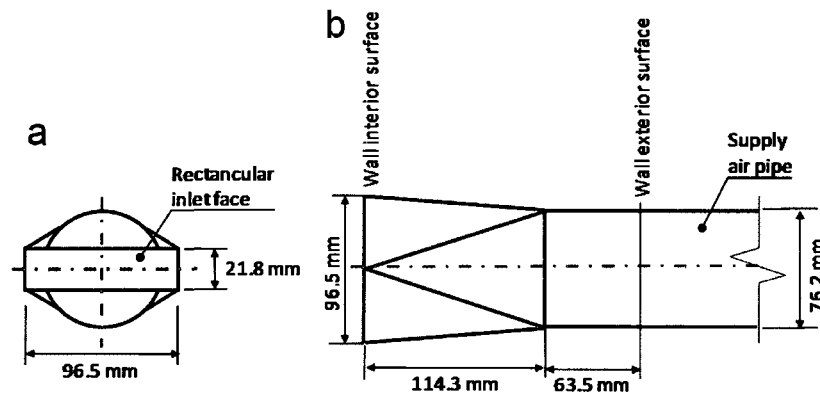
Figure 4.10: Drawings of the inlet adaptor: a) frontal view and b) longitudinal top view (adapted from Fazio et al., 2008b).

Two rectangular outlets, placed in the south wall, were connected outside the wall to one flexible pipe that returned the air from the test-hut to the AHU. Outlets had dimensions of 135 mm (W) and 85 mm (H). Figure 4.11 shows a schematic drawing of the location of these outlets in the south wall. To avoid condensation in the return pipe, a 25 W light bulb was installed inside each outlet to increase the temperature of the exhaust air. Black fine screens were installed at the outlets to minimize the radiation influence to indoors from the light bulbs.
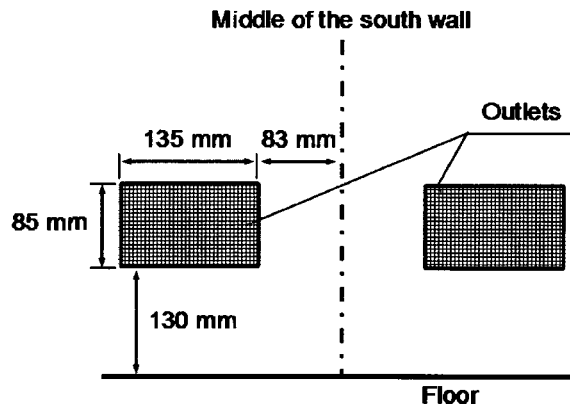
Figure 4.11: Location and dimensions of the outlets.

4.5 Moisture generation system

Moisture was generated either on the first floor or the second floor at a constant rate. Because part of this thesis research analyzes steady-state conditions for humidity ratio at the end of the moisture generation period, a moisture generation period of 10 hours (followed by 14 hours without moisture generation) was set for most of cases to reach steady-state conditions. In cases without ventilation, water vapor was produced only over 3 h to avoid surface condensation and damage of RH sensors. To generate the moisture, water was pumped by a multichannel cartridge pump (model Watson-Marlow Sci-Q205, Thermo Scientific) from a tank outside the room (in the foyer room) to a stainless steel recipient on a small heater (Micro Hotplate, model 120, Thermo Scientific). Thus, when water dripped into the pot, it evaporated immediately. A load cell beneath the water tank monitored the weight change of the water tank (Figure 4.12). The location of the evaporation system is shown in Figure 4.5. A small chrome wire shelf with an aluminum sheet (0.38 m x 0.71 m) on top was used to support the hotplate and the steel pot. The bottom of the steel recipient was placed at 0.55 m height.

Water tank   **Water pump**   **Evaporation system**
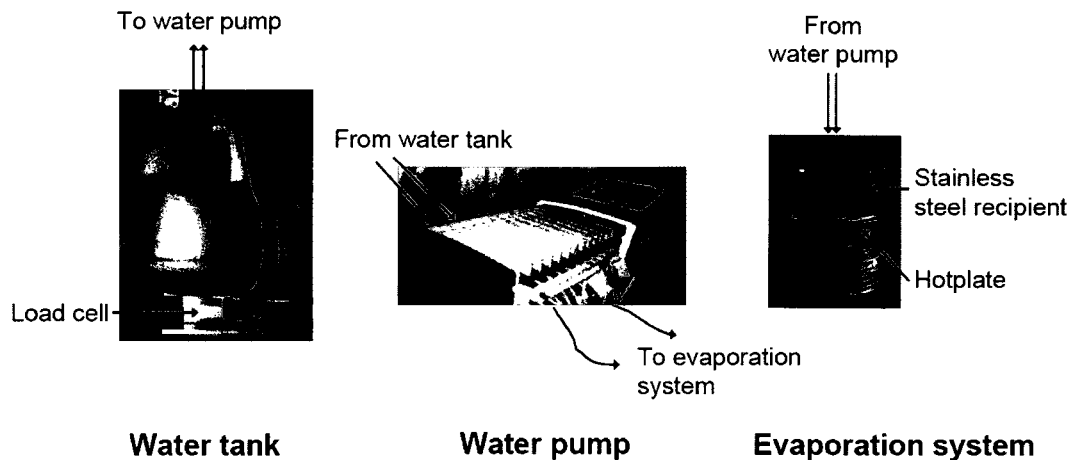
Figure 4.12: Moisture generation system (Yang et al., 2007).

4.6 Instrumentation and monitoring

4.6.1 Monitoring

An extensive monitoring program was carried out. It included the monitoring of outdoor conditions, indoor surface conditions, operation of the ventilating system and heating system, and indoor air condition. The main sensors and instruments employed in the test setup are summarized in Table 4.2.

a. Outdoor conditions

The temperature and RH conditions in the Environmental Chamber were controlled and measured by two temperature sensors (Resistance Temperature Detectors or RTDs) located in the cold box and hot box (T_Cold and T_Hot), and by a RH sensor installed in the hot box (RH_hot). Figure 4.13 shows the location of these sensors.

b. Indoor surface

Surface temperature of indoor surfaces was measured in more than 140 locations. Thermocouples were inserted into the gypsum board surface on the east and west walls, while they were taped with aluminum tape on the surfaces covered with aluminum sheets (ceilings, floors, north and south walls). As example, Figure 4.14 shows a

drawing with the location of thermocouples on the west wall of one room. The same locations were monitored in both rooms.

Table 4.2: Information and specifications of sensors and instruments.

#	Sensor	Location	Characteristics	Picture
1	Thermocouples (quantity: 145)	Indoor surfaces	Type T 30 AWG, PVC insulated & jacketed Accuracy: ±0.3°C Manufacturer: Pelican Wire Co.	
2	1% RH sensor (quantity: 4)	Inlets, Outlets	Model: HMT333 Accuracy*: ±0.6%RH (0...40%RH) ±1.0%RH (40... 97%) ±0.1°C for built-in RTD Manufacturer: Vaisala Instruments	
3	2% RH sensor (quantity: 64)	Across the rooms	Models: HMP50 and Humitter 50Y Accuracy: ±2%RH (10... 90%RH) ±0.5°C for built-in temperature sensor Manufacturer: Vaisala Instruments	
4	Omnidirectional anemometers (quantity: 19)	Across the room	Model: Probe HT 412 and transducer HT428 Accuracy*: 0-1 m/s : ±0.02 m/s ±1% of readings 1-5 m/s: ±3% of readings ±0.2°C for built-in temperature sensor Manufacturer: Sensor Electronics	
5	Power meters (quantity: 4)	Baseboard heaters Hotplates	Model: P4400 Accuracy*: ±0.2% Manufacturer: P3 International	
6	Laminar flow element (LFE) (quantity: 2)	Ventilation system (see Figure 4.5)	Model: 50MC2-2, (capacity100 cfm) with 2110F Smart Flow Gauge Accuracy*: ±1% of reading Manufacturer: Meriam Process Technologies	
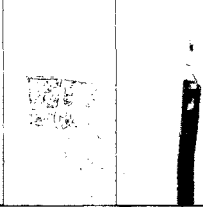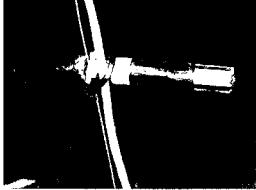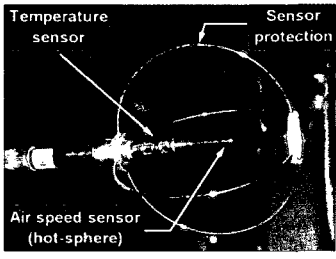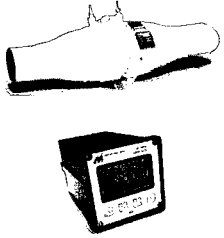
Table 4.2: Information and specifications of sensors and instruments (continued).

#	Sensor	Location	Characteristics	Picture
7	Load cells (quantity: 2)	Moisture Generation system	Model: SCAIME Type AG 2.5kg capacity Accuracy*: 1/4000 (0.025%) Manufacturer: Scaime	

Notes:
* Accuracy specified by the manufacturer.

- Item #1: After installation, thermocouple measurements (averaged over at least 4 hours) from DASs were compared to readings from precision RTD probes, when the temperature in the test rooms and climate chamber reached the same value. The differences were input to the program that manage the DAS and were corrected in the obtain sensor data. This is referred to as the system calibration.

- Item #2: The HMT333 probes have been checked at a few RH levels against the RH calibration chamber with a 0.6%RH chilled mirror sensor; their accuracy statement is reliable. A RTD (resistive temperature detector) is packaged in each probe and it has a good ±0.1°C accuracy.

- Item #3: These sensors had originally a 3% RH accuracy for RH measurements, but they were calibrated to 2% accuracy. The low accuracy of 3% for the probes is because the manufacturer did not calibrate each probe. The RH sensing elements, however, have a better precision and repeatability and thus the measurement uncertainty can be reduced by a full calibration. That full calibration was performed on the probes with more than 20 data points for each, using the RH calibration chamber with a 0.6% chilled mirror RH sensor. A linear calibration relation was obtained for each probe.

  The temperature sensor in each probe was calibrated at one temperature point.

- Item #5: These are consumer grade products and require manual operation and reading.

- Item #7: The load cell accuracy was confirmed by using precisions weights. The same type of load cells was proven reliable in another 200+ day testing project.

c.   Ventilating and heating system

The temperature and RH of the supply air and exhaust air were monitored using RH probes with 1% RH accuracy in the inlet and outlet. The airflow rate was monitored by one laminar flow element for each room.

Power consumption of baseboard heaters and hotplate heaters was monitored using power meters. It was found that the power consumption of the baseboard heaters was influenced by the operation of the hotplates, which were switched on during the moisture generation and switched off during the period without moisture generation. Therefore, power consumption measurements of the baseboard heaters were obtained for both periods.
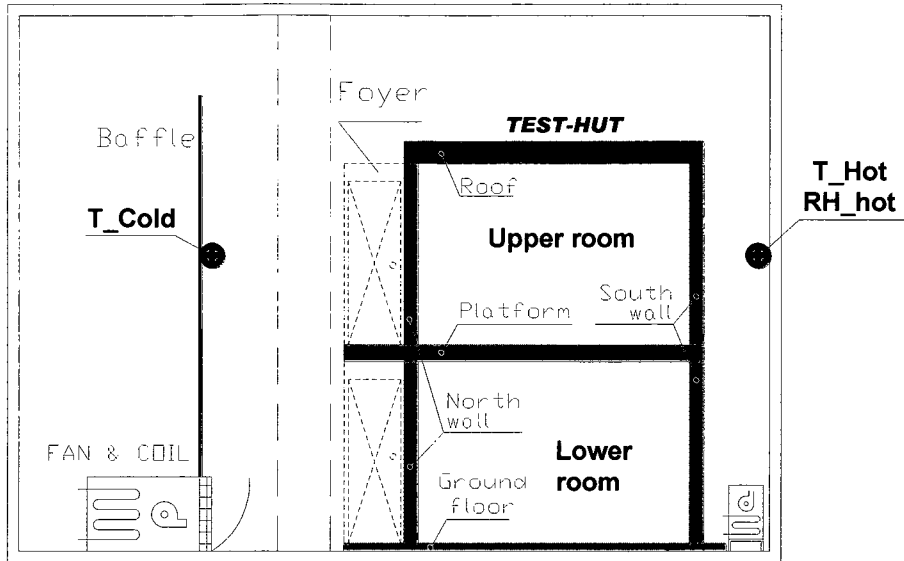
Figure 4.13: Location of sensors monitoring temperature and RH in the Environmental Chamber.
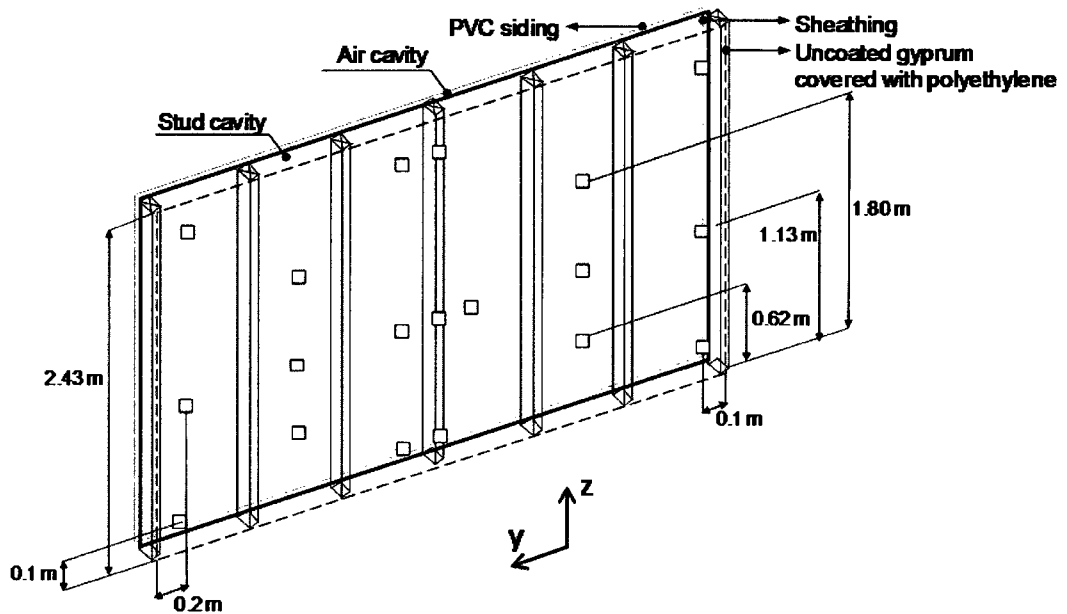
Figure 4.14: Location of thermocouples (□) on the west wall of one room.

d. Indoor air condition

The indoor RH and temperature were monitored by 32 RH sensors placed in each room at different heights (0.10, 1.13, 1.80 and 2.24 m) using the pole mounting system

shown in Figure 4.15. More details of the mounting system of RH sensors are in Vera et al. (2007).
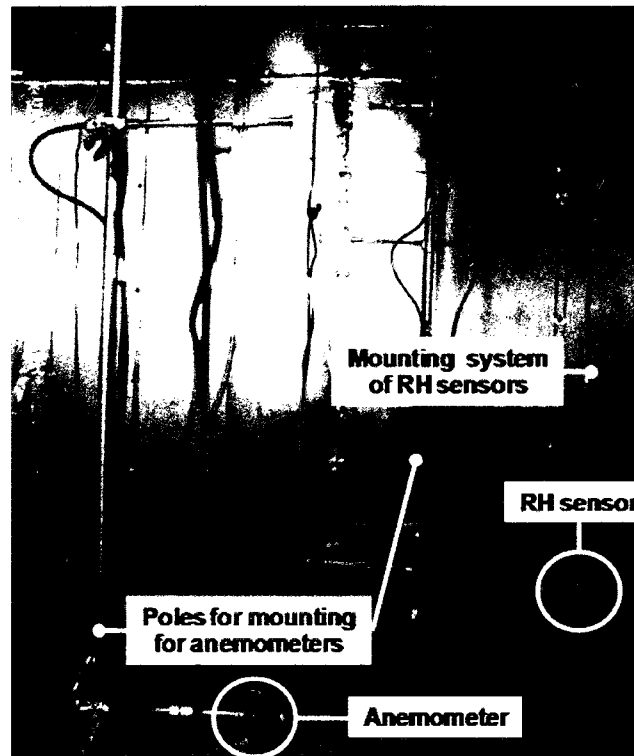
Figure 4.15: Mounting system of RH sensors and omnidirectional anemometers.

An isometric view with the location of the RH sensors either in the lower or upper room is shown in Figure 4.16. An example of the temperature and RH measurements obtained by all 64 RH sensors across the test-hut is presented in Figure 4.17. With the relative humidity and temperature of air measured by the RH sensors, humidity ratio of the air can be calculated at different locations across the room during the test runs.
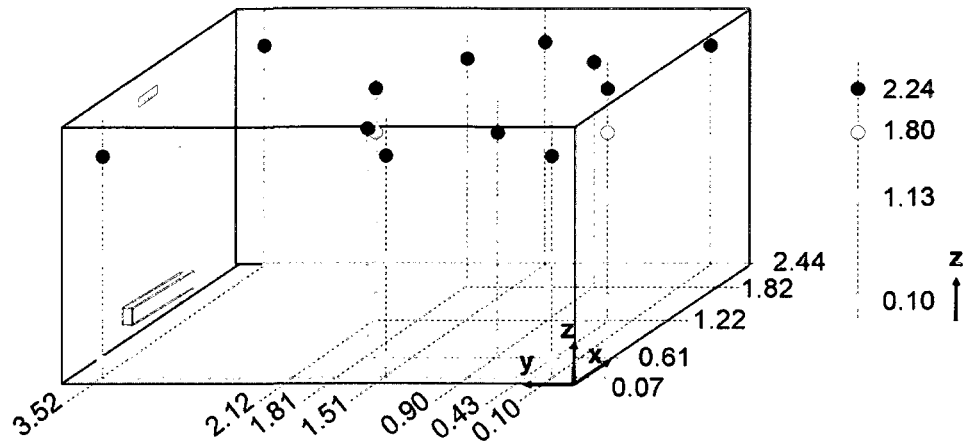
Figure 4.16: Isometric view with the location of RH sensors in each room (dimensions are in meters).
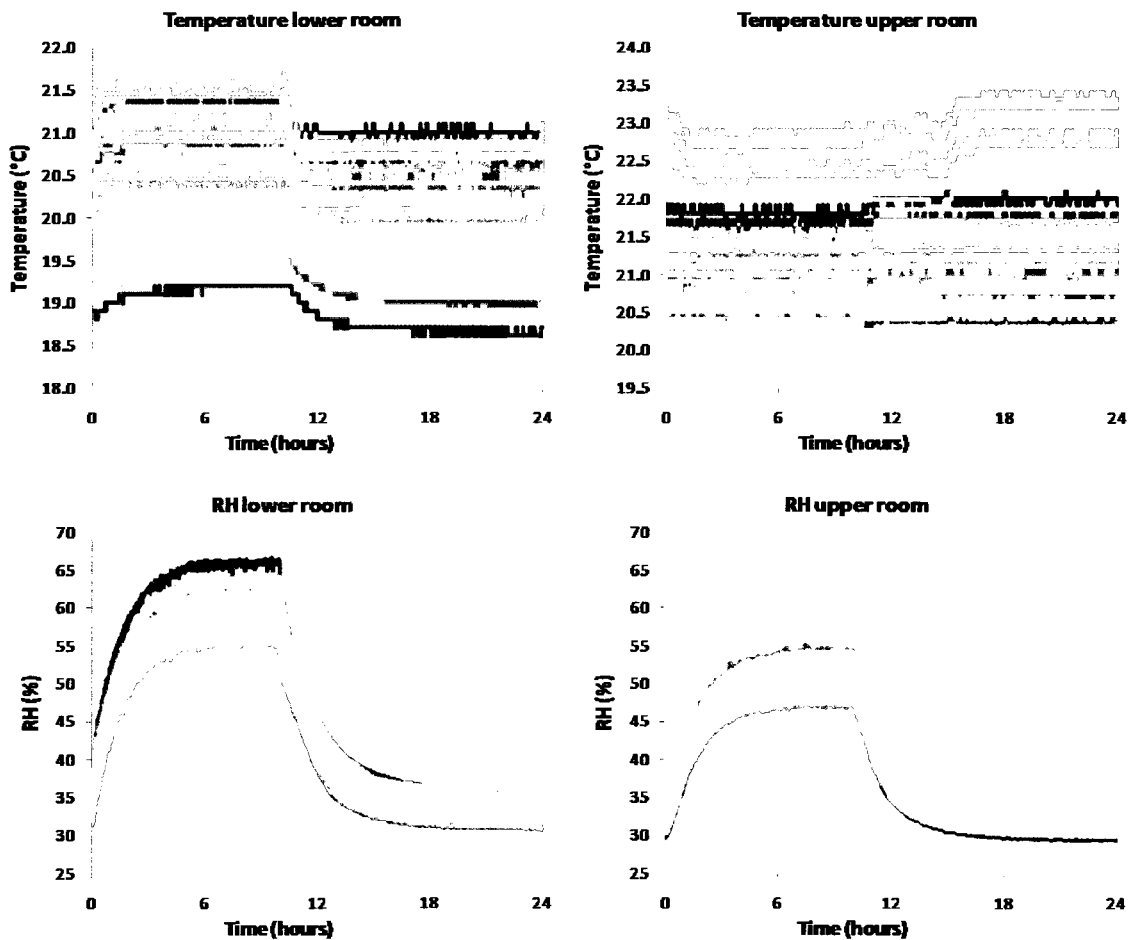
Figure 4.17: Example of temperature and RH measurements obtained with the 64 RH sensors across the two-rooms.

Air speeds and temperatures within each room were measured by 14 omnidirectional anemometers, which were all installed in the longitudinal middle plane of the test-hut (x = 1.22 m) as shown in Figure 4.18. Most of the sensors were placed in vertical planes at y = 1.41 m and y = 2.89 m. One anemometer was placed close to each inlet to monitor the inflow rate. These anemometers were mounted on thin and vertical aluminum poles at different heights (Figure 4.15). Additionally, one anemometer was installed above the baseboard heater on the upper room. In addition, five omnidirectional anemometers were installed across the opening as shown in Figure 4.19. They were kept in place by steel wires connected to the opening edges.
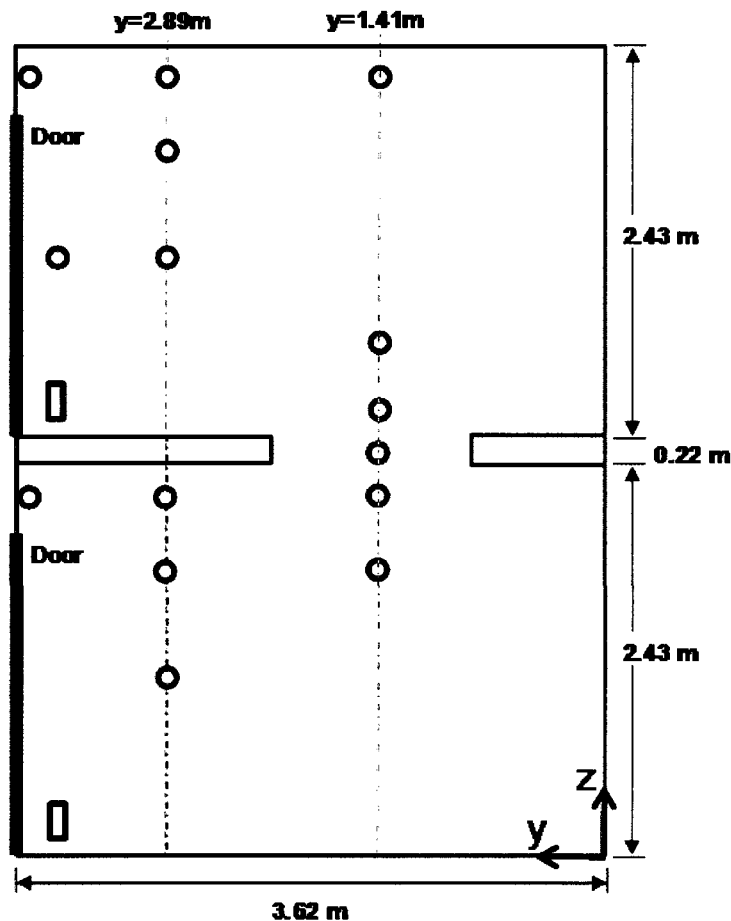
Figure 4.18: Locations of omnidirectional anemometers in the middle vertical plane of the test-hut.
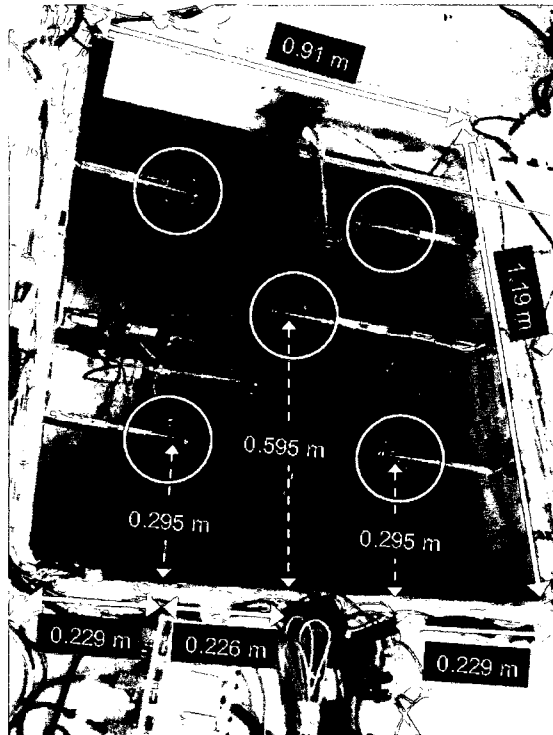
Figure 4.19: Location of omnidirectional anemometers in the opening.

Each anemometer provided both air speed and temperature readings. The measurements with the omnidirectional anemometers were performed every 0.2 seconds (5 Hz), following the recommendations provided by Melikov et al. (1998). Air speed and temperature were averaged every 3 minutes, and a sample of these results is presented in Figure 4.20. It can be seen that higher air speed occurred in the inlet and above the baseboard heater placed in the upper room (note that there is no sensor above the baseboard heater in the lower room). Air speeds across the room and in the opening are much lower. On the other hand, lower temperatures can be seen at the inlet, while higher temperatures were found above the baseboard heater in the upper room.

4.6.2 Data Acquisition System

The Data Acquisition System (DAS) for this project consisted of three units (SCXI system from National Instruments). One unit was used to measure the thermocouples

and RH sensors from each of the two test rooms (Figure 4.21a) and it was placed in the foyer to minimize the wire lengths. An additional unit was located outside the environmental chamber and was used for other measurements (e.g. load cells, climatic chamber condition, etc.). All three DAS units used the same type of data acquisition boards, which had a 16-bit resolution, 200 k samples per second sampling rate. A computer was used to control and communicate with all three units through USB cables.
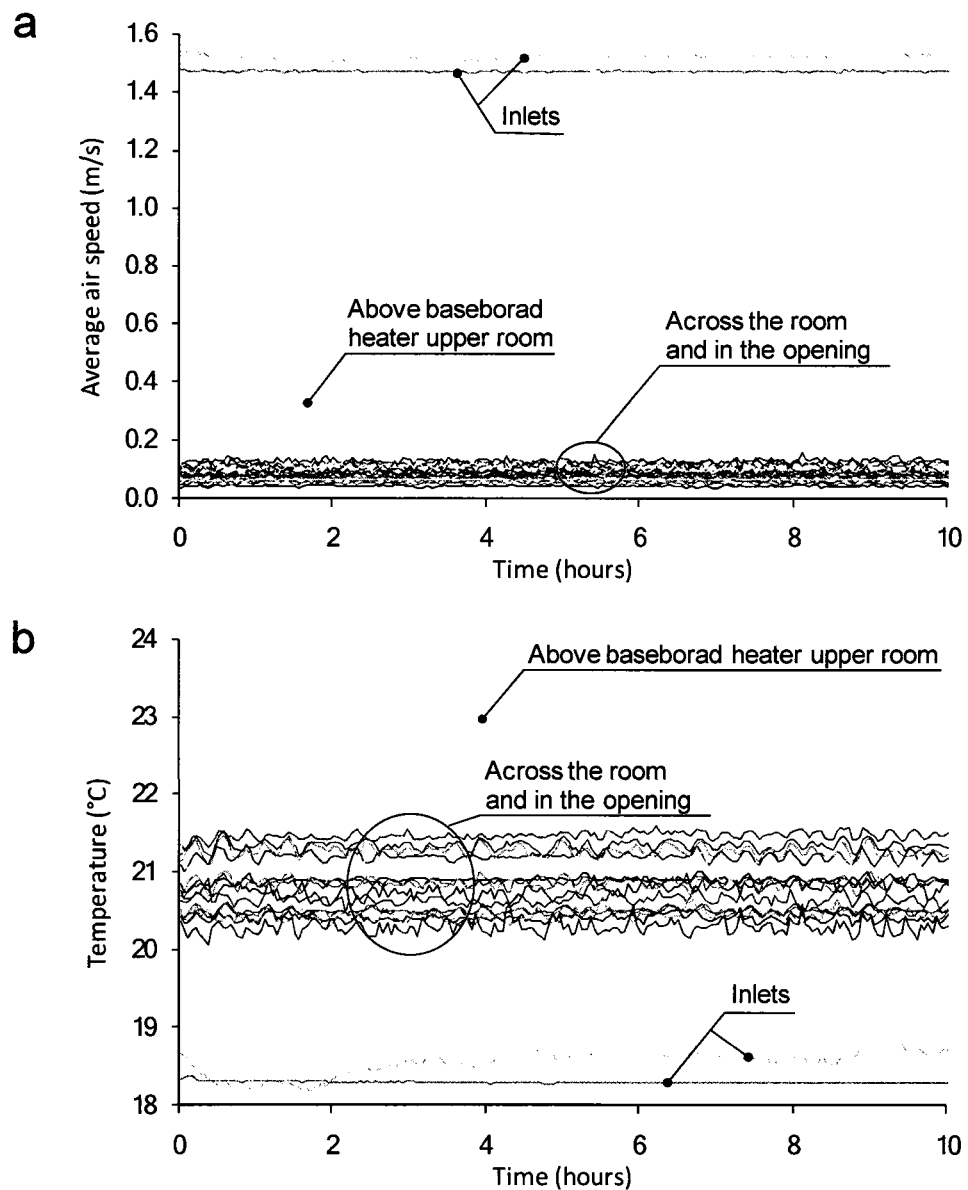
Figure 4.20: Example of measurements by omnidirectional anemometers: a) air speed measurements and b) temperature measurements.

Figure 4.21: Data acquisition system units: (a) for thermocouples and RH, and (b) for omni-directional anemometers.

Leading wires from sensors to DAS units for most sensor types were grouped into 16 or 32 lines using multi-conductor cables or were bundled together by PVC flexible sleeves. Terminal blocks, screw-terminal types (Figure 4.22a) and quick connector types (Figure 4.22b and 4.22c) were used for thermocouple and RH sensors, respectively. The use of the cables and terminal blocks greatly facilitated the installation and trouble-shooting of the wires, connections and sensors.
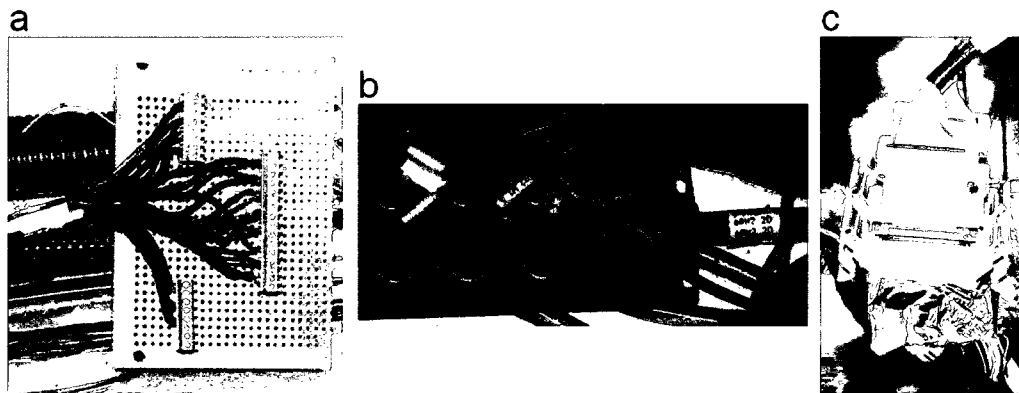
Figure 4.22: (a) Screw-terminal type for thermocouples, (b) group connector box for RH sensors, and (c) terminal block for RH sensors.

Data were taken at intervals of 0.5, 1 or 5 minutes, depending on the experimental characteristics. Each measurement, one value in the data files, of a sensor was the average of 10 consecutive readings (DA conversions) that were taken at 600 Hz.

Air speed and temperature data from the anemometers were collected by three manufacturer-provided measurement stations HT-480 (Figure 4.21b). Sampling was performed at 5 Hz continuously during testing.

4.7 Cases tested and test conditions

Twenty different cases were tested to estimate the moisture exchange between the two rooms and the interzonal mass airflows through the opening, and to investigate the influence of the difference in average temperature between the two rooms (ΔT), ventilation strategy, ventilation rate and moisture source location on the interzonal air and moisture exchange between the two rooms. Figure 4.23 shows a sketch with the cases tested arranged in four scenarios, and Table 4.3 shows the main tested conditions of each case.
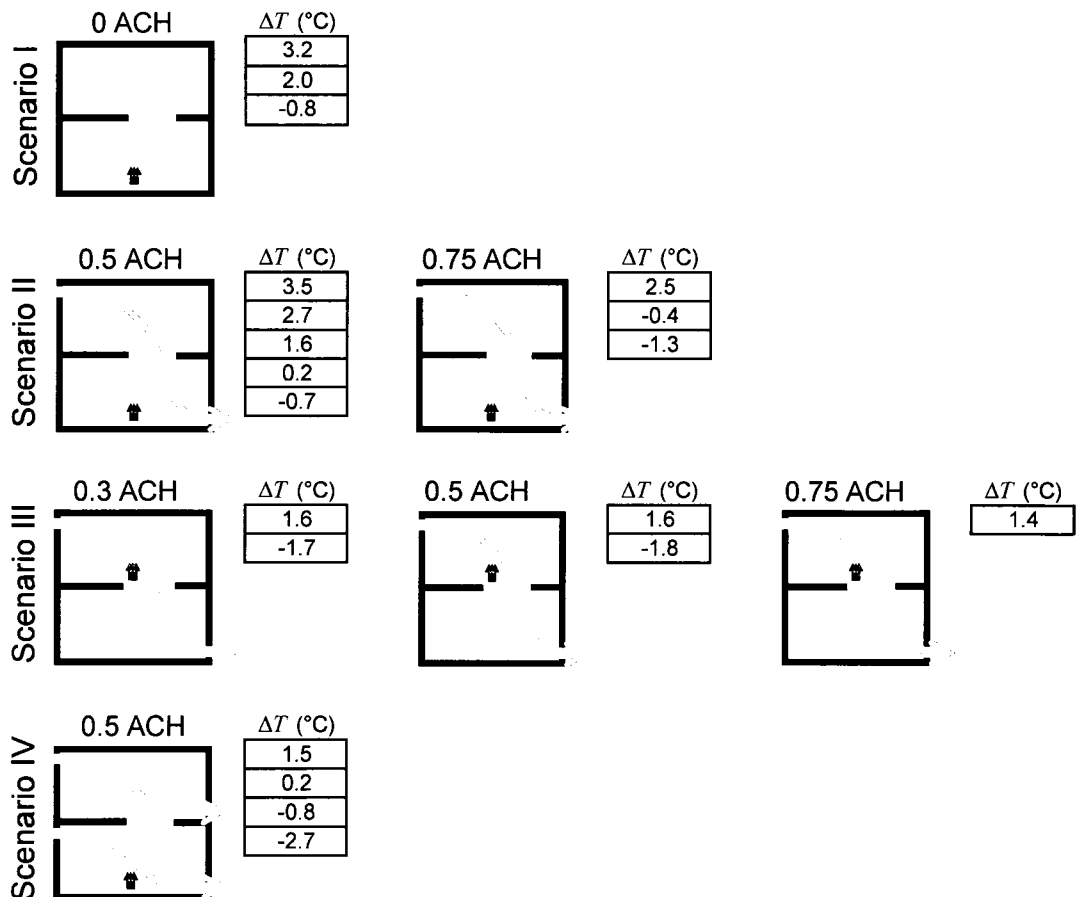
Figure 4.23: Main parameters tested.

Table 4.3: Cases tested and their main conditions.

Scenario	Cases	ΔT (°C)	Ventilation strategy	Ventilation rate[1] (ACH)	Moisture source location	Moisture generation rate (g/h)
I	1-1	+3.2	No	0	Lower	108.5
	1-2	+2.0	ventilation	0	room	106.6
	1-3	-0.8		0		106.4
II	2-1	+3.5	Single	0.50	Lower	109.4[2]
	2-2	+2.7	ventilation	0.50	room	109.4[2]
	2-3	+1.6	with	0.50		109.4[2]
	2-4	+0.2	downward	0.50		109.4[2]
	2-5	-0.7	net flow	0.50		109.1
	2-6	+2.5	through the	0.75		108.7
	2-7	-0.4	opening	0.75		108.4
	2-8	-1.3		0.75		108.6
III	3-1	+1.6	Single	0.30	Upper	113.8
	3-2	-1.7	ventilation	0.30	room	114.4
	3-3	+1.6	with	0.50		114.1
	3-4	-1.8	downward	0.50		112.0
	3-5	+1.4	net flow through the opening	0.75		113.0
IV	4-1	+1.5	Independent	0.50	Lower	109.4
	4-2	+0.2	ventilation	0.50	room	109.6
	4-3	-0.8	in each	0.50		105.7
	4-4	-2.7	room	0.50		106.5

[1] Nominal values of ventilation rates correspond to the air change rate for the whole volume of the two-story test-hut.

[2] The moisture generation rate was not measured for these cases due to a malfunction of the DAS to measure the reference voltage for the load cell beneath the water tank. The moisture generation rates for the test before and the test after this problem were 109.0 and 109.4 g/h, respectively.

The conditions tested are described as follows:

a. General test conditions

The outdoor conditions, air supply conditions and the moisture generation rate were kept the same for all tests. The measured outdoor conditions were -4.7 ± 0.2°C and 68 ± 4%RH. The supply air condition was kept constant at around 18°C and 38%RH for all cases. The nominal moisture generation rate was 100 g/h, which simulated the typical moisture generation rate in a two-persons bedroom. This rate of moisture generation is due to mainly people's respiration based on data found in Sanders (1996). The measured moisture generation rate was between 6% and 14% higher than the

nominal value as shown in Table 4.3, and it was not possible to keep it the same for all cases. However, the variations found among the same scenario are low and acceptable.

b.   Temperature difference between the lower and the upper rooms

Several temperature differences between the lower and the upper rooms (ΔT) were set by changing the set point of the thermostat in the two rooms. In cases where a much colder upper room was desired, the baseboard heater in the upper was switched off. The temperature difference is considered as the difference between the average room temperatures and it ranged from about -2.7°C to +3.5°C. ΔT is negative when the upper room is warmer than the lower room, while ΔT is positive when the upper room is colder than the lower room. The average temperature in each room was obtained averaging the temperature measurements from the 32 RH sensors in each room for the last 30 minutes of the moisture generation period.

c.   Ventilation strategy and moisture source location

Four different scenarios of ventilation strategies and moisture source locations were tested as shown in Figure 4.24. Three different ventilation strategies were implemented: no ventilation (scenario I), single ventilation with downward net flow through the opening (scenarios II and III), and independent ventilation in each room (scenario IV). The moisture source was placed either on the lower floor or the upper floor.

d.   Ventilation rate

Ventilation rates shown in this thesis research correspond to the air change for the whole volume of the two-story test-hut. Most of the cases were carried out at 0.5 ACH, but other ventilation rates were also tested. No ventilation (0 ACH) was tested in scenario I, 0.3 ACH was tested in scenario III and 0.75 ACH was tested in scenarios II and III.
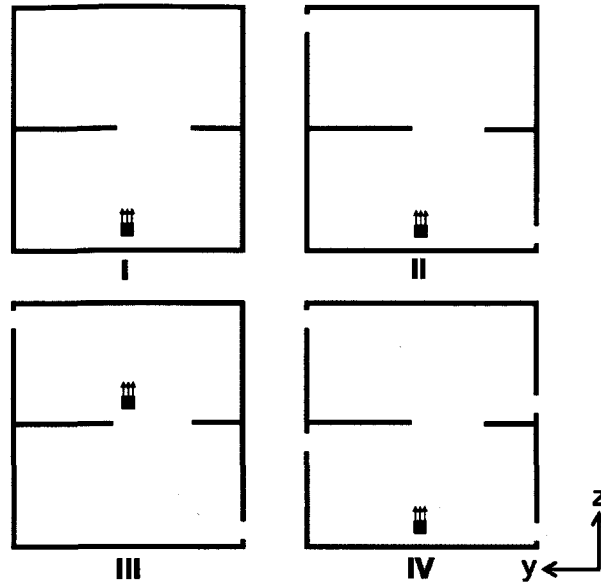
Figure 4.24: Scenarios tested for combined ventilation strategy and moisture source locations.

In most of the cases, each case tested lasted for 3 days and consisted of 3 daily cycles. Each day-cycle was characterized by an increase of indoor HR during the moisture generation period, followed by a decay of HR during the period without moisture generation. Temperature was higher (~0.5°C) during the moisture generation period in the room where moisture was generated because of the hotplate operation. Figure 4.25 shows the average HRs and temperatures in each room. It can be observed that the plotted results are very similar among the three daily-cycles; however, during the first day the indoor conditions were usually disturbed during the setting tasks. For this reason, the results analysed herein correspond to the data measured for either the second day-cycle or the third day-cycle.

4.8 Measurement uncertainties

The measurement accuracies of the main sensors employed in the experiments are presented in Table 4.2. Among all measurements, air speeds, air temperatures and HRs are the base of this study because they allow validating the CFD model and investigating the moisture exchange between the two rooms and the interzonal mass

airflow through the opening. For these reasons, an uncertainty analysis of these measurements is described below:
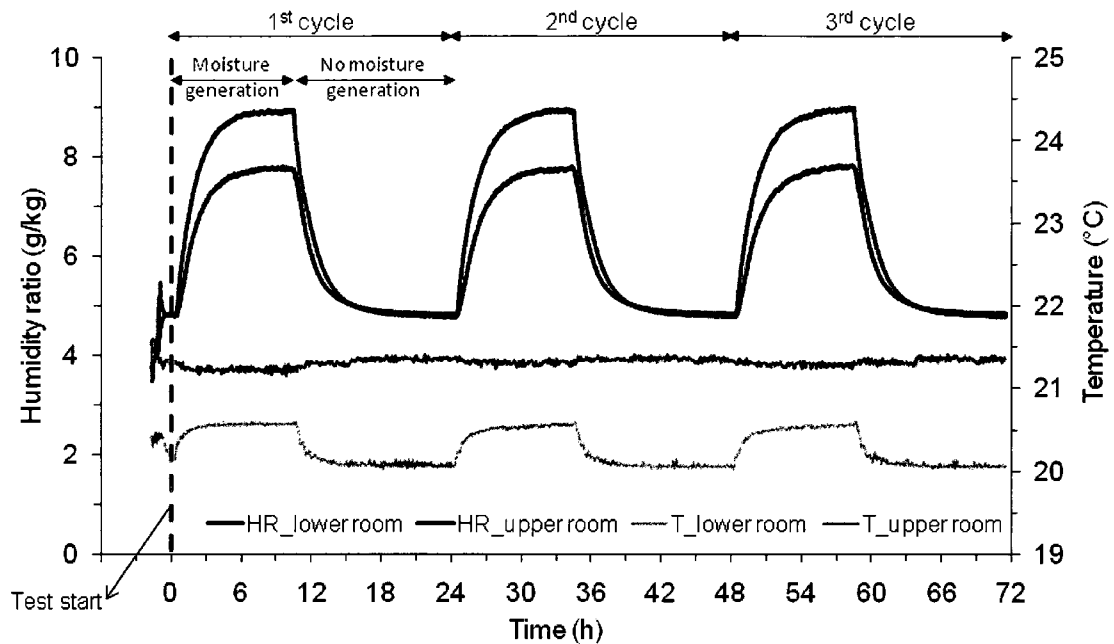
Figure 4.25: Repeatability of average indoor conditions (HR and temperature) over a three-day test.

4.8.1 Temperature

Air temperatures were monitored by the omnidirectional anemometers and the RH sensors, which have accuracies of ±0.2°C and ±0.5°C, respectively. The accuracy of the omnidirectional anemometers was provided by the manufacturer. Brand-new omnidirectional anemometers were acquired for this investigation, thus no calibration was deemed as necessary. RH sensors were calibrated to improve the original RH accuracy of 3%RH to 2%RH. Every sensor was calibrated at more than 20 points using a RH calibration chamber with a 0.6%RH accuracy chilled mirror RH sensor. At the same time, the temperature of the sensor was read at each data point and the readings were found to vary less than 1°C over the calibration of each set of sensors. Thus the temperature sensor in each RH probe was calibrated at one temperature point.

4.8.2 Humidity ratio

The humidity ratio values are calculated from the temperature and RH readings of the 2% RH probes. Humidity ratio (w) depends on the atmospheric pressure (P) and partial vapor pressure (p_v). The measurement uncertainty of the humidity ratio depends mainly on the measured partial vapor pressure and its measurement uncertainty, thus the standard uncertainty of the humidity ratio (u_w) can be calculated using the following equation:

$$u_w = \left(\frac{\partial w}{\partial p_v}\right) u_{p_v} = 0.2 \ g/kg \tag{4.1}$$

where w is the humidity ratio or HR (g/kg or kg/kg), p_v is the partial vapor pressure (Pa), and u_{p_v} is the standard uncertainty of the partial vapor pressure (Pa). Since the partial vapor pressure depends on the saturation vapor pressure (at the measured temperatures) and the measured RHs, the uncertainty of the partial vapor pressure (u_{p_v}) needs to be calculated. This calculation is provided in Appendix A.

The standard uncertainty of HR, u_w, corresponds to a 68% level of confidence. Then the expanded uncertainty of the humidity ratio, U_w (95% level of confidence), is ±0.46 g/kg using a coverage factor of 2.26.

4.8.3 Air speed

The omnidirectional anemometers used in this study are specially designed to measure low air speed with a range between 0.05 and 5 m/s and are known as low velocity thermal anemometers (LVTA). Popiolek et al. (2007) identified 15 sources of errors related to LVTAs (e.g. natural convection, directional sensitivity, calibration reference, etc.). They quantified the total uncertainty of LVTAs using a database of instantaneous air velocities measured with Laser Doppler Anemometers and they also

modeled the impact of some error sources, such as natural convection, directional sensitivity and dynamic response of anemometers.

The estimation of the uncertainty of LVTAs is complex and requires specialized equipment. However, Melikov et al. (2007) estimated the total uncertainty of four types of LVTAs available in the market, A, B, C and D (Figure 4.26). The LVTA type D is the same as those used in this thesis research. Melikov's results can be used to estimate the uncertainty measurements for the range of air speed measured in this study.
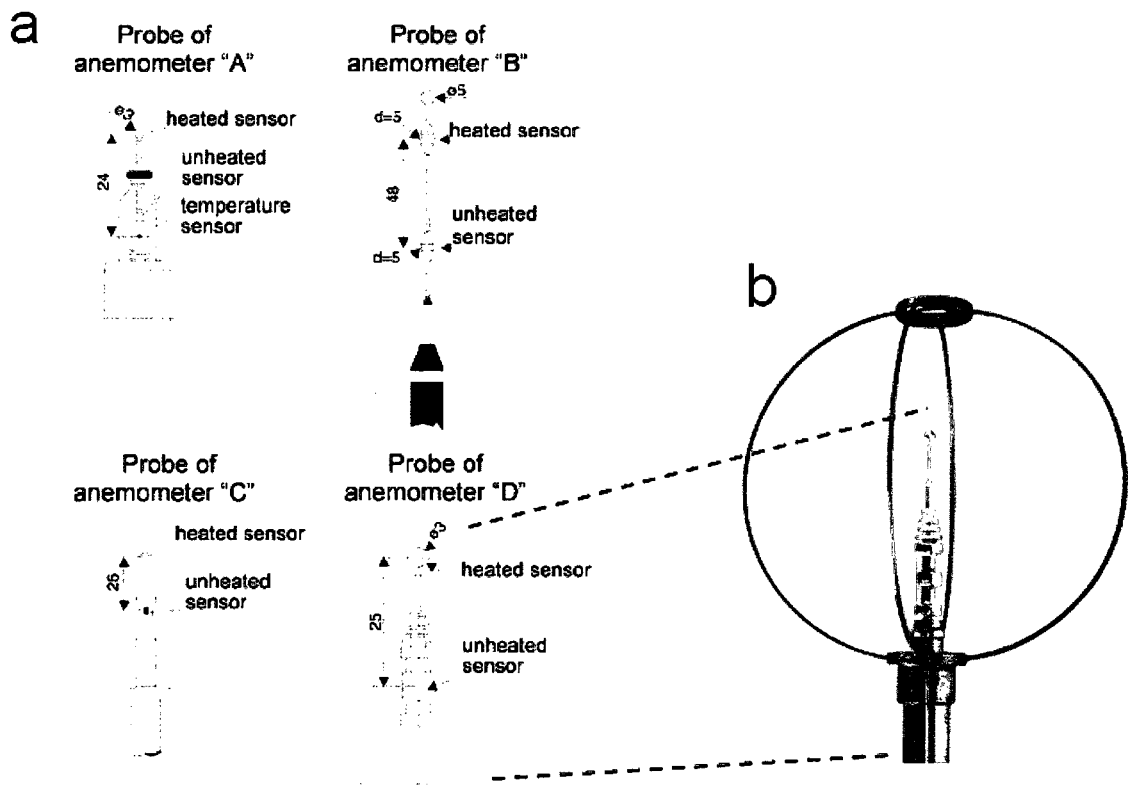
Figure 4.26: a) Types of LVTAs studied by Melikov et al. (2007) and b) omnidirectional anemometers used in the current investigation.

Melikov et al. (2007) indicate that the expanded uncertainty of the mean air speed ($\bar{V}$) for the type D anemometer probe is given by:

$$U_{\bar{V}} = -0.0053 \cdot \bar{V}^2 + 0.0262 \cdot \bar{V} + 0.0214 \tag{4.13}$$

Figure 4.27 plots the expanded uncertainty of the air speed between 0.05 and 0.3 m/s, which is the air speed range measured across the two rooms and into the opening. It can be observed that the uncertainty varies from 0.023 to 0.029 m/s, which is higher than the accuracy provided by the manufacturer of the omnidirectional anemometers. Also, the relative uncertainty is very large (~ 35 to 45%) for air speed measurements at the low limit just above 0.05 m/s, and it decreases up to 10% for air speeds near 0.3 m/s.
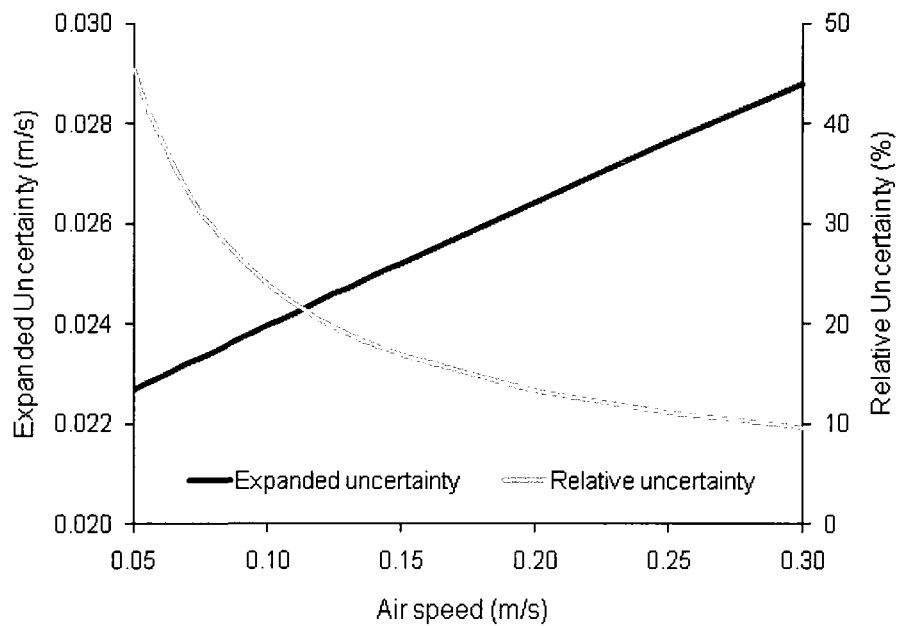
Figure 4.27: Expanded uncertainty and relative uncertainty of the omnidirectional anemometer used in this thesis.

CHAPTER 5

EXPERIMENTAL RESULTS AND ANALYSIS

5.1 Introduction

In this chapter an analysis is carried out on the air and moisture transports between the two rooms based on experimental data by studying the following two physical quantities:

- Steady-state difference between the average humidity ratios of the two rooms (ΔHR), which is defined as the average HR in the moisture source room over the last 30 minutes of the moisture generation period subtracted by the average HR in the other room over the last 30 minutes of the moisture generation period. ΔHR is expressed in unit mass of water vapor (g or kg) per kg of dry air, and indicates the degree of moisture exchange between the two rooms. Higher ΔHR values mean a low interzonal moisture exchange, while smaller ΔHR values indicate a high interzonal moisture exchange. ΔHR values are calculated over the last 30 minutes of the moisture generation, period in which steady-state humidity ratios are obtained for all cases tested. The influences of ΔT, ventilation strategies, and moisture source locations on ΔHR are addressed in section 5.2.

- Measured interzonal mass airflows (F). Interzonal airflows through horizontal openings also carry the moisture in the air and directly influence the moisture exchange between different zones. If the water vapor is considered as a single tracer gas that is released at constant rate, the upward and downward mass airflows through the opening can be estimated based on the temporal profiles of humidity ratios in each room that are obtained experimentally. The influences of ΔT and ventilation strategies on the interzonal mass airflows are presented in section 5.3.

Herein, interzonal mass airflows denote the transport of dry air only. Thus, they are expressed as kg of dry air per second; while the movement of water vapor carried by the airflow is referred to the moisture transport.

5.2   Interzonal moisture exchange through the horizontal opening

5.2.1 Procedure

The concentration of water vapor in the air is expressed as the humidity ratio in grams or kilograms of water vapor per kg of dry air (g/kg or kg/kg). HR values can be calculated from RH and temperature readings of the 32 RH probes installed across each room. Figure 5.1 shows the temporal HR profiles in the lower and upper rooms for case 4-1, the solid lines are the average HRs in each room while the shaded bands delimit the maximums and minimums HR values from all 32 RH probes located in each room.
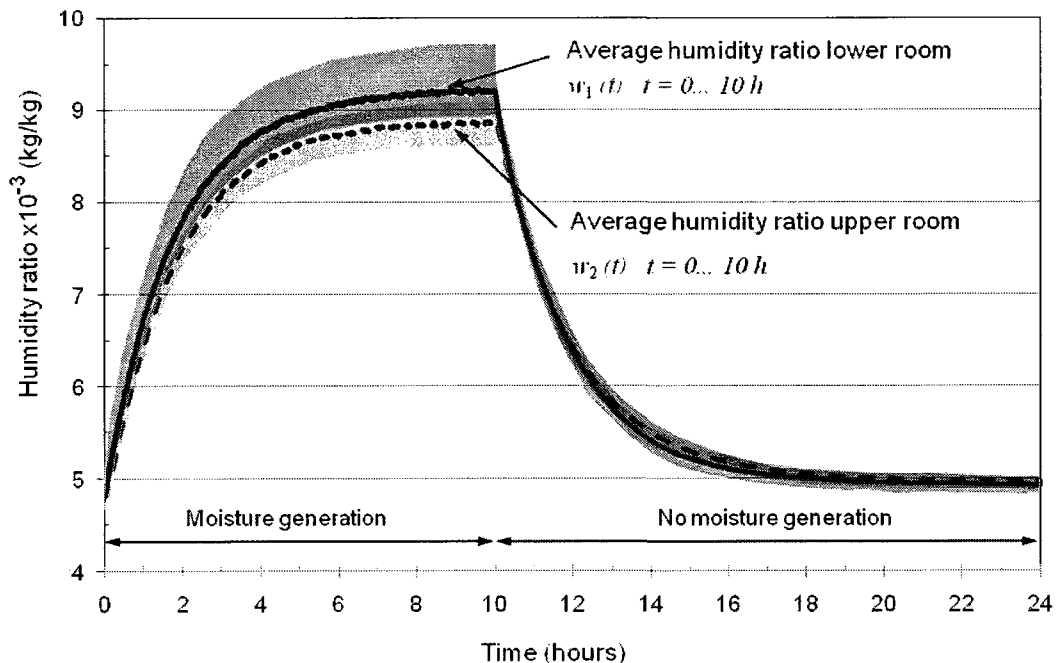
Figure 5.1: Measured average temporal HR profiles in each room and maximum and minimum HR ranges delimited by shaded bands in each room for case 4-1.

It can be observed in Figure 5.1 that the humidity level increases immediately after the moisture generation starts (t = 0) in the lower room (the moisture source room) and

in the upper room. This means that the water vapor not only moves fast across the moisture source room, but also is transported without any delay to the upper room. Therefore, the moisture exchange between the two rooms occurs as soon as the moisture generation starts. Also, Figure 5.1 shows that steady-state humidity level is reached at the end of the moisture generation period. The shaded bands in each room show that the HR is not uniform across each room. Similar results were found for the other cases for scenarios II, III, and IV.

Comparisons among different cases based on the temporal HR profiles are, while very illustrative and revealing, qualitative. A quantitative approach based on the average steady-state HR data is used. In this approach, ΔHR is obtained for each case to evaluate the influences of ΔT, of the ventilation strategies, and of the locations of the moisture source on the moisture exchange between the two rooms. This approach was not applied for scenario I (cases 1-1, 1-2 and 1-3) where steady-state conditions were not reached during the short 3 hours moisture generation period that was set for these cases without ventilation.

5.2.2 Results

a.   Influence of temperature difference

Figure 5.2 compares ΔHR values (ΔHR is given by the height of the bar; the top of the bar corresponds to the average HR in the room where moisture source is placed, whereas the bottom of the bar shows the average HR in the other room) for scenarios II, III and IV at different values of ΔT. It is observed that higher ΔHR values occurred when the upper room was warmer than the lower room, whereas lower ΔHR values were found when the upper room was colder. For instance, cases in scenario IV (Figure 5.2d) show that ΔHR was about 1.6 g/kg at a temperature difference of -2.7°C, while it decreased to 0.34 g/kg at +1.5°C. This result reveals that higher interzonal moisture exchange occurs

when the upper room is colder, whereas the moisture exchange between the two rooms is low when the upper room is warmer.

Also, Figure 5.2 shows that ΔT influences the average humidity level in the rooms. When the moisture source is placed in the lower room, the average HR in the upper room (bottom of the bar in Figures 5.2a, 5.2b and 5.2d) depends significantly on ΔT. Average HR in the upper room was much lower when the upper room was warmer, and increased significantly when the upper room was colder. This shows that the warmer upper room led to a significantly smaller amount of moisture moving up through the opening from the moisture source.
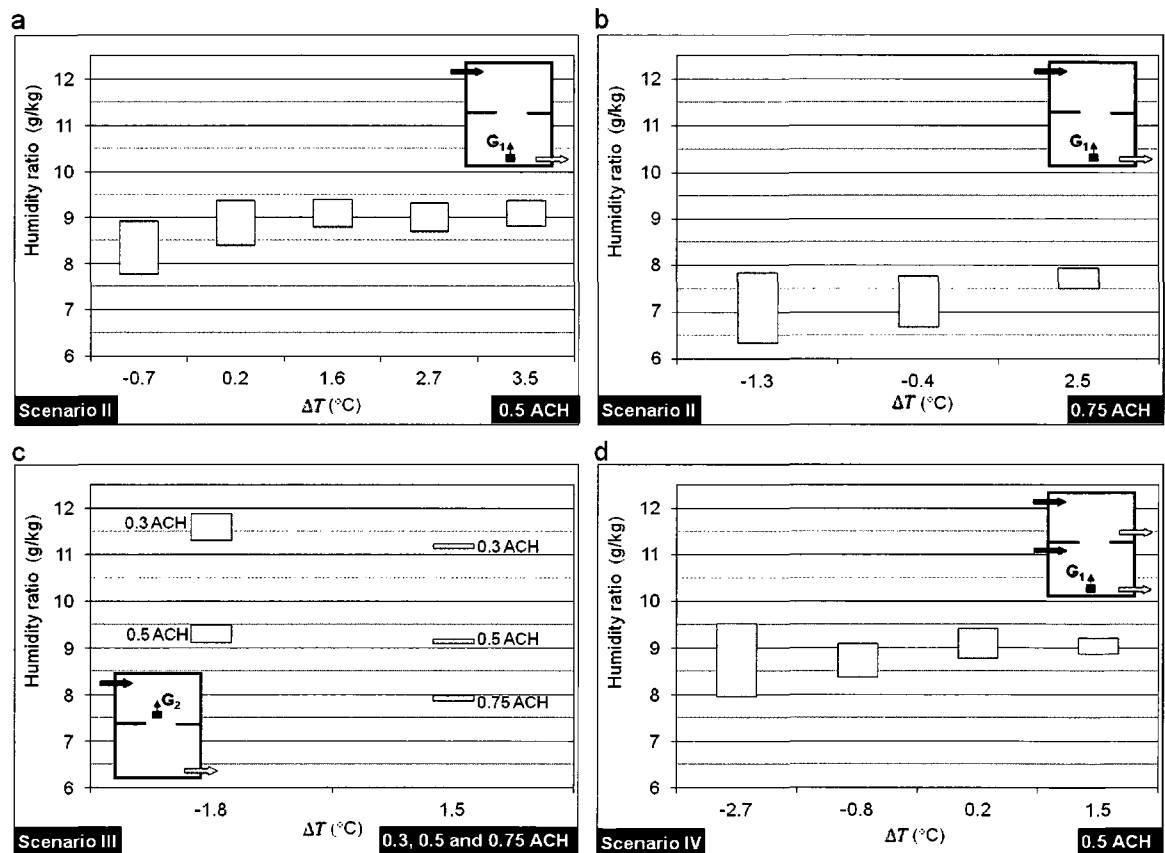
Figure 5.2: Influence of ΔT, ventilation strategies, ventilation rates and moisture source locations on interzonal moisture exchange. The bar height represents ΔHR. The top of the bar corresponds to the average HR in the room where moisture source is placed, whereas the bottom of the bar shows the average HR in the other room.

b.   Influence of moisture source locations

Figure 5.2c shows ΔHR when the moisture source is placed in the upper room. Unlike scenarios II and IV, higher HR levels occur in the upper room in scenario III. Comparing scenarios II (Figs. 5.2a and 5.2b) and III (Fig. 5.2c), which have different locations of the moisture source but the same ventilation strategy, it can be observed that ΔHR values are smaller for scenario III at any ventilation rate. This condition is due to water vapor, generated in the upper room, is being transported to the lower room by the downward net flow through the opening, contributing to the air and moisture mixing between the two rooms.

c.   Influence of ventilation strategy

The influence of the ventilation strategy on the moisture exchange between the two rooms is shown in Figure 5.3. The ΔHR values for single ventilation with downward net flow through the opening (scenario II) and independent ventilation in each room (scenario IV) are compared at three values of ΔT. The ΔHR values are smaller for independent ventilation than those for single ventilation at all three ΔT values shown. These lower values for ΔHR may be attributed to higher interzonal moisture exchange in cases with independent ventilation as compared to cases with single ventilation. This condition agrees well with the fact that the strong downward net flow through the opening in scenario II restricts upward transport of warm and moist air from the lower room through the opening. Also, Figure 5.3 reveals that the influence of the ventilation strategy is much smaller when the upper room is colder.
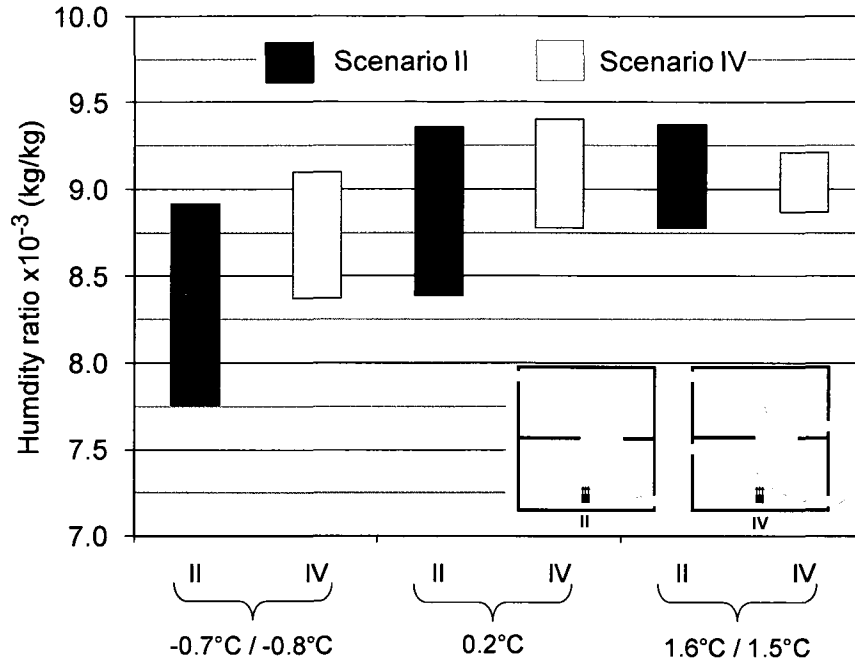
Figure 5.3: Comparison of ΔHR between scenarios II and IV at 0.5 ACH. The bar represents ΔHR. The top of the bar height corresponds to the average HR in the lower room, whereas the bottom of the bar shows the average HR in the upper room.

5.3 Measured interzonal mass airflows

5.3.1 Procedure

Interzonal airflows are commonly calculated based on tracer gas techniques (decay, constant injection and constant concentration methods) with one or multiple gases. In this thesis, water vapor is considered as a single tracer gas that was released at a constant rate. Moisture transport through horizontal openings is determined by the interzonal airflows, and the specific vapor concentrations (HRs) in the two rooms are results of all the moisture inflows and outflows. This interdependency can be encompassed more precisely by the mass balance equations for moisture masses and air masses in both test rooms. The generic form of the water vapor mass balance for the four scenarios is given by:

$$\dot{w}_1(t) = a_{11} \cdot w_1(t) + a_{12} \cdot w_2(t) + m_1(t) \tag{5.1}$$

$$\dot{w}_2(t) = a_{21} \cdot w_1(t) + a_{22} \cdot w_2(t) + m_2(t) \tag{5.2}$$

The temporal profiles of humidity ratios in each room during the moisture generation period, $w_1(t)$ and $w_2(t)$, correspond to the average HR in the lower and upper rooms, as shown in Figure 5.1 for case 4-1. Coefficients a_{ij} and sources m_i are different for different scenarios. For each scenario, all the moisture fluxes involved, source, and sink terms are shown in Figure 5.4; and the expressions for all coefficients a_{ij} and sources m_i are obtained and shown in Table 5.1.
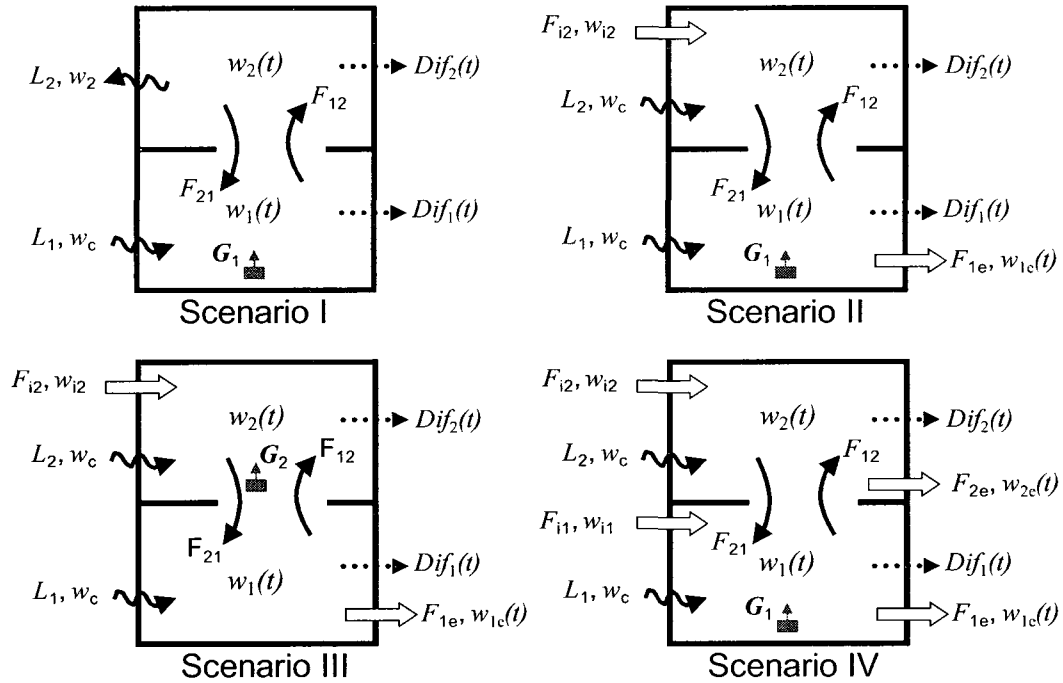
Figure 5.4: Air and moisture flows involved in the air and moisture balance equation for each scenario.

Eqs. 5.1 and 5.2 can be integrated over the moisture generation periods into time-integral equations as follows:

$$w_1(\tau) - w_1(0) = a_{11} \cdot \int_0^\tau w_1(t)dt + a_{12} \cdot \int_0^\tau w_2(t)dt + \int_0^\tau m_1(t)dt \tag{5.3}$$

$$w_2(\tau) - w_2(0) = a_{21} \cdot \int_0^\tau w_1(t)dt + a_{22} \cdot \int_0^\tau w_2(t)dt + \int_0^\tau m_2(t)dt \qquad (5.4)$$

where τ is the duration of the moisture generation period, which is 10,800 s (or 3 h) for

scenario I and 36,000 s (or 10 h) for scenarios II and IV.

Table 5.1: Terms for the water vapor and air mass balance equations for different ventilation strategies[1,2].

	Scenario I	Scenario II	Scenario IV
a_{11}	$-\dfrac{F_{12}}{\rho_1 V}$	$-\dfrac{F_{12}}{\rho_1 V}$	$-\dfrac{F_{12}}{\rho_1 V}$
a_{12}	$\dfrac{F_{21}}{\rho_1 V}$	$\dfrac{F_{21}}{\rho_1 V}$	$\dfrac{F_{21}}{\rho_1 V}$
a_{21}	$\dfrac{F_{12}}{\rho_2 V}$	$\dfrac{F_{12}}{\rho_2 V}$	$\dfrac{F_{12}}{\rho_2 V}$
a_{22}	$\dfrac{-F_{21} + L_2}{\rho_2 V}$	$-\dfrac{F_{21}}{\rho_2 V}$	$-\dfrac{F_{21}}{\rho_2 V}$
m_1	$\dfrac{G_1 + L_1 w_c - Dif_1}{\rho_1 V}$	$\dfrac{G_1 + L_1 w_c - F_{1e} w_{1e} - Dif_1}{\rho_1 V}$	$\dfrac{G_1 + L_1 w_c + F_{i1} w_{i1} - F_{1e} w_{1e} - Dif_1}{\rho_1 V}$
m_2	$-\dfrac{Dif_2}{\rho_2 V}$	$\dfrac{F_{i2} w_{i2} + L_2 w_c - Dif_2}{\rho_2 V}$	$\dfrac{F_{i2} w_{i2} + L_2 w_c - F_{2e} w_{2e} - Dif_2}{\rho_2 V}$
$\sum F_{ij} = $ $\sum F_{ji}$	$F_{12} = F_{21} + L_1$ $L_1 = L_2$	$F_{21} + L_1 = F_{12} + F_{1e}$ $L_2 + F_{i2} + F_{12} = F_{21}$	$F_{21} + F_{i1} + L_1 = F_{12} + F_{1e}$ $F_{12} + F_{i2} + L_2 = F_{21} + F_{2e}$

[1] Coefficients for scenario III are not shown here because good interzonal mass airflows were not obtained for this scenario.

[2] Diffusion through the East and West walls in the lower and upper rooms is given by:

$$Dif_i = M_c \times A \times \Delta t \times (p_{v,i} - p_{v,c}) \quad i = lower\ room\ or\ upper\ room$$

where, M_c is the wall combined permeance, which was calculated equal to 1.5×10^{-11} kg/s·m²·Pa, $p_{v,i}$ is the partial water vapor pressure in room i (Pa), and $p_{v,c}$ is the partial water vapor pressure in the environmental chamber (Pa), and Δt is the time interval over which moisture diffusion is calculated.

Air mass balance equations are established by equating the total air mass airflow

entering a room to that leaving the room for the upper and the lower rooms. For

instance, Eqs. 5.5 and 5.6 are the air mass balance equations for scenario II. The exact

forms of these equations are different for different scenarios as can be seen in Table 5.1.

$$F_{21} + L_1 = F_{12} + F_{1e} \qquad (lower\ room) \tag{5.5}$$

$$L_2 + F_{i2} + F_{12} = F_{21} \qquad (upper\ room) \tag{5.6}$$

The unknowns in the set of Eqs. 5.3 to 5.6 are the interzonal mass airflow rates through the opening in either the upward (F_{12}) or downward (F_{21}) direction, while all other flow rate terms involved are determined from the experimental data. Therefore, solutions to the interzonal airflow rates can be obtained by solving either Eqs. 5.3 and 5.5 for the lower room or Eqs. 5.4 and 5.6 for the upper room. However, it is found that different interzonal mass airflows are obtained depending on which of the two sets of equations is used. This difference arises from a vapor mass imbalance in the two-story test-hut, for example, the total vapor mass entering and generated in the test hut does not equal exactly the vapor mass leaving the test hut. The vapor imbalance in the test-hut may be caused by measurements errors of humidity ratios for the room air volume, supply air, exhaust air, and environmental chamber; by estimation errors of air leakage; and by non-well mixed air conditions within each room. Consequently, the calculated upward and downward mass airflows are taken as the average of the values calculated from both sets of equations. Appendix B provides more details about the vapor mass imbalance in the test-hut.

5.3.2 Measured interzonal mass airflows and average air speed across the opening

Table 5.2 lists the upward mass airflows that were calculated according to the above procedure for each case. Cases with the moisture source placed on the upper room (scenario III) are not listed because negative values for the upward mass airflow were obtained. These values do not have physical meaning. The same problem has been reported by Miller et al. (1997). For scenario III, negative upward mass airflow

using the integral method may have been obtained because the temporal humidity ratio

curves for both rooms are very close. Thus, the HR difference at any time is very small,

which yields to large errors of the solutions to the set of Eqs. 5.3 and 5.5 or to the set of

Eqs. 5.4 and 5.5 for F_{12} and F_{21}. The air speeds in the opening were measured by five

omnidirectional anemometers, the installation of which was shown in section 4.6. The

mean air speeds across the openings were calculated from the arithmetic averages of

the data obtained from these five anemometers.

Table 5.2: Measured upward mass airflow rates and net airflow rates through the
horizontal opening, and measured average air speeds across the opening.

Cases	ΔT (°C)	Ventilation strategy	Upward net flow F_{12} (kg/s) (x10^{-3})	Net flow[1] (kg/s) (x10^{-3})	Measured average air speed $\bar{V}_{opening}$ (m/s)
1-1	+3.2	No ventilation	74.3	0.07	0.144
1-2	+2.0		61.0	0.07	0.121
1-3	-0.8		24.1	0.07	0.078
2-1	+3.5	Single	54.9	-7.28	0.145
2-2	+2.7	ventilation	53.5	-7.37	0.134
2-3	+1.6		48.2	-7.26	0.122
2-4	+0.2		26.8	-7.25	0.090
2-5	-0.7		19.8	-7.28	0.080
2-6	+2.5	Single	62.1	-11.14	0.137
2-7	-0.4	ventilation	17.7	-11.18	0.082
2-8	-1.3		9.4	-11.14	0.060
4-1	+1.5	Independent	41.7	0.09	0.126
4-2	+0.2	ventilation	20.5	0.09	0.095
4-3	-0.8	in each room	17.3	0.09	0.070
4-4	-2.7		6.9	0.09	0.054

[1] Negative values indicate downward net flows through the opening.

Figure 5.5 plots the measured upward mass airflows (F_{12}) against ΔT. The solid

line represents the linear least square fitting to all measured F_{12}. The large residual

(R^2=0.89) signifies that there is a very strong correlation between F_{12} and ΔT, and 89%

of the upward mass airflow rates are caused by the temperature differences between the

lower and the upper rooms. Higher upward mass airflows occurred when the upper room

was much colder, while much smaller upward mass airflows were found when ΔT was

near 0°C. However, there were still air movements through the horizontal openings even

when the upper room was (on average) warmer. These results show that a colder upper room facilitates upward movements of warm air and downward movements of cold air. The interzonal air movements result in larger moisture exchange between the two rooms, as presented in section 5.2.2.
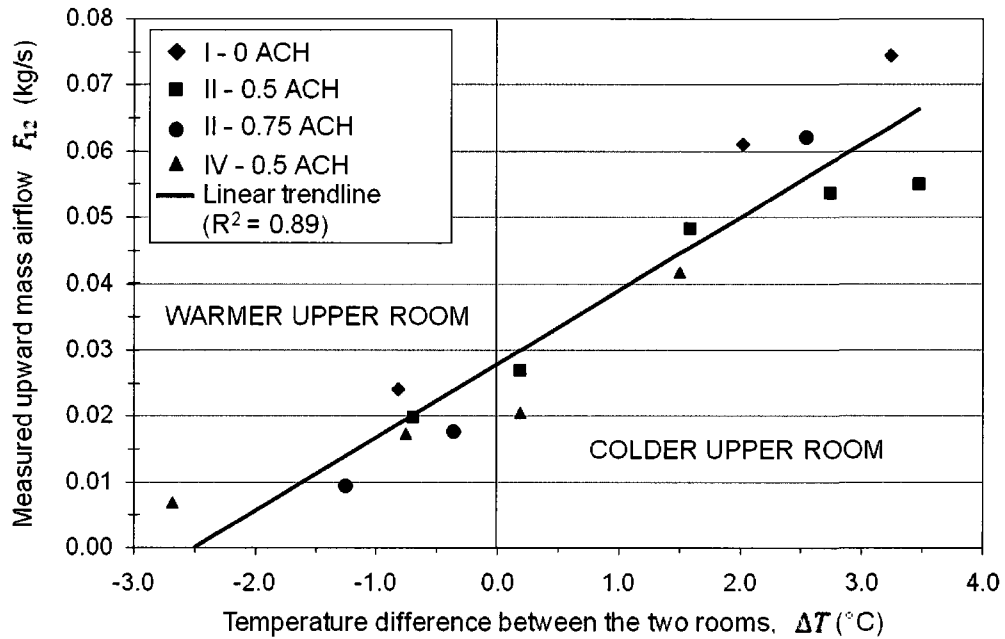
Figure 5.5: Measured upward mass airflow versus the temperature difference between the lower and the upper rooms (ΔT).

The measured average air speed through the opening ($\bar{V}_{opening}$) correlates very well with ΔT as shown in Figure 5.6. Higher values of $\bar{V}_{opening}$ are observed when the upper room is colder, whereas lower values of $\bar{V}_{opening}$ are found when the upper room is warmer. This is similar to the correlation found between F_{12} and ΔT.

Measured airflow rates and air speeds across the opening represent the same phenomenon, the air movements across the horizontal opening. The measured average air speed across the opening ($\bar{V}_{opening}$) can be used to estimate the average interzonal mass airflows through the opening ($\bar{F}^e$) according to Eq. 5.7. Also, the measured

average airflows through the opening ($\bar{F}$) can be calculated from the measured upward and downward mass airflows as shown in Eq. 5.8.

$$\bar{F}^e = 0.5 A \rho \bar{V}_{opening} \tag{5.7}$$

$$\bar{F} = 0.5(F_{12} + F_{21}) \tag{5.8}$$
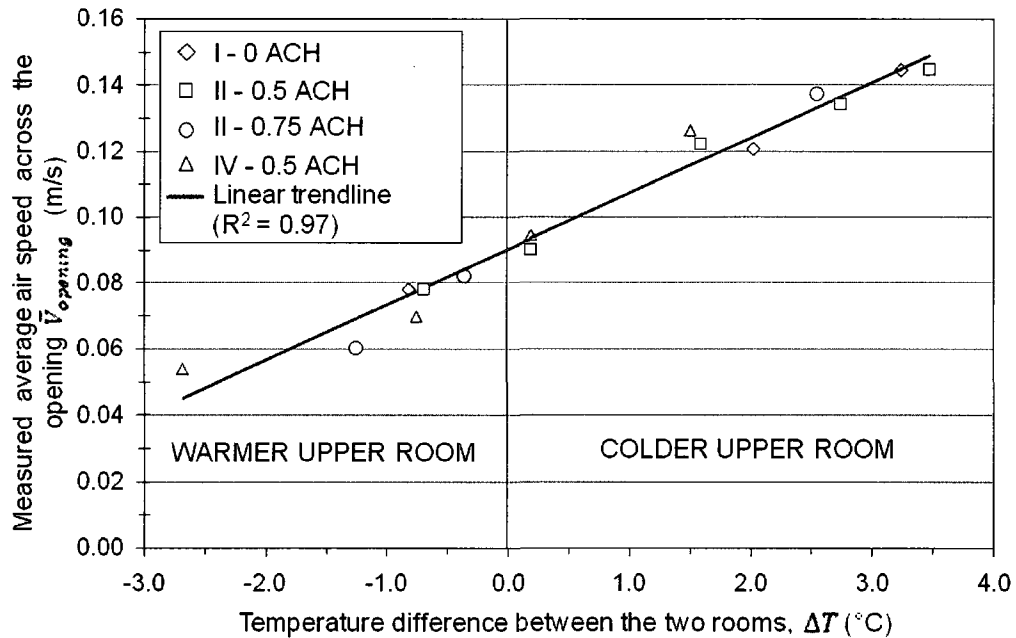
Figure 5.6: Measured average air speed across the opening versus temperature differences between the lower and the upper rooms.

Figure 5.7 plots both the measured and estimated average mass airflow rates, $\bar{F}$ and $\bar{F}^e$, respectively. It can be seen that the estimated values from average air speed across the opening ($\bar{F}^e$) are always higher than those measured in all cases tested. Nevertheless, it is noticeable that the measured and estimated average mass airflows follow the same tendency among different cases tested, which is an indication of the reliability of the measured interzonal mass airflow rates. The differences between $\bar{F}$ and $\bar{F}^e$ shown in Figure 5.7 are expected because of two main reasons:

- The estimated airflows from the measured air speeds across the opening ($\bar{F}^e$) are the actual air movement within the opening. However, due to the existence of

eddies within and close to the opening, some of the airflows did not proceed with the entire "journey" between the two rooms so that some of the air movements estimated can be considered ineffective in exchanging the water vapor between the two rooms; whereas the measured average airflows ($\bar{F}$) are based on the assumption that this airflow contributes to the water vapor exchange between the two rooms with 100% effectiveness.

- The estimated average airflow through the horizontal opening should be calculated considering the vertical component of the velocity instead of the omnidirectional air speed measured by anemometers. Since the vertical component of the velocity is always smaller than the magnitude of the velocity vector or air speed, the estimated average airflow rates through the opening are larger than the measured values.
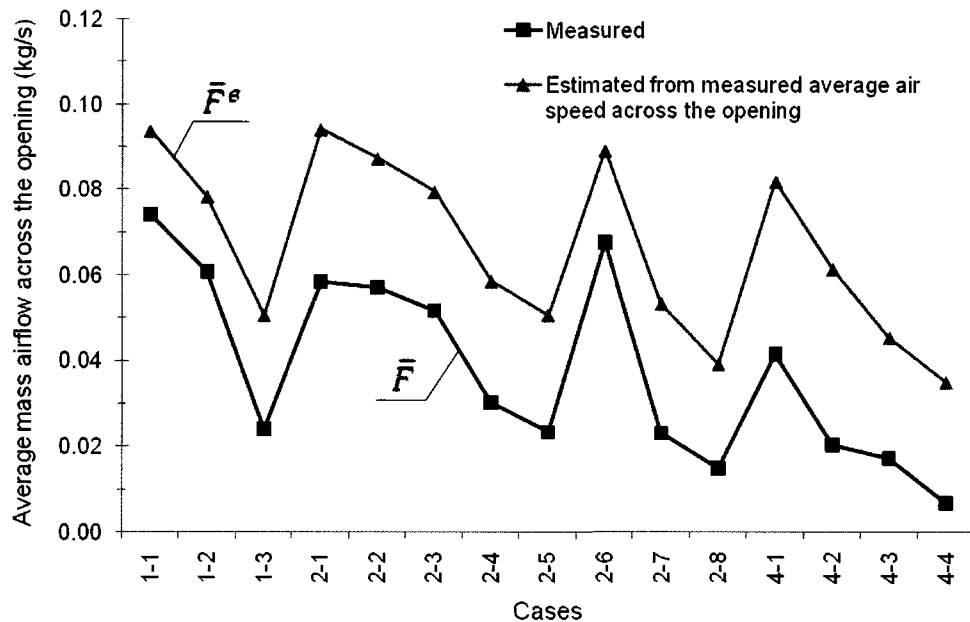
Figure 5.7: Comparison between measured and estimated (from measured air speeds across the opening) average interzonal mass airflows.

5.3.3 Interzonal mass airflows when the upper room is colder

As presented in *Chapter 2* in reviewing existing studies on interzonal airflows through horizontal openings, most studies were carried out for situations with colder upper rooms. Under this condition, the difference between air densities of the two rooms causes buoyancy driven-flows, which in turn transport warm air from the lower room to the upper room.

Figure 5.8 shows the upward mass airflow when the upper room is colder than the lower room for scenario I (no ventilation), scenario II at 0.5 ACH (single ventilation with downward net flow through the openings) and scenario IV at 0.5 ACH (independent ventilation in each room). Besides the influence of the temperature difference between the two rooms on the interzonal mass airflow, mechanical ventilation is expected to play a significant role.
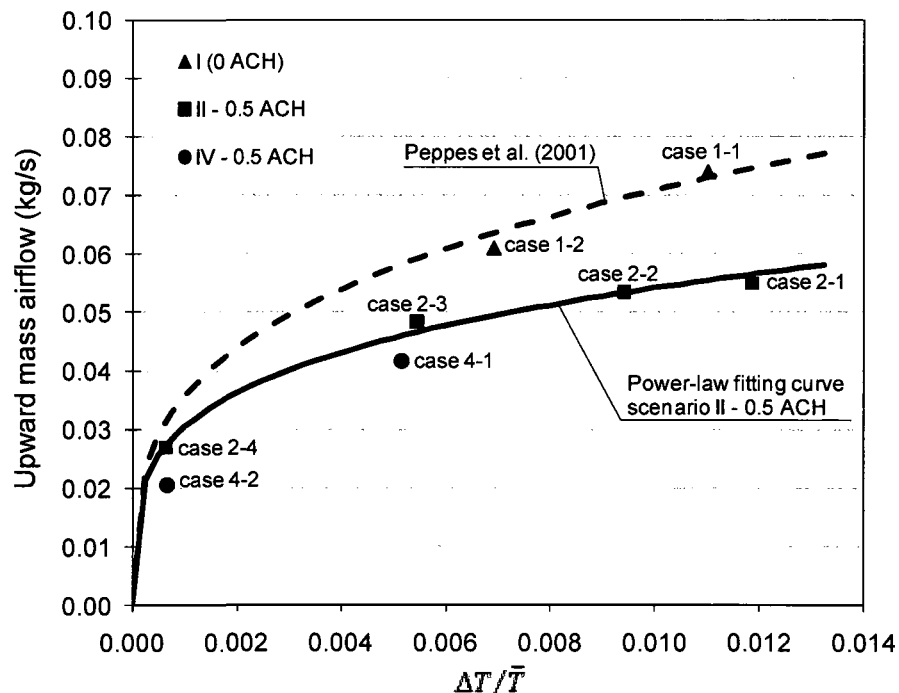
Figure 5.8: Influence of mechanical ventilation on the upward mass airflows.

First, it can be observed that higher values of F_{12} are found in cases with no mechanical ventilation than those values for cases with mechanical ventilation

(scenarios II and IV). This result reveals that mechanical ventilation restricts the interzonal mass airflows.

Second, it can be observed that upward mass airflows for the two cases tested for scenario IV are slightly lower than the values for scenario II at 0.5 ACH. However, the results based on ΔHR in Figure 5.3 show that independent ventilation (scenario IV) promotes the moisture exchange between both rooms. Since higher interzonal moisture exchange is associated with higher upward mass airflows, no definitive conclusions can be drawn about the influence of ventilation strategy on interzonal air and moisture transport for cases with mechanical ventilation. Furthermore, the available data points for scenario IV are not sufficient to support any definite conclusions.

Third, the comparison of the results for cases 1-1 and 1-2 (no ventilation and upper room colder than the lower room) with the results found in the existing studies on buoyancy-driven flows through horizontal openings and as summarized in Figure 2.14, indicates that these two cases agree very well with the flow relationship found by Peppes et al. (2001) represented by the dotted line in Figure 5.8. Although Peppes' tests a staircase, this good agreement may be due to the fact that both experiments tested similar ranges of ΔT, up to 3.5°C in the current test and up to 6°C in Peppes et al. (2001), and similar opening sizes.

Finally, Figure 5.8 also shows that the shape of the power-law fitting curve for cases of scenario II has the same shape of the curves found for buoyancy-driven flows by Peppes et al. (2001) and others. This similarity would indicate that although ventilation restricts the interzonal airflow, this phenomenon can still be represented by the generic form of the orifice flow equation as follows:

$$F_{12} = CA\rho_a\sqrt{gH}(\Delta T/\bar{T})^n \tag{5.9}$$

where F_{12} is the upward mass airflow (kg/s), C is a constant of proportionality, A is the opening area (m²), ρ_a is the air density (kg/m³), g is the acceleration due to gravity (m/s²), H is the opening thickness (m), ΔT is the temperature difference between the lower and the upper rooms (°C), $\bar{T}$ is the absolute average temperature of the two rooms (°K), and n is a fitting constant. C and n would depend on the ventilation rate and ventilation strategy.

5.3.4 Interzonal mass airflows when the upper room is warmer

Figure 5.5 indicates that upward interzonal mass airflows exist also when the upper room was warmer. Under this condition, it is not immediately clear why upward airflows occur. Only the study of Klobut and Sirén (1994) was carried out with forced ventilation, and they observed the same phenomenon. However, they did not find a reasonable explanation for this result. This section attempts to propose possible causes of this phenomenon.

The current test was designed not to impose a well mixed air condition (e.g. no fans were used to mix the air inside each room). Therefore, in the current study, the temperature distributions in either room were not uniform. While the average temperatures were warmer in the upper room and colder in the lower room, local conditions could have provided the forces to drive upward movements of air and moisture. These local conditions could have been caused by:

- Convective currents of warm air generated near and above the baseboard heater of the lower room, and

- Convective currents of warm and moist air flowing above the moisture generation system.

Although the experimental data, temperature and HR, were measured at many points across the test-hut, they are not enough to obtain a clear spatial distribution of the

temperature and HR and to identify possible warm convective currents. Moreover, air speed was measured only at 19 points, which does not make possible to establish the airflow pattern in the room. This type of information is provided by the CFD modeling in *Chapter 7*.

Another plausible cause of the measured upward mass airflows under a warmer upper room condition could be vapor diffusion through the opening. El Diasty (1993) indicates that this transport mechanism of moisture may be important in large openings in the absence of interzonal airflows through doorways. Similarly, for the situation considered here, water vapor diffusion could exist through the opening as long as there were differences in the humidity ratios in the air. Thus the measured F_{12} from the temporal HR profiles might be completely or partially the result of moisture diffusion transport through the opening. Mass vapor flow due to diffusion (m_v) through a large opening may be expressed as follows (ASHRAE, 2005):

$$m_v = D_v A \rho_a \, \Delta w / H \tag{5.10}$$

where D_v is the water vapor diffusion coefficient, which is 25 mm^2/s at 20°C, A is the opening area (m^2), ρ_a is the air density (kg/m^3), Δw is the difference in humidity ratio between the two rooms or ΔHR (kg/kg), and H is the opening thickness (m).

From the experimental data for cases with a warmer upper room, and using the average humidity ratio in each room, the calculated total moisture diffusion flow through the opening varies from 7x10^{-8} to 2x10^{-7} kg of water vapor per second, which is negligible in comparison with the amount of moisture transported by the upward mass airflows (7x10^{-5} to 5x10^{-4} kg of water vapor per second). Therefore, diffusion does not play any influencing role in the interzonal moisture transport through the horizontal opening. Hence, it may be concluded that the moisture transported upward through the

opening when the upper room was warmer was indeed caused by interzonal mass airflows.

5.4 Discussion and closing remarks

This chapter has presented the experimental results of the interzonal air and moisture exchange between the lower and the upper rooms for cases with buoyancy-driven flows (scenario I) and for cases with combined buoyancy and forced driven flows (scenarios II, III and IV). The driving forces for the flows originated are temperature differences between the two rooms and the mechanical ventilation. The literature review in *Chapter 2* shows that interzonal airflows through horizontal openings have been studied for cases with buoyancy-driven flows only. The work reported in this chapter represents pioneering research on interzonal airflow through horizontal openings under combined buoyancy and forced driven flows. This chapter provides reliable and meaningful results for this condition that may lead to a better understanding of this phenomenon. The main conclusions drawn from the experimental results are:

- The upward mass airflow and interzonal moisture exchange are related highly to the temperature difference between both rooms. A colder upper room promotes the interzonal air and moisture exchange, while a warmer upper room condition significantly restricts the interzonal air and moisture transport through the opening.

- In comparison with cases with no ventilation, mechanical ventilation strongly restricts the interzonal mass airflow through the opening. However, it was found that the flow equation representing this phenomenon can still be expressed by the generic form of the orifice flow equation that applies for cases with buoyancy-driven flows.

Due to the limited amount of experimental data, no conclusive results may be drawn about the influence of ventilation rate and ventilation strategy on the interzonal air

and moisture flows. These issues are addressed in *Chapter 7* by means of CFD simulations.

CHAPTER 6

CFD MODELING AND VALIDATION

6.1 Introduction

In this thesis research a 3D CFD model was implemented in Airpak to model zonal movements and interzonal exchanges of air and moisture between the upper and the lower rooms interconnected by a large horizontal opening. This chapter covers the modeling of the two-story test-hut, the implementation of the components of the numerical solution methods in Airpak, and the validation of the CFD model. The CFD simulation results are presented in *Chapter 7*.

Airpak (version 3.012) is a CFD software capable of modeling airflow, heat transfer, contaminant transport, and thermal comfort in ventilated rooms. Airpak uses FLUENT (version 6.3.26) as solver engine for the transport equations and has already implemented the indoor zero-equation model to model turbulence that was introduced in *Chapter 3*.

The indoor zero-equation model was chosen in this investigation because:

- It has been extensively validated (see section 3.3) and provides good predictions of indoor airflow pattern and the distribution of temperature and species, especially for mixed convection; and

- The computing time is much shorter than other turbulence models, which allows performing a large number of simulations to extend the conditions tested experimentally in a reasonable period of time.

The CFD model includes several aspects that should be carefully implemented or chosen in the CFD software to represent the real physical phenomena that needed to be simulated. The CFD model includes, for example, building the room, modeling the heat

and moisture sources, selecting the turbulence model, building the mesh grid, choosing the convergence criterion, etc. All these aspects and others acting together significantly impact the ability of the CFD model to properly simulate the actual physical phenomena. To ensure the reliability of the results, the CFD model must be validated. Validation is defined by Chen and Srebric (2001) as:

"The demonstration of the coupled ability of the user and the CFD code to accurately predict representative indoor environmental applications for which some sort of reliable data is available".

Hence, to arrive at reliable results, not only the CFD model should be validated, but also the ability of the user to model the physical problem of interest. Reliable experimental data should be available to perform the validation. The validation of the CFD model focuses on:

- Confirming that the turbulence model, the indoor zero-equation model employed in this thesis, is capable of predicting the transport of heat and moisture through the horizontal opening caused by interzonal airflows;

- Confirming that the physical components of the problem (e.g. two-story test-hut, moisture generation system, baseboard heaters, inlets) are properly modelled; and

- Confirming that the discretization method, mesh topology and size, and the numerical algorithm are properly chosen for the airflow problem of the room being investigated.

The experimental data provides not only the information about the interzonal air and distribution of temperature and moisture across the two-story test-hut, but also the data to perform a detailed validation of the CFD model. In most studies, very few experimental cases are used to validate the CFD model. In this thesis research, extensive experimental data are used to validate the developed CFD model. The

experimental data cover 12 test cases that correspond to scenarios II (single ventilation with downward through the opening) and IV (independent ventilation in each room). No validation was performed for scenario I (no ventilation) because there is no experimental data at steady-state conditions for this scenario (test was stopped after 3 hours of moisture generation to avoid surface condensation and damage of RH sensors). Also, scenario III was not validated because no interzonal mass airflows were calculated in this case.

The CFD modeling of the physical problem and its validation, presented in the next sections, follows the guidelines of Chen and Srebric (2001), Sørensen and Nielsen (2003), Zhou (2007) and Fluent (2007).

6.2 Modeling the two-story test-hut in Airpak

This section shows how the physical components of the two-story test-hut were modeled in Airpak. Figure 6.1 shows a sketch of the two-story test-hut built in Airpak for scenario II. The walls are of zero-thickness. While most of existing simulation studies used average wall surface temperatures, this research used all wall surface temperatures measured in the experiment as input to reflect more realistic boundary conditions. The platform containing the horizontal opening and dividing the upper and lower rooms is 0.22 m thick and surface temperatures on the upper and lower sides of the platform are specified. No moisture interaction between the indoor air and wall surfaces was considered.

The moisture source system was complex to model because water dripped into the steel pot above the hotplate and evaporated immediately when it hit the hot steel pot, as shown in Figure 6.2a. A small chrome wire shelf with an aluminum sheet on top was used to support the hotplate and the steel pot. The measured power consumption of the hotplate was 150 W, which corresponds to approximately 65 W for latent heat involved

in the evaporation process of the dripping water and to 85 W for the sensible heat. This last value is implemented as the total power of the hotplate in Airpak. Figure 2b shows the modeled moisture generation in Airpak. The top cylindrical plate of the hotplate was modeled as a heat source. The steel pot was modeled as a block with a small fan that represents the hole through which vapor leaves the pot. The fan generated a constant mass rate of water steam at 100°C. The aluminum sheet on the top of this shelf was modeled with dimensions of 0.38 m x 0.71 m.
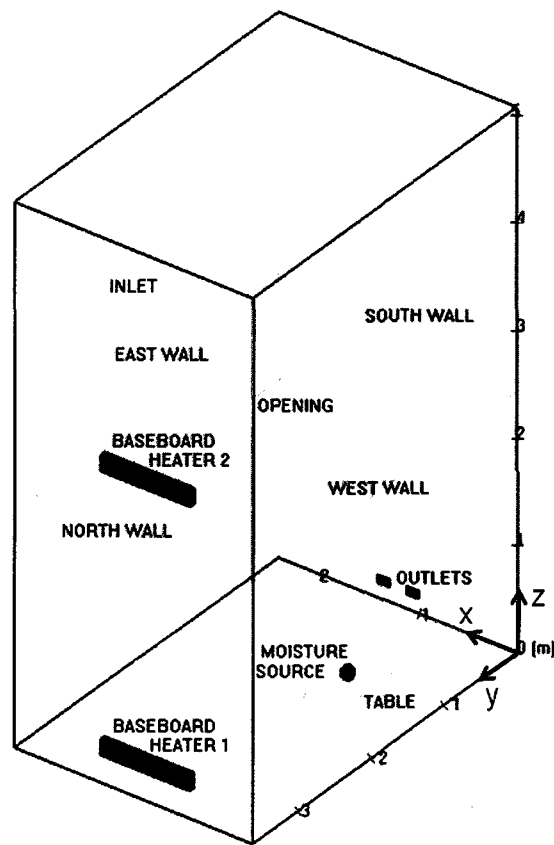
Figure 6.1: Two-story test-hut model built in Airpak for scenario II.

Baseboard heaters were modeled as heat sources of 0.92 m x 0.065 m x 0.15 m. The measured mean power consumption during the moisture generation period was set as total power for each baseboard heater. However, heating power measurements of these heaters showed that the baseboard heaters operated as plotted in Figure 6.3a. Heaters delivered heat over few second, increasing the heating power from zero to

reach their maximum heating power (> 800 W) and then returned to zero. Instead, the CFD model considers the average power heating output of baseboard heaters during the moisture generation period, which is below 400 W depending on the case.
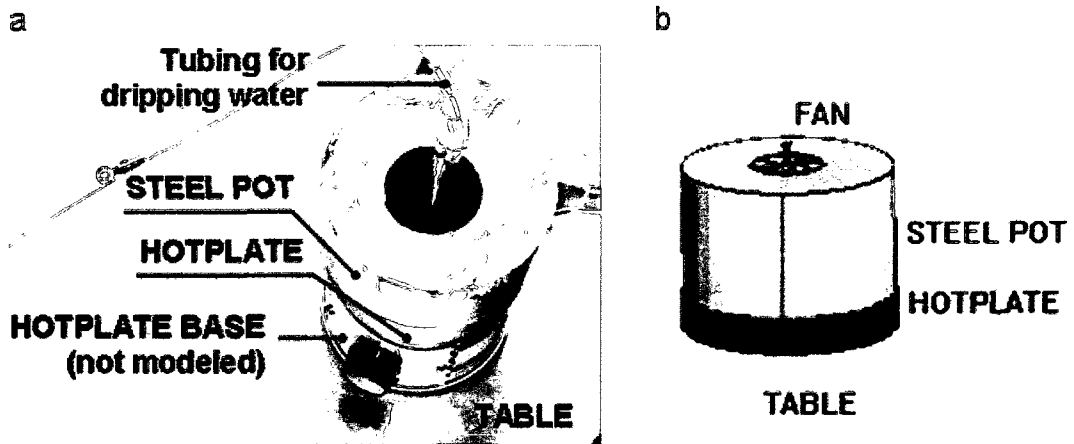
Figure 6.2: a) Real and b) modeled moisture source system.
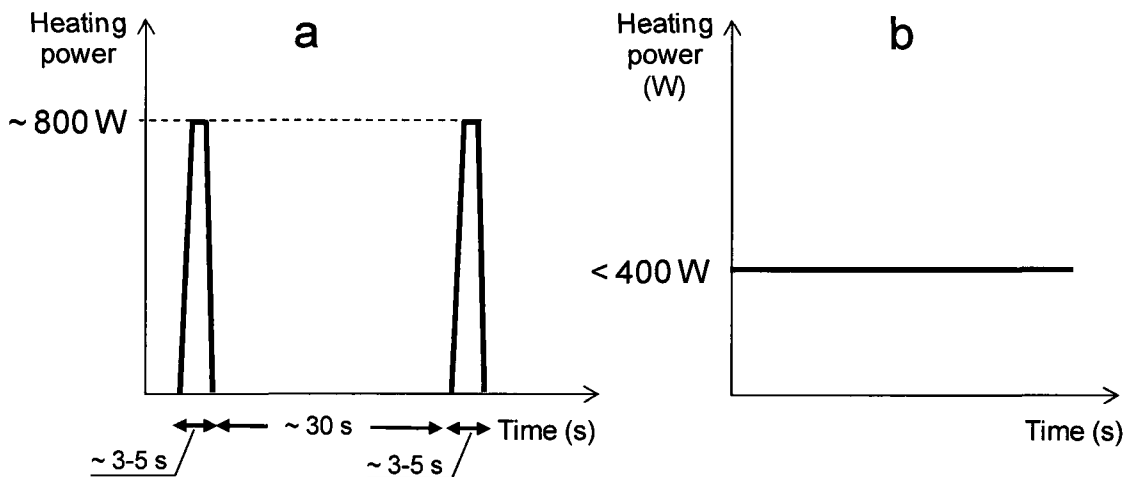
Figure 6.3: Operation of baseboard heaters: a) measured and b) modeled.

The ventilation inlet face was a small rectangular section of 96.5 mm (W) by 21.8 mm (H). Because the circular cross-section of the supply air pipe changed to a small rectangular section at the inlet face in a short length (see Figure 4.10), the inflow may spread in all directions. To account for this divergence, the inlet was modeled as 9 small rectangular diffusers with equal areas in a 3 by 3 arrangement; their airflow rates were the same; the inflow directions were different, however, as shown in Figure 6.4. Angle α

was ±25° or 0° (for the east and west deflections), whereas β was ±15° or 0° (for the up and down deflections).
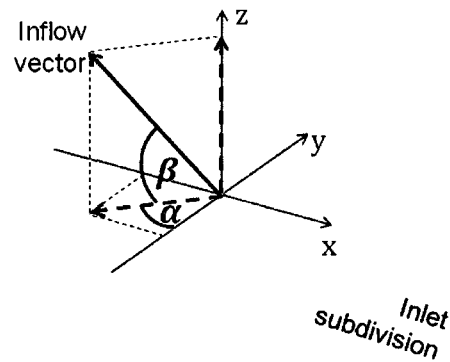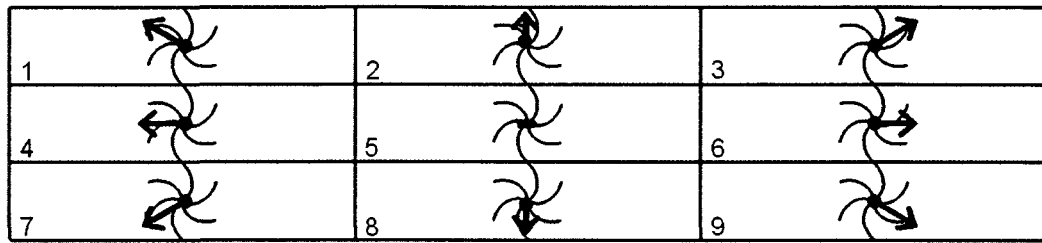
	X	y	z
1	-0.4663	-1	0.2679
2	0	-1	0.2679
3	0.4663	-1	0.2679
4	-0.4663	-1	0
5	0	-1	0
6	0.4663	-1	0
7	-0.4663	-1	-0.2679
8	0	-1	-0.2679
9	0.4663	-1	-0.2679

Figure 6.4: Frontal view of the modeled inlet. Arrows and table show the direction of the inflow in each subdivision.

Since the air was pumped out the room before it passed through the AHU units (see Figure 4.8), the outlets were implemented as openings and the normal outflow was specified by means of the air speed.

6.3 Components of the numerical solution methods and its implementation in Airpak

6.3.1 Mathematical model and discretization scheme

The starting point of the numerical method is the mathematical model, which corresponds to the set of partial differential governing-equations (given in Chapter 3) that represent the physical phenomena. Besides the governing equations of mass, momentum and energy presented in Chapter 3, the following aspects were considered:

- The discrete ordinates radiation model was used to account the determination of

the surface temperature of the baseboard heaters and hotplate because the heat flux boundary condition was set for these components.

- The species transport equation was considered in the governing equations to determine the humidity ratio distribution in the two-story test-hut. The diffusion coefficient of the water vapor was set equal to 2.5×10^{-5} m^2/s, which corresponds to the diffusion coefficient of water vapor at 20°C.

- In order to achieve faster convergence, Boussinesq approximation for buoyancy flows described in *Chapter 3* was used.

Steady-state and 3D simulations were performed to predict the air velocity field and distribution of temperature and humidity ratio within the two-story test-hut, and to calculate the interzonal mass airflows through the opening.

The variables involved in the governing equations (pressure, velocity components, temperature, humidity ratio) are computed at the grid-points. Then, the partial differential equations are approximated by a system of algebraic equations for the variables at discrete locations in space. Most common discretization methods used in CFD are finite-difference, finite-volume, and finite-element methods. Airpak uses the finite-volume method, in which the solution domain is subdivided into a finite number of contiguous control volumes, and the variables (e.g. pressure, velocity components, temperature and species concentration) are estimated at the center of each control volume.

The approximation of the terms in the governing equations is made by so-called differencing schemes. The upwind differencing scheme (UDS) is available in Airpak. Upwind means that the value of the convection term at the control volume face is derived from quantities in the control volume upstream (Veersteg and Malalasekera, 1995). Airpak allows the choice between the first-order and second-order UDS. In the first-order UDS, the value of the variable at the face of the control volume is set equal to the value at the center of the control volume. In the second-order UDS, higher order

accuracy is achieved at cell faces through a second-order Taylor series expansion around the center of the control volume. In this research the second-order UDS was used to achieve a higher accuracy of the solutions.

6.3.2 Mesh topology and size

The hexahedral mesh was used. Several mesh sizes were tested; trial runs indicated that a mesh with about 356,000 nodes for scenario II and 389,000 nodes for scenario IV provides satisfactory results. The mesh size for scenario IV is larger because the inlet in the lower room and the outlets in the upper room are included. The mesh was generated by specifying the maximum spacing of 0.18 m in the y-direction, and 0.12 m in the x and z directions, and by specifying the closest node to the wall surfaces at 0.025 m. Meshes were refined locally near the wall surfaces, baseboard heaters, inlets, outlets and the moisture generation system. Figure 6.5 shows the mesh grid for scenario II in the longitudinal and transversal planes of the test-hut.

6.3.3 Solution algorithm, convergence criteria and relaxation factors

In the set of governing equations shown in *Chapter 3*, the values of the velocity components, temperature and species concentration (humidity ratio) can be determined solving the conservation equations. For determining pressure. Airpak uses the SIMPLE (Semi-Implicit-Method for Pressure-Linked-Equations) pressure-velocity coupling algorithm (Patankar, 1980). SIMPLE algorithm uses a relationship between velocity and pressure corrections to enforce mass conservation and to obtain the pressure field.

The solution procedure is iterative, and the unbalance of the solved variables or residuals occurs at the end of each iteration. A criterion has to be established to allow convergence of the CFD solution (termination of the iterative process). In this study, convergence is considered to be achieved for a solution when the sum of the scaled residual was below 10^{-6} for energy and 10^{-3} for other variables. In order to obtain stable

and converged results, the iteration procedure uses under-relaxation factors for the different variables solved. Following the guidelines in Zhou (2007), the under-relaxation factors were selected as 0.3 for pressure, 0.2 for momentum, and 1.0 for temperature, viscosity and water vapor.
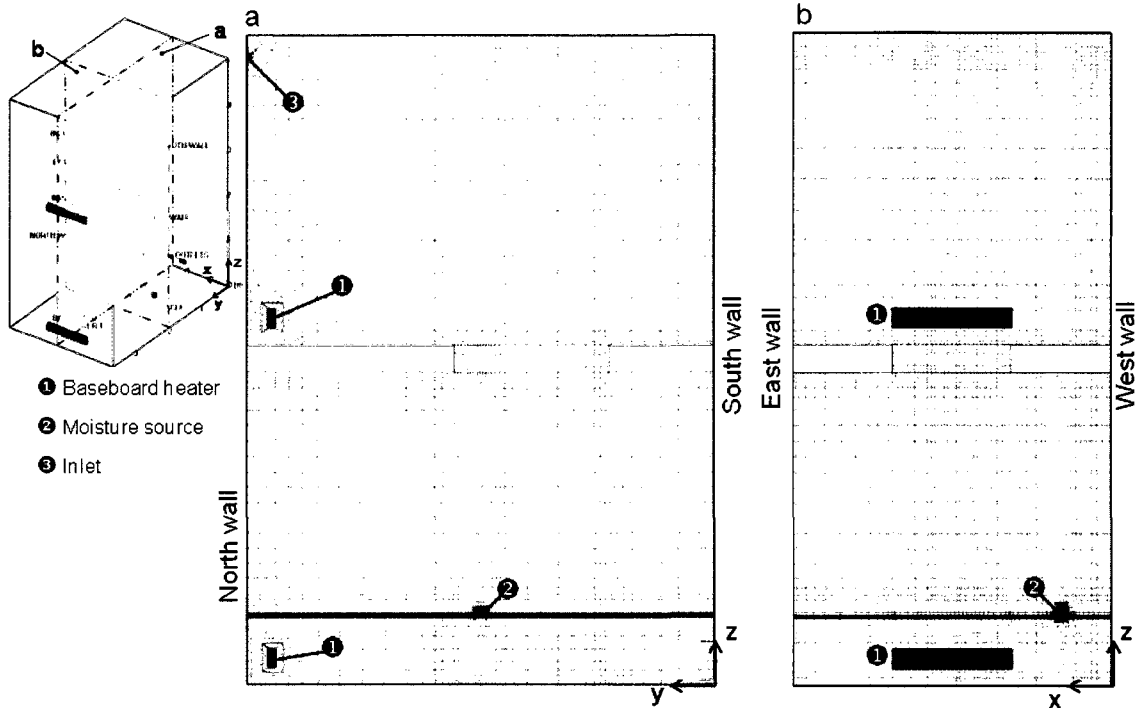
Figure 6.5: Mesh grid for scenario II at a) x = 1.22 m and at b) y = 1.81 m.

All simulations were performed on the Concordia University HPC (High-Performance Computing) cluster using two of its 712 processors (each a 2.2 GHz AMD Opteron 64-bit) in parallel. For most cases, convergence was reached between 2 and 4 hours.

6.4 Validation of the CFD model

The CFD model is validated in two steps for scenario II at 0.5 and 0.75 ACH (single ventilation with downward net flow through the opening) and scenario IV at 0.5 ACH (independent ventilation in each room) at different values of ΔT. Appendix C

summarizes the test conditions of these cases that were used as input data for the CFD simulations.

In the first step, the CFD model is validated with the air speed and temperature data measured by 19 omnidirectional anemometers across the test-hut and into the opening, and with the experimental data for air temperature and HR obtained from 64 RH probes. In the second step, the interzonal mass airflows through the opening calculated from the CFD simulations are compared with those derived from measurements in *Chapter 5*. Herein, the result obtained from the CFD simulations are called predicted, simulated or computed.

6.4.1 Validation for air speed and distribution of temperature and HR

Figures 6.6, 6.7 and 6.8 show the comparisons between the computed and measured values of air speed and temperature profiles at two locations of the test hut (poles A1 and A2) for scenarios II at 0.5 ACH and 0.75 ACH, and for scenario IV at 0.5 ACH, respectively.

Pole A1 was located in the middle of the opening with sensors above, at and below the opening. Simulated air speeds agree quite well with the measured air speeds in both scenarios. Only cases 2-8 and 4-2 show less agreement because CFD air speeds within the opening and above the opening are much higher than the measured values. Despite these few discrepancies, the overall performance of the CFD model to predict the air speeds above, within and below the opening (pole A1) is good, which is essential to properly model the interzonal air and moisture transport through the horizontal opening.

Pole A2 was located between the opening and the baseboard heater. The CFD profiles show a discontinuity that represents the platform between z = 2.43 m and z = 2.65 m. Pole A2 includes few points in the occupant's zone (core of the room), where air
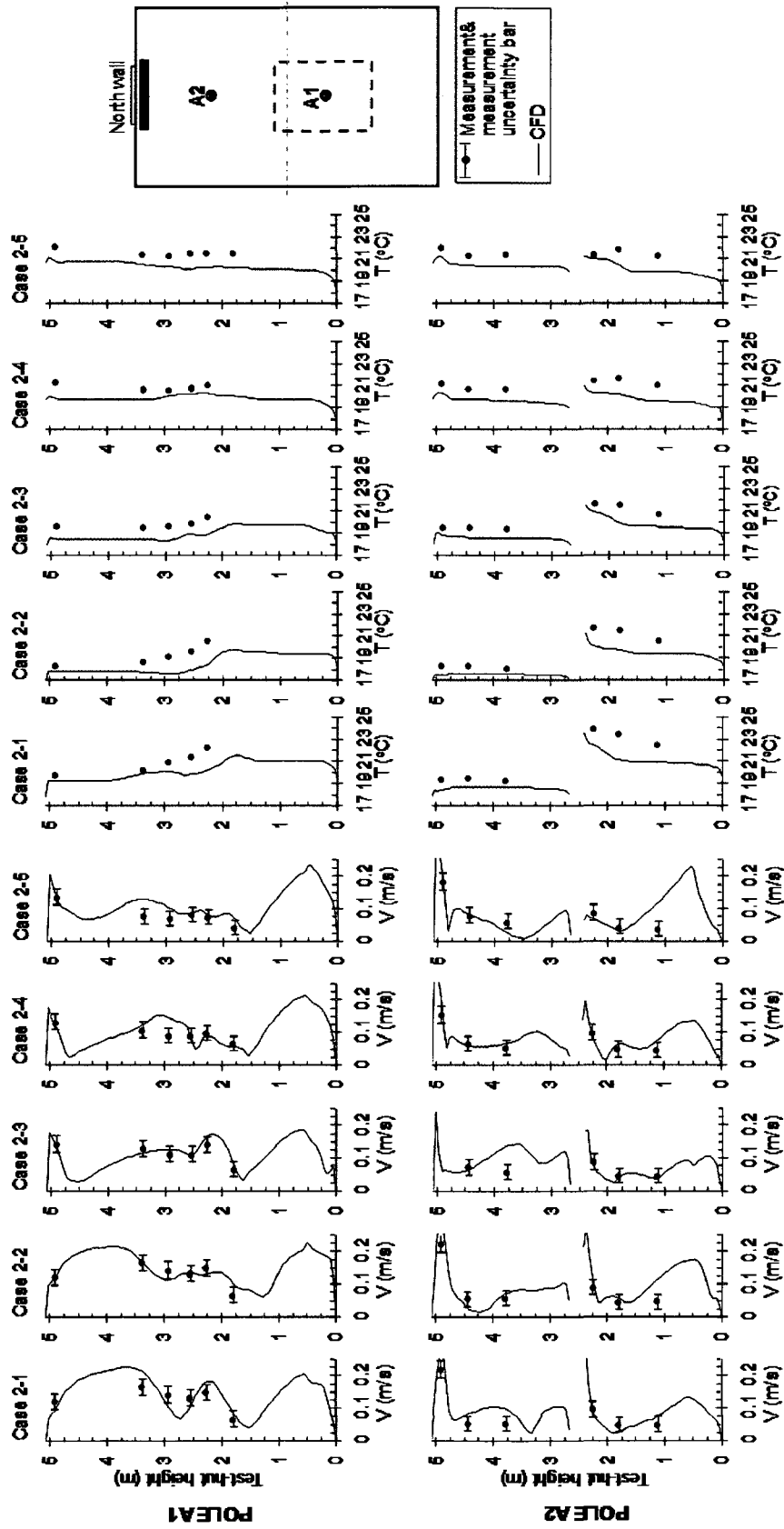
Figure 6.6: Comparison of measured and simulated air speeds and temperatures for scenario II at 0.5 ACH (cases 2-1, 2-2, 2-3, 2-4 and 2-5).
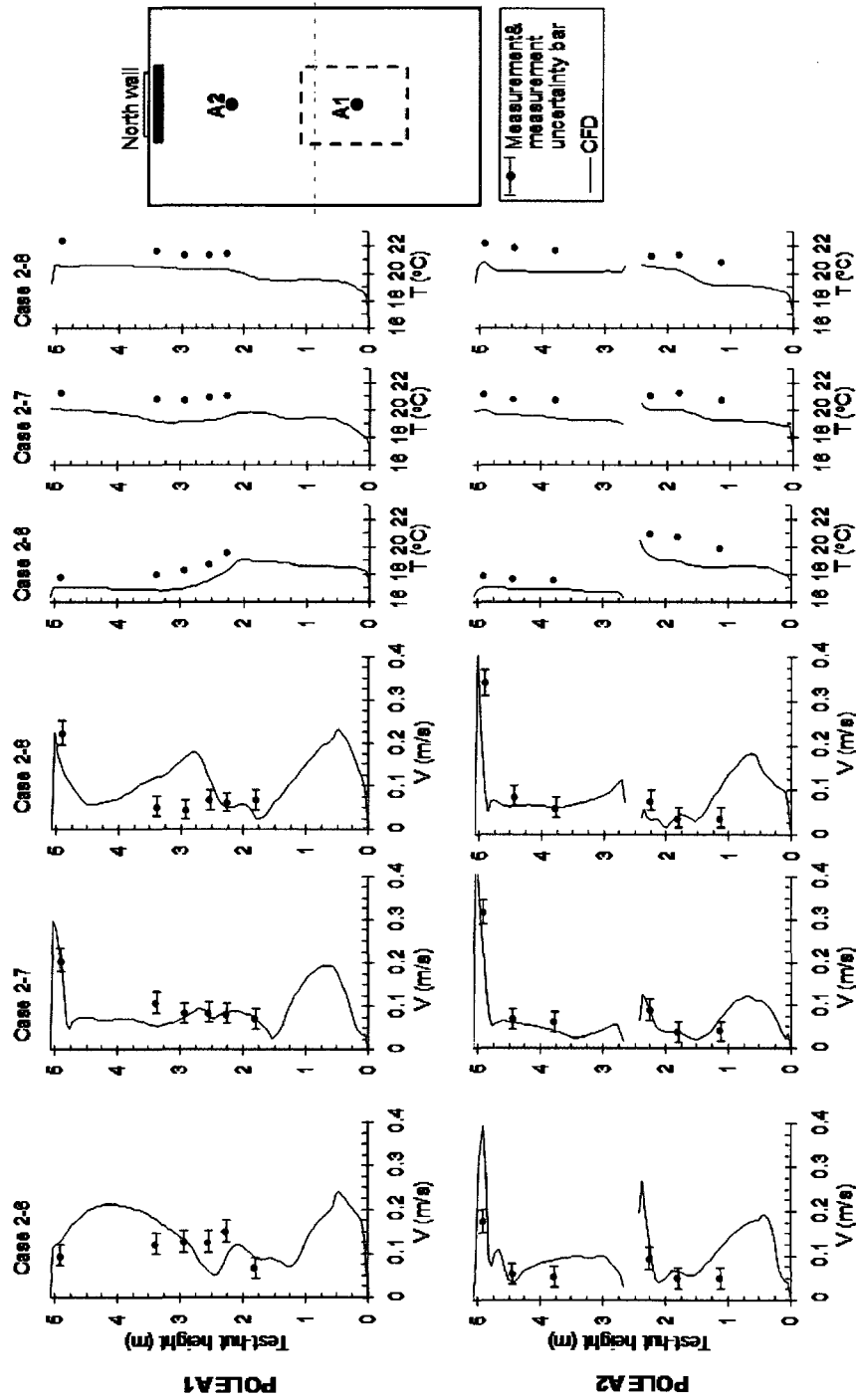
Figure 6.7: Comparison of measured and simulated air speeds and temperatures for scenario II at 0.75 ACH (cases 2-6, 2-7 and 2-8).
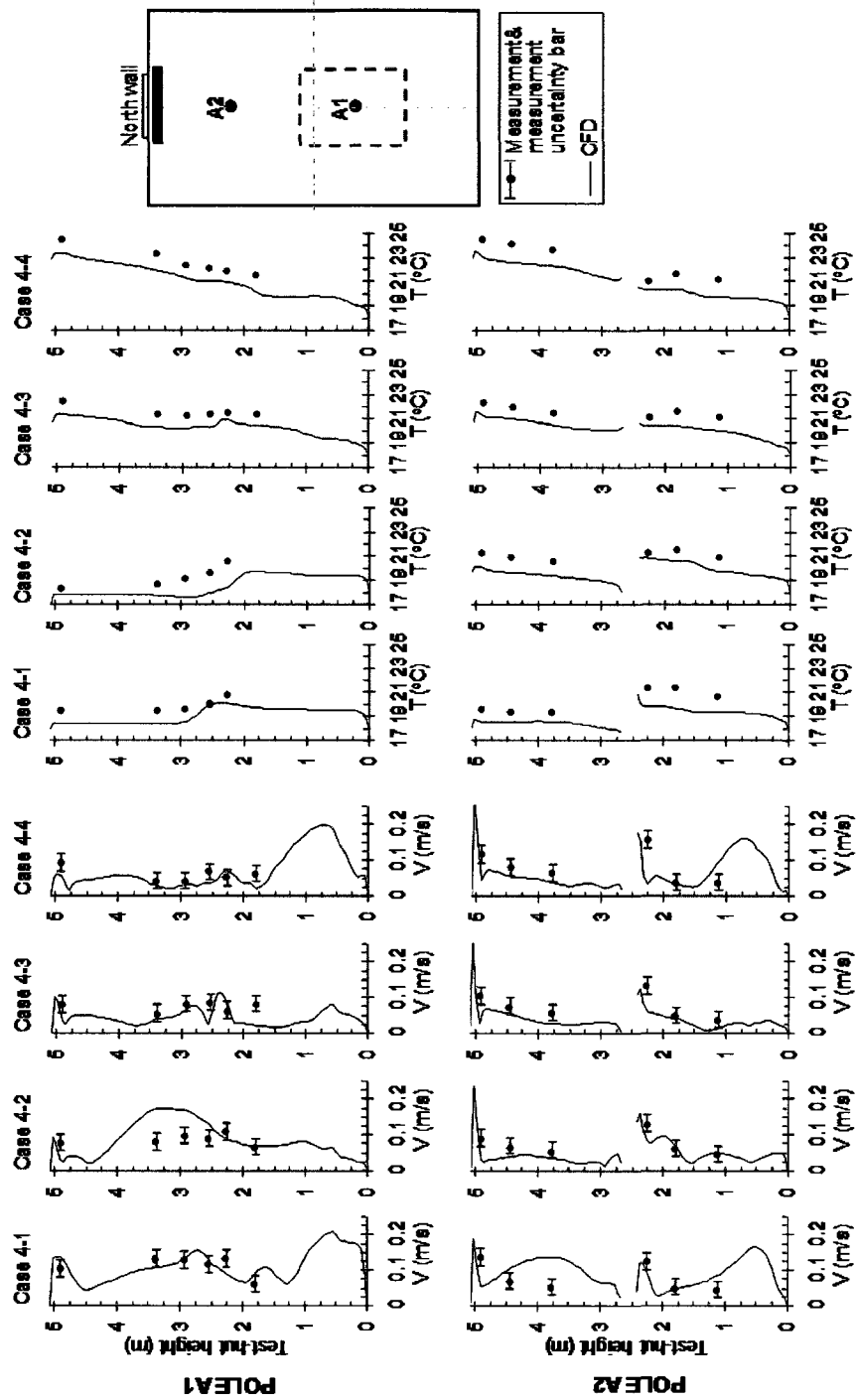
Figure 6.8: Comparison of measured and simulated air speeds and temperatures for scenario IV at 0.5 ACH (cases 4-1, 4-2, 4-3 and 4-4).

speeds are below 0.1 m/s. In this zone, some discrepancies between the computed and measured values are observed. Air speeds in the jet throw from the ventilation inlet vary among scenarios and ventilation rates. Higher air speeds (> 0.3 m/s) can be observed in the jet throw for scenario II at 0.75 ACH in the upper room, while lower air speeds (< 0.15 m/s) are found for scenario IV at 0.5 ACH in jet throw in both rooms. The predicted air speeds are close to those measured in the jet throw zone. Only case 2-8 shows an unacceptable difference. Results in the jet throw show that the inlet was properly modeled, which is key to obtain good CFD predictions in the two-story test.

Comparison between the measured and simulated temperatures in poles A1 and A2 shows that CFD model under-predicts the air temperatures. The simulated temperatures are between 0.5°C and 2°C lower than t he measured temperatures, but also it can be observed the good agreement between the tendency of the predicted and measured temperatures. The discrepancies in temperature shown may be caused by the complex boundary conditions. Wall surface temperatures were measured at several locations along the walls but there are large zones without measurements. To obtain the wall temperature distribution in these zones, the CFD software interpolates between the measured temperatures, which may introduce errors. Other complex boundary conditions are the baseboard heaters. While the heating power of the baseboard heaters had a transient behavior as shown in Figure 6.3a, the CFD model considers the average heating power of these heaters (Figure 6.3b). Later in this section, the simulated temperatures are compared with the values measured by means of RH sensors. The results show that the predicted temperatures are lower than the simulated values, but in most locations the differences in temperature are slightly lower (< 0.7°C) than those found for measurements with omnidirectional anemometers.

Figures 6.9 to 6.14 show the comparison between the measured and computed distributions of HR and temperature for cases 2-3 and 2-5 (scenario II at 0.5 ACH),

cases 2-6 and 2-7 (scenario II at 0.75 ACH), and cases 4-1 and 4-3 (scenario IV at 0.5 ACH). Comparisons are made in seven locations (RHT1, RHT2, ... RHT7), where temperature and HR were obtained from measurement data from the 2% RH sensors.

In most of the locations and cases, very good agreements between simulated and measured HR and temperature are observed. It can be seen that the CFD model provides noticeable predictions of HR in most locations, except in the upper room of cases 2-5 and 2-6. In these two cases, the predicted HRs are about 0.5 g/kg lower than the measured values; however, this difference corresponds to a relative difference of about 6.5% only. Since the HR in the upper room depends mainly on the upward mass airflow, the good predictions of HR in the upper room indicate that the CFD model is properly modeling the upward air and vapor flow through the opening.

Moreover, good predictions of HR in the lower and upper rooms show that the moisture distribution across the rooms is also being predicted properly by the CFD model. An interesting location to be analyzed separately is RHT4 because is close to the moisture generation source. In this location, the measured and simulated HR in the lower room agree well in all cases, which shows that the rising and distribution of water vapor from the moisture source is well predicted by the CFD model.

Comparing the computed and measured temperatures, it can be observed that the CFD model predicts well the temperature profiles. However, the CFD model systematically under-predicts the temperatures in many points by 0.5°C - 0.7°C. This range of differences between predicted and measured temperatures is considered to be between excellent and acceptable by some studies on validating CFD models (Srebric et al., 1999; Xu and Chen, 2000; Zhang et al., 2007). These differences could be caused by the complex boundary conditions (e.g. wall surface temperatures, baseboard heater operation), and by uncertainty in estimating the convective heat transfer.
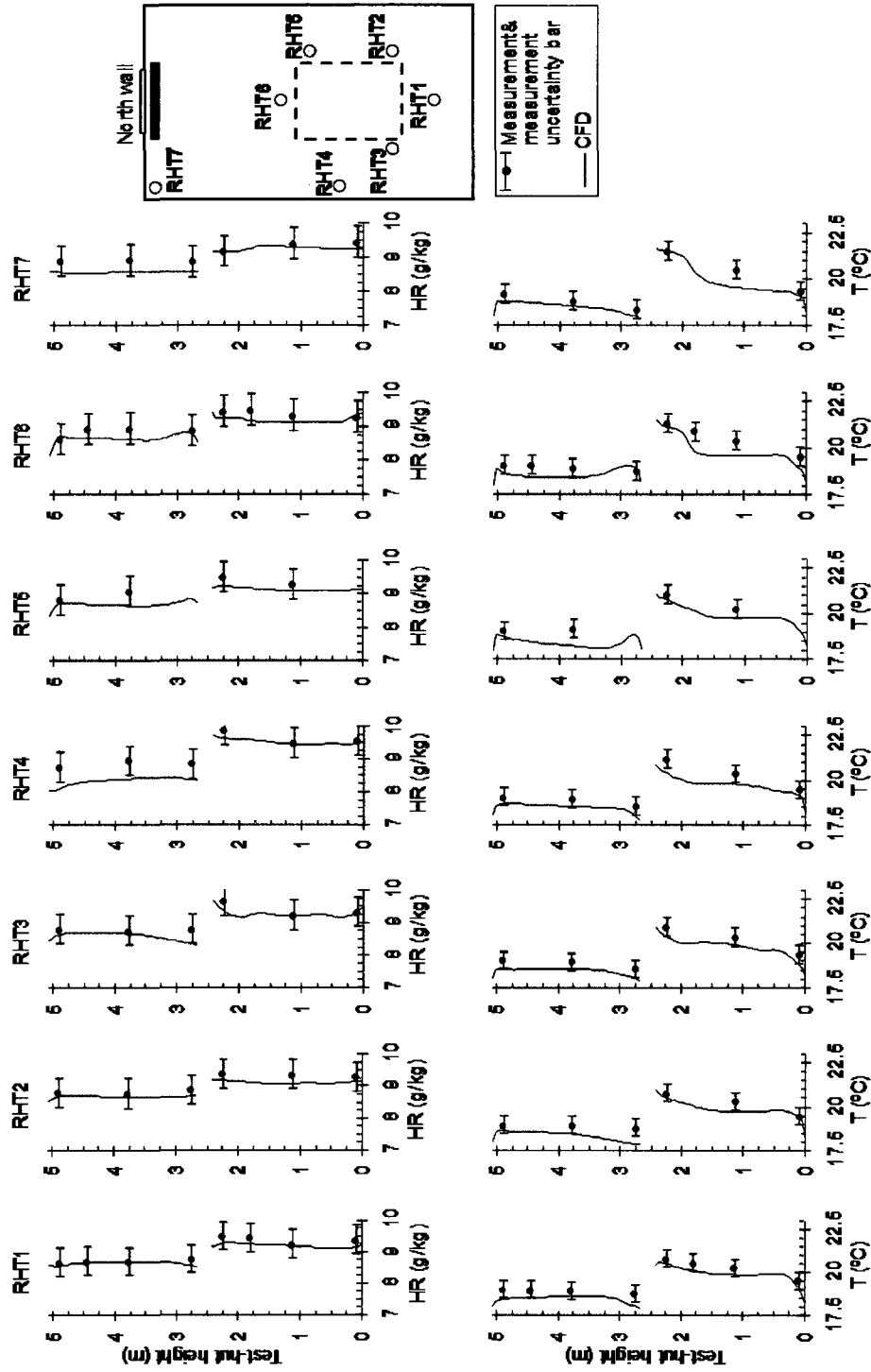
Figure 6.9: Comparison of measured and simulated distributions of humidity ratio and temperature for case 2-3 (scenario II at 0.5 ACH).
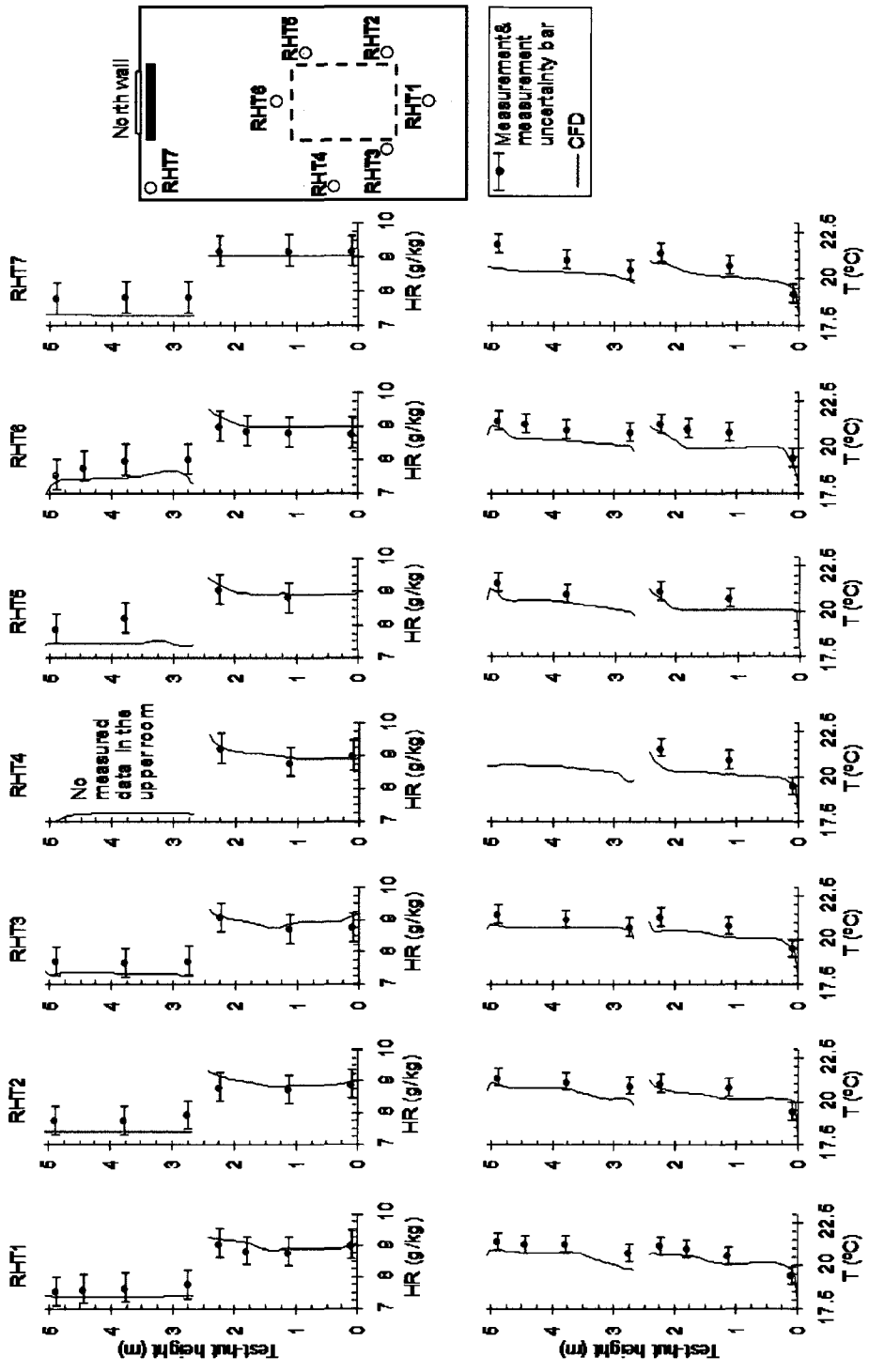
Figure 6.10: Comparison of measured and simulated distributions of humidity ratio and temperature for case 2-5 (scenario II at 0.5 ACH).

123
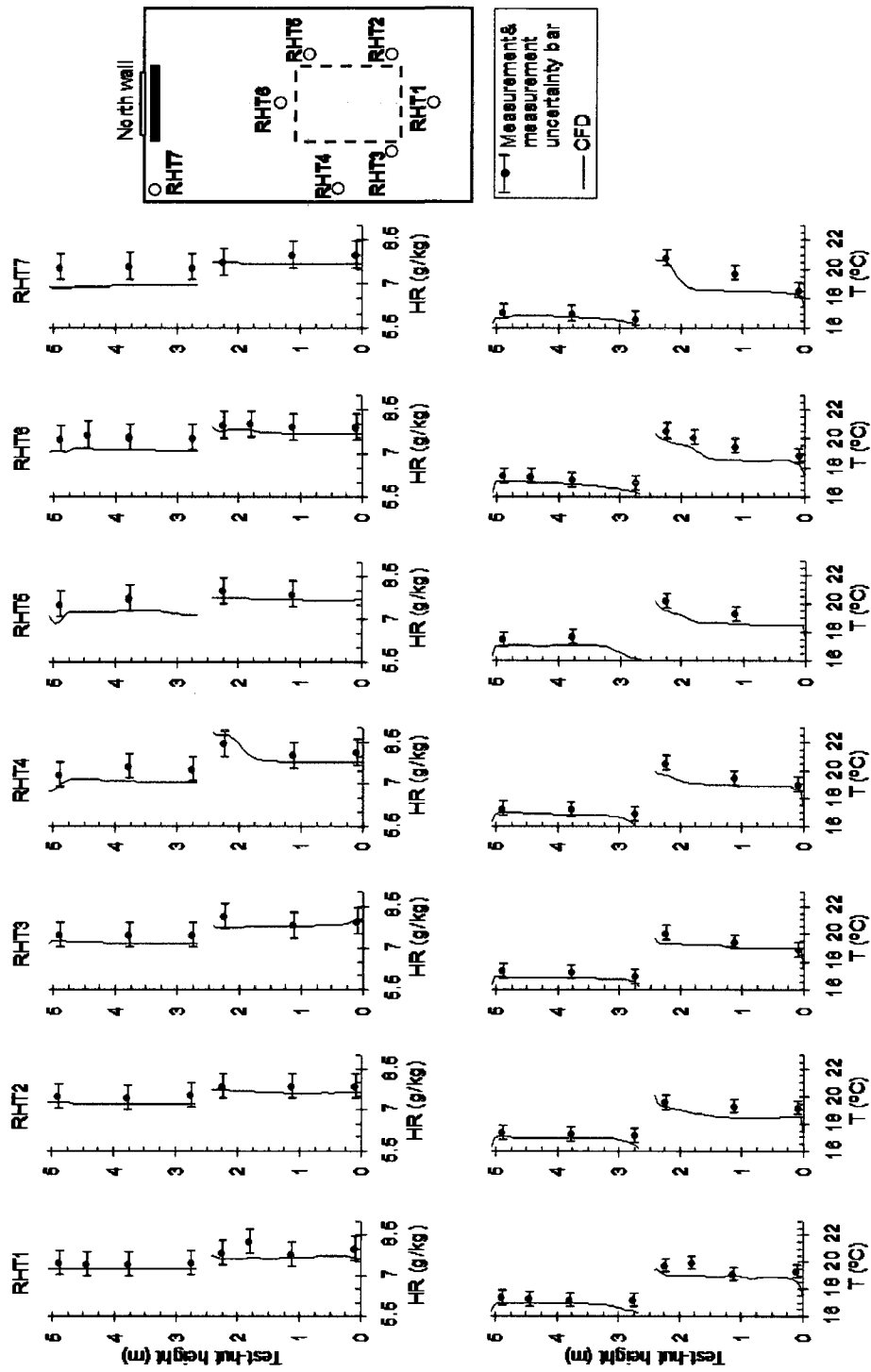
Figure 6.11: Comparison of measured and simulated distributions of humidity ratio and temperature for case 2-6 (scenario II at 0.75 ACH).
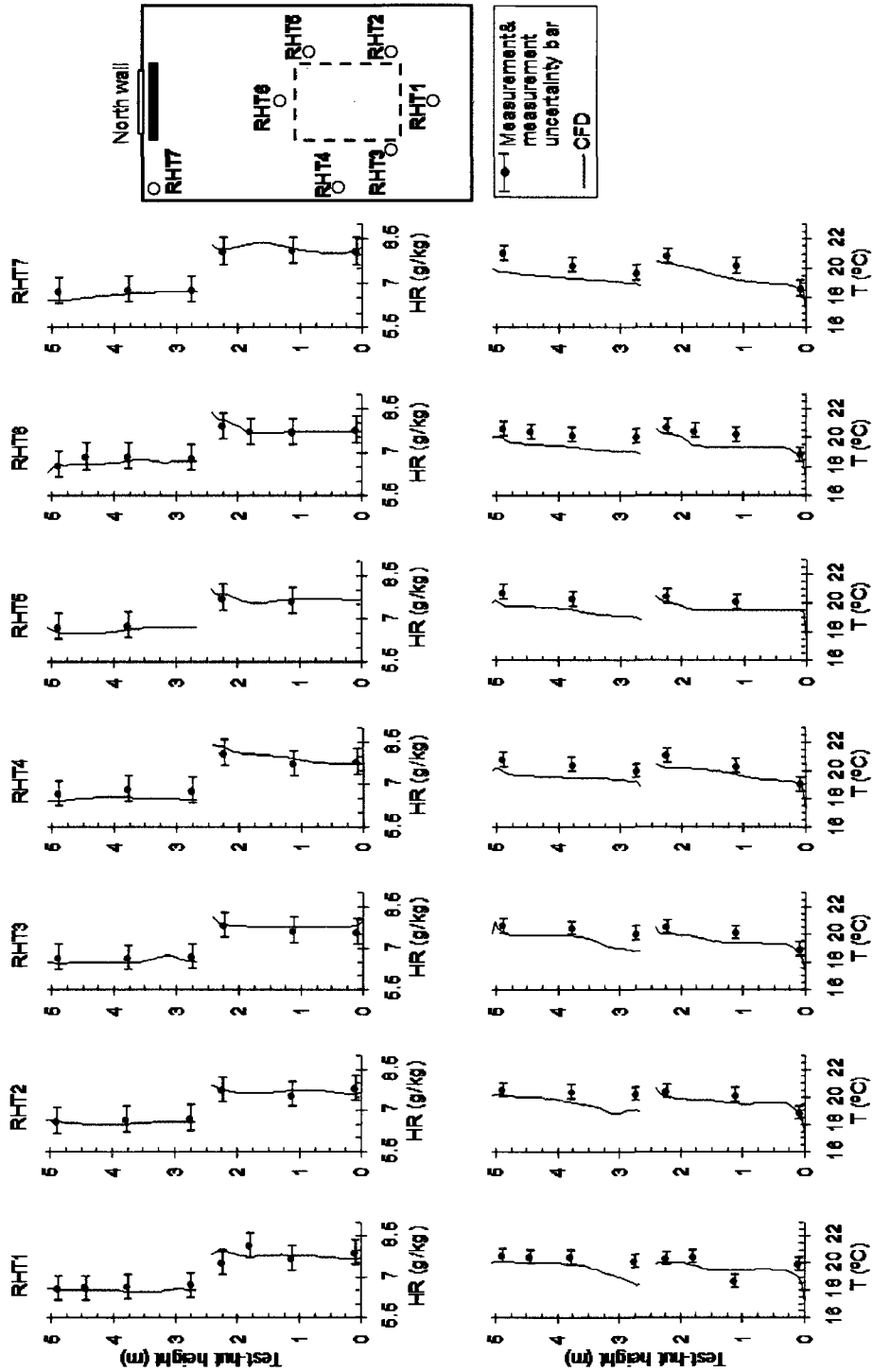
Figure 6.12: Comparison of measured and simulated distributions of humidity ratio and temperature for case 2-7 (scenario II at 0.75 ACH).
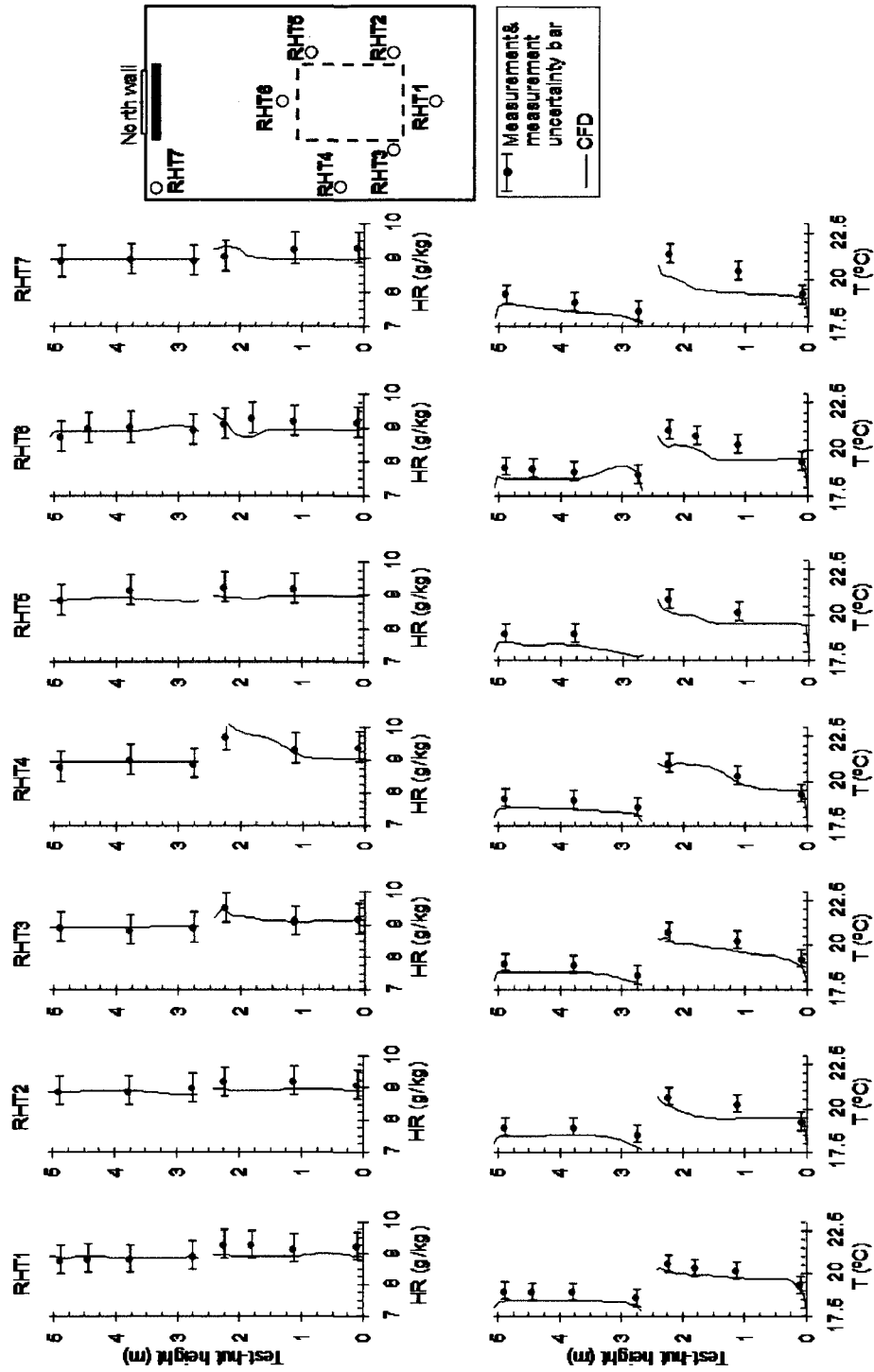
Figure 6.13: Comparison of measured and simulated distributions of humidity ratio and temperature
for case 4-1 (scenario IV at 0.5 ACH).
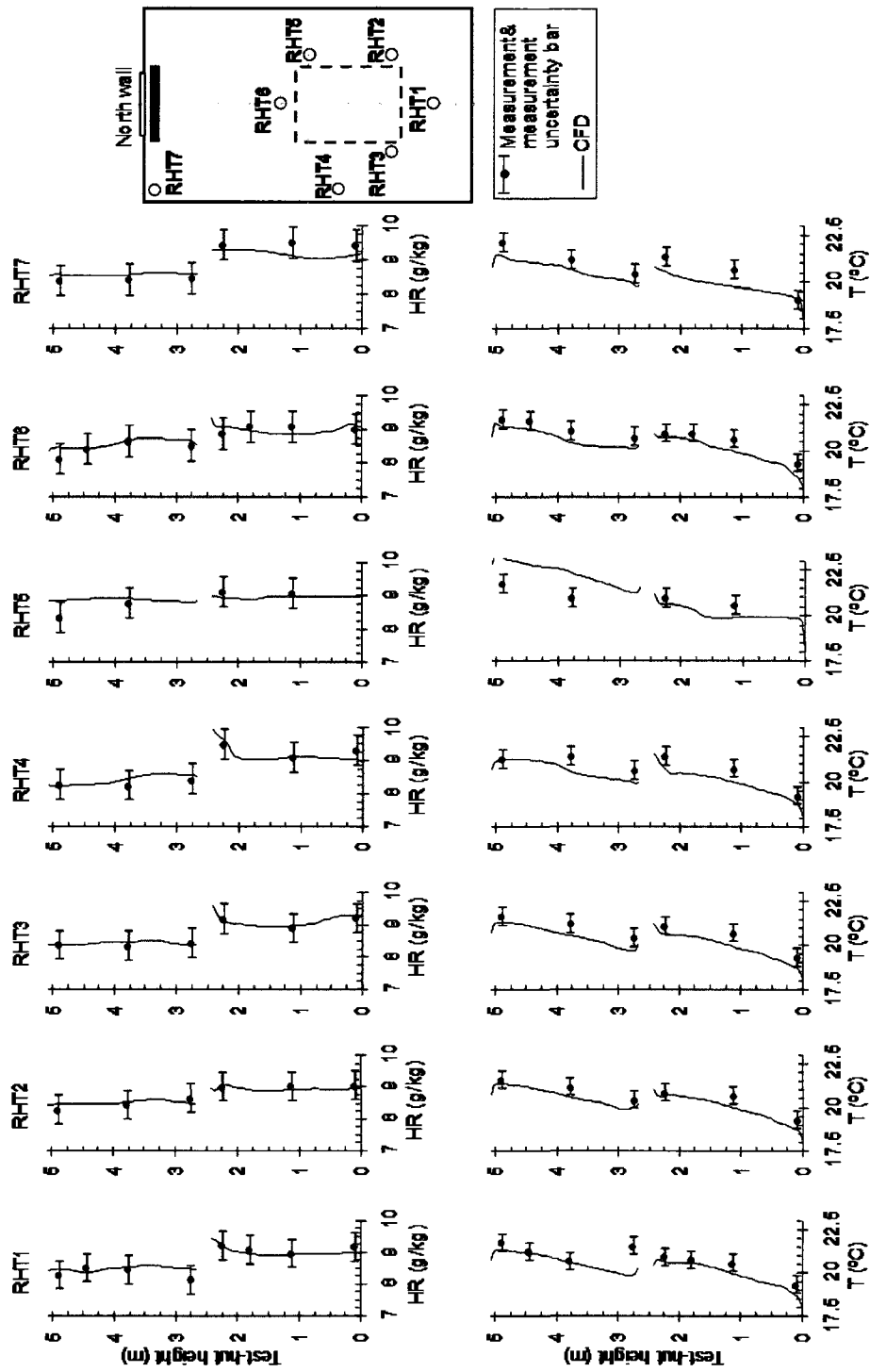
Figure 6.14: Comparison of measured and simulated distributions of humidity ratio and temperature for case 4-3 (scenario IV at 0.5 ACH).

Although there are a few differences between the computed and measured temperatures, the overall performance of the CFD model predicting temperature is good. The CFD model is able to capture the temperature differences between the two rooms and the shape of the predicted vertical temperature profiles in each location for all the cases.

The simulated and measured average temperatures and HRs in each room are also compared in Table 6.1. In general, average simulated values agree very well with measured average values. The absolute difference between the measured and simulated HR ranges from 0.03 to 0.39 g/kg for the lower room and from 0.01 to 0.57 g/kg in the upper room. These results indicate that the largest relative differences between the measured and simulated average values are 4% and 9% in the lower and upper room, respectively. On the other hand, it can be seen that simulated average temperatures are lower than the measured average values. The differences between the measured and predicted temperature are from 0.3°C to 0.7°C in the lower room, and from 0.1°C and 0.9°C in the upper room.

Table 6.1: Simulated and measured (between brackets) average temperatures and HRs.

	Lower room		Upper room	
	HR (g/kg)	Temperature (°C)	HR (g/kg)	Temperature (°C)
Case 2-1	9.1 (9.4)	21.5 (22.2)	8.8 (8.8)	18.6 (18.7)
Case 2-2	9.1 (9.3)	19.8 (20.3)	8.6 (8.7)	17.4 (17.5)
Case 2-3	9.3 (9.4)	20.0 (20.3)	8.5 (8.8)	18.4 (18.7)
Case 2-4	9.3 (9.3)	20.0 (20.4)	8.3 (8.4)	19.7 (20.2)
Case 2-5	9.1 (8.9)	20.2 (20.5)	7.3 (7.8)	20.6 (21.0)
Case 2-6	7.8 (7.9)	19.1 (19.5)	7.1 (7.5)	16.7 (17.1)
Case 2-7	7.8 (7.8)	19.5 (19.9)	6.5 (6.7)	19.5 (20.0)
Case 2-8	7.6 (7.8)	19.7 (20.3)	5.7 (6.3)	20.3 (21.2)
Case 4-1	9.0 (9.2)	19.7 (20.2)	8.9 (8.9)	18.3 (18.7)
Case 4-2	9.0 (9.4)	19.8 (20.3)	8.6 (8.8)	19.4 (20.1)
Case 4-3	9.1 (9.1)	19.9 (20.4)	8.5 (8.4)	20.7 (21.1)
Case 4-4	9.7 (9.6)	20.1 (20.4)	7.9 (7.9)	22.3 (23.1)

From the above validation, it may be concluded that CFD model in Airpak performs well in predicting relative accurate airflow field and distributions of temperature and HR. The model is able to capture the differences in temperature and HR between the upper and the lower rooms, and the differences between the scenarios and ventilation rates. Moreover, the good predictions of HR and temperature in the upper room show that the CFD model predicts the interzonal HAM transport properly because HR and temperature in the upper room are highly dependent of the interzonal mass airflows.

6.4.2 Validation for interzonal mass airflows

The interzonal mass airflows across the middle horizontal plane of the opening (z = 2.54 m) are calculated based on the CFD results for all cases in scenario II and scenario IV. The upward and downward mass airflow rates through the opening, F_{12} and F_{21}, are calculated as follows:

$$F_{12} = \sum_i \rho_{a_i} Vz_i A_i \qquad Vz_i > 0 \; (upward \; mass \; airflow \; only) \tag{6.1}$$

$$F_{21} = \sum_j \rho_{a_j} Vz_j A_j \qquad Vz_j < 0 \; (downward \; mass \; airflow \; only) \tag{6.2}$$

where ρ_a is the dry air density (kg/m^3) calculated from the predicted temperature, Vz is the z-component of the air velocity vector (m/s), and A is the cell area (m^2) on which Vz occurs.

Since the mesh grid in the opening (plane xy) is not uniform (Figure 6.15a), the areas covered by the cells vary according to their locations, making it difficult to calculate the interzonal mass airflows. For this reason, values for Vz and for the temperature over a uniform mesh grid were obtained through a smooth surface interpolation algorithm in Matlab (Sandwell, 1987). This uniform mesh is represented by the red points in Figure 6.15b against black points of the original CFD mesh. As example, the air velocity vectors

(by the arrows) and their z-axis components Vz (by the color map) across the horizontal opening over the original CFD mesh for case 2-2 are plotted in Figure 6.15c, while values of Vz over the uniform mesh grid are shown in a surface plot in Figure 6.15d. Using the uniform grid, the cell area is constant and the upward (F_{12}) and downward (F_{21}) mass airflows through the opening can be calculated with simple arithmetic averages in Matlab.
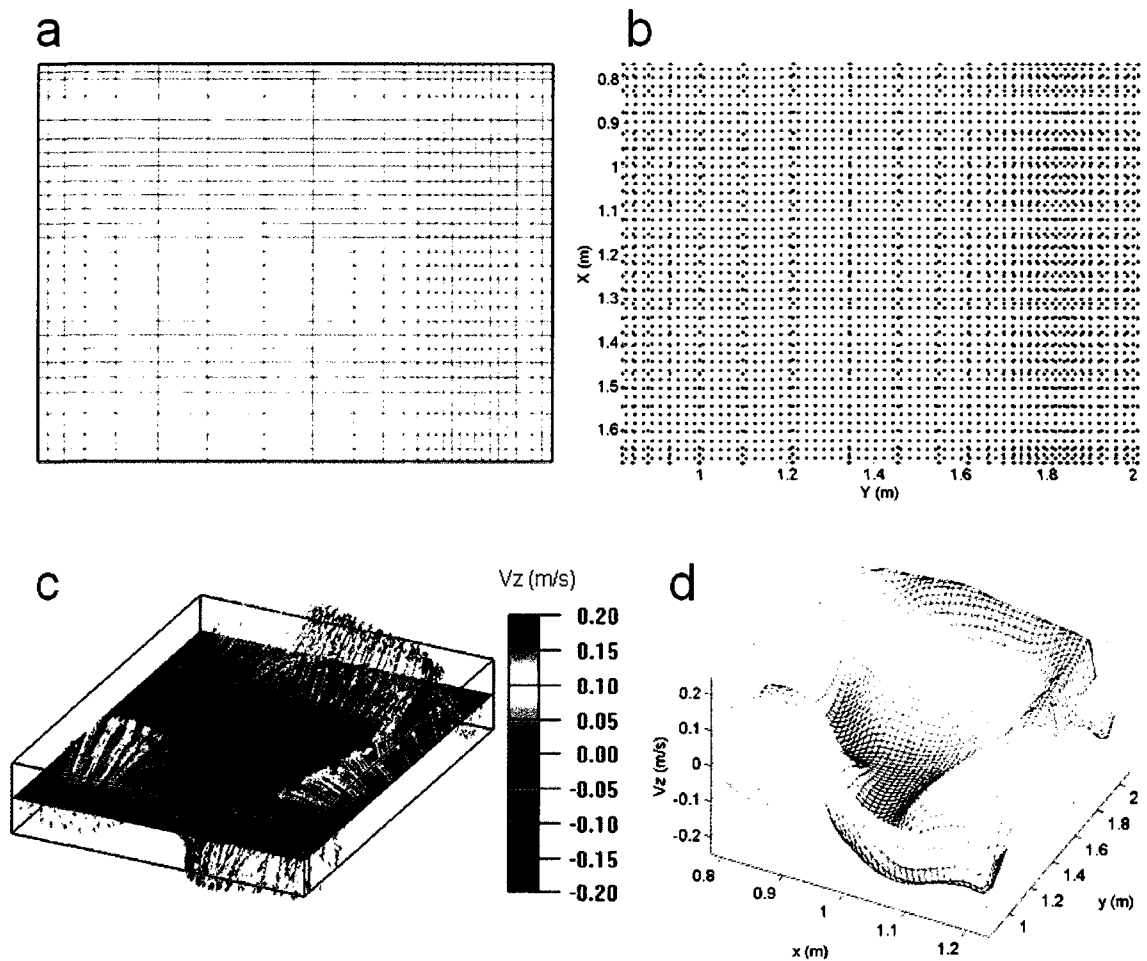
Figure 6.15: Comparisons of meshes and air velocity across the opening for case 2-2: a) original mesh grid of the CFD model, b) uniform mesh in red dots against black dots CFD mesh, c) velocity vectors in arrows superimposed over color map of z-axis components Vz in CFD mesh, and d) interpolated Vz over the uniform mesh.

The upward mass airflows obtained by means of CFD simulations are listed in Table 6.2, along with the results of the measured upward mass airflows obtained in *Chapter 5*. Although upward mass airflows can not be compared directly because $\Delta T / \bar{T}$ from simulations and from measurements are not exactly the same, some conclusions can be inferred from Table 6.2. The measured and simulated upward mass airflows for scenario II at 0.5 ACH agree very well. However, the $\Delta T / \bar{T}$ values of CFD data points are lower than those of the measured data because the CFD model under-predicts the temperature differences between the two rooms, especially for cases 2-1 and 2-2. Figure 6.16 shows the measured and simulated upward mass airflow for cases of scenario II at 0.5 ACH when the upper room is colder (cases 2-1, 2-2, 2-3 and 2-4). Power-law fitting lines are plotted for both measured and CFD data. It can be observed that the underlining relations between the temperature differences and mass airflow rates are very similar between the simulations and experiments, as can be observed by the closeness between the two regression lines from the simulated and measured values.

Table 6.2: Measured and simulated upward mass airflows.

	Measured		Simulated (CFD)	
	F_{12} (kg/s)	$\Delta T / \bar{T}$	F_{12} (kg/s)	$\Delta T / \bar{T}$
Case 2-1	0.0549	0.0118	0.0521	0.0091
Case 2-2	0.0535	0.0094	0.0511	0.0076
Case 2-3	0.0482	0.0054	0.0477	0.0047
Case 2-4	0.0268	0.0006	0.0270	0.0005
Case 2-5	0.0198	-0.0024	0.0203	-0.0013
Case 2-6	0.0621	0.0087	0.0410	0.0072
Case 2-7	0.0177	-0.0012	0.0239	-0.0007
Case 2-8	0.0094	-0.0043	0.0143	-0.0026
Case 4-1	0.0417	0.0052	0.0466	0.0044
Case 4-2	0.0205	0.0007	0.0351	0.0009
Case 4-3	0.0173	-0.0026	0.0198	-0.0033
Case 4-4	0.0069	-0.0091	0.0142	-0.0081
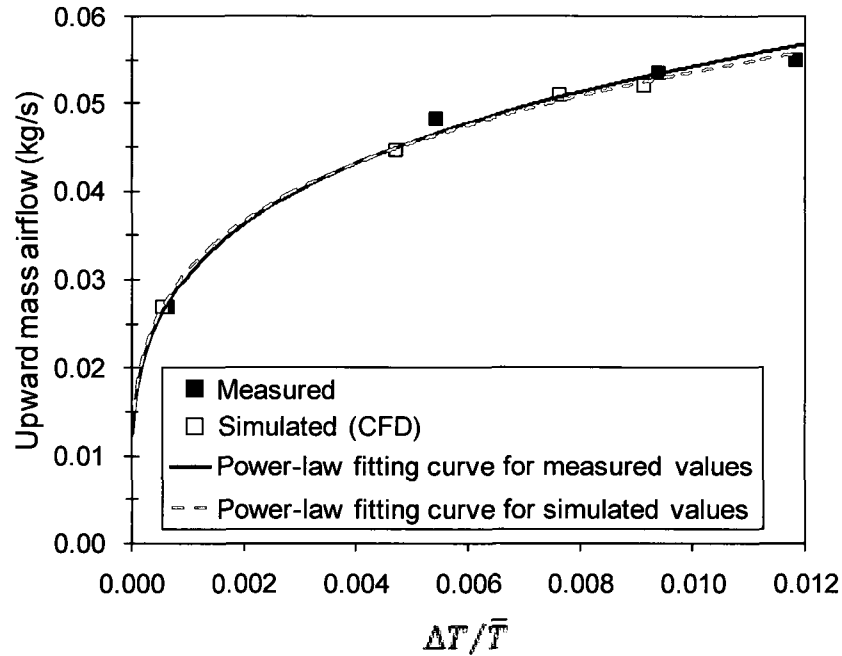
Figure 6.16: Comparison between the measured and simulated upward mass airflows for scenario II at 0.5 ACH with colder upper room.

As shown in Table 6.2, differences between the measured and simulated upward mass airflows in scenario II at 0.75 ACH are much larger than those observed in scenario II at 0.5 ACH. Much lower F_{12} value is predicted by the CFD model (0.041 kg/s) for case 2-6 than the measured value (0.062 kg/s). In this case, the measured F_{12} is too high, and even higher than the corresponding value at 0.5 ACH for similar $\Delta T/\bar{T}$ (0.053 kg/s for case 2-2). This lacks physical meaning because at higher ventilation rate should make it more difficult for the air in the lower room to go up in the scenario with downward net flow through the opening. Hence, the measured F_{12} at 0.75 ACH should be smaller than the value at 0.5 ACH. The CFD model predicts this phenomenon well. The differences found for cases 2-7 and 2-8 are expected because of the differences in $\Delta T/\bar{T}$. In these two cases, the measured upward mass airflows are lower than that predicted by the CFD model, but at the same time, the measured $\Delta T/\bar{T}$ are much higher than those predicted by the CFD model.

132

For scenario IV, cases 4-1 and 4-3 show good agreement between the measured and computed upward mass airflows. Otherwise, results do not agree well for cases 4-2 and 4-4. In both cases the measured and computed $\Delta T/\bar{T}$ are close, thus the CFD model overpredicts the upward mass airflow. Nevertheless, in the case 4-4, the overpredicted F_{12} is not critical because of the small upward mass airflows that occur when the upper room is much warmer than the lower room (ΔT equal to -2.6°C). Therefore, poor agreement between the measured and computed F_{12} was obtained only for case 4-2. For this reason, this case was excluded as baseline case of simulations reported in *Chapter 7*.

6.5 Discussion and closing remarks

This chapter shows the extensive validation of the CFD model carried out for twelve cases tested for scenarios II and IV. The first order parameters obtained from the CFD simulations, such as distribution of air speeds, temperatures and HRs, were compared with experimental measurements in more than 80 points across the two-story test-hut. Overall, good agreements were found between the computed and measured values.

Furthermore, computed interzonal mass airflows agree well with the measured values in most of the cases. For cases of scenario II at 0.5 ACH, the relative difference between the computed and the measured upward mass airflows ranged between 0.7% and 5.1%. The results are less satisfactory for scenario IV, especially for case 4-2. As a basis for comparisons, previous numerical studies with buoyancy-driven flows have reported differences below 10% between the measured and computed interzonal using more advanced turbulence models (Riffat and Shao, 1995; Peppes et al., 2001, 2002).

It should be noted that the CFD simulations provided satisfactory results for scenarios II and IV. Some cases of scenario I were also simulated, but very poor results

were obtained because the transient and unstable behavior of buoyancy-driven flows. This confirms that Chen and Xu's turbulence model is only suitable for indoor environments with mixed ventilation, such as those found in scenarios II and IV, while indoor environments with buoyancy flows need to be modeled with more advance turbulence models, such as large eddy simulation or three-equation eddy viscosity (v2f-dav) models.

CHAPTER 7

CFD RESULTS AND ANALYSIS

7.1 Introduction

Chapter 5 analyzed the air and moisture exchange between the two rooms based on experimental data. Although interesting and useful results were obtained from the experimental data, the following limitations were observed:

- Only few ventilation rates and values of ΔT were tested.

- Airflow pattern inside the test-hut can not be obtained from the omnidirectional anemometer measurements, and also the distribution of humidity and temperature can not be acquired from the measurements obtained by RH sensors. The use of a larger number of sensors and additional associated elements (e.g: DAS, wires and cables) to obtain these results would be expensive and time consuming due to longer duration of their installation and setting, and longer post-processing of data obtained.

- There are not enough data to explain some results, such as the existence of upward mass airflows when the upper room is warmer as described in section 5.3.4.

For these reasons, the validated CFD model implemented in Airpak, as presented in *Chapter 6*, has been used to investigate additional conditions to those tested experimentally, and to provide detailed spatial data for the analysis of the velocity field across the opening, the influence of the ventilation rate and ventilation strategy on interzonal mass airflow, the influence of ΔT and ventilation rate on the interzonal moisture exchange, and the causes of upward mass airflows when the upper room is warmer than the lower room. In particular, the CFD simulations were performed for scenarios II (single ventilation with downward net flow through the opening) and IV

135

(independent ventilation in each room), ventilation rates between 0.4 ACH and 1.5 ACH, and additional temperature differences between the two rooms. All the cases simulated have the same inlet conditions with supply air temperature equal to 18°C and humidity ratio equal to 4.925 g/kg, and the same moisture generation rate (109.4 g/h). The wall surface temperatures and power of baseboard heaters of cases tested in scenario II and IV were used as baseline cases with small modifications.

In total, 51 cases were simulated for scenario II, and 31 cases were simulated for scenario IV. Tables 7.1 and 7.2 summarize the ventilation rates and temperature differences between the lower and the upper rooms (ΔT) of the cases that were simulated for scenario II and scenario IV, respectively. The temperature differences shown in Tables 7.1 and 7.2 were generated by varying the power output of baseboard heaters and surface temperatures of walls, while the ventilation rates shown in these tables were generated by changing the supply airflow rate in the CFD model.

Table 7.1: ΔT at different ventilation rates of the cases simulated for scenario II.

Ventilation rate	0.4 ACH	0.5 ACH	0.625 ACH	0.75 ACH	1.0 ACH	1.5 ACH
ΔT for colder upper room	+4.1 +2.9 +2.2 +1.3 +0.1	+4.6 +2.9 +2.7 +2.4 +1.3 +0.2	+4.6 +3.2 +1.5 +0.4	+4.6 +3.7 +3.1 +2.5 +0.4	+5.3 +3.4 +3.0 +0.5	+4.9 +3.8 +2.6 +1.8 +0.5
ΔT for warmer upper room	-0.5 -0.9 -1.3 -2.2	-0.4 -0.9 -1.3 -2.2	-0.4[1] -1.3[1] -2.2[1]	-0.4 -0.9 -1.2 -2.1	-0.3 -0.8 -1.1 -2.0	-0.2 -1.0 -1.9

[1] The simulated results of these cases are used only to analyze the influence of ventilation rate on interzonal moisture exchange (section 7.5).

The CFD results presented in this chapter include the analysis of the airflow pattern across the opening, the influence of ventilation rates and ventilation strategies on the interzonal mass airflow rates, the influence of ΔT and ventilation rates on the interzonal moisture exchanges, and the existence of warm convective currents.

Furthermore, empirical equations representing the upward mass airflow through the horizontal opening are derived for cases with colder upper room and for cases with warmer upper room.

Table 7.2: ΔT at different ventilation rates of the cases simulated for scenario IV.

Ventilation rate	0.5 ACH	0.75 ACH	1.0 ACH	1.5 ACH
ΔT for colder upper room	+4.8 +3.2 +2.5 +1.3 +0.1	+4.9[1] +3.6[1] +2.5[1] +1.6[1]	+5.2 +3.7 +2.6 +1.5 +0.1	+5.3 +3.9 +1.6 +0.3
ΔT for warmer upper room	-0.4 -0.7 -0.9 -1.8 -2.4	-0.7[1] -2.3[1]	-0.1 -0.7 -1.6	-0.6 -1.6 -2.1

[1] The simulated results of these cases are used only to analyze the influence of ventilation rate on interzonal moisture exchange (section 7.5).

7.2 Airflow and moisture across the opening

Experimental results showed that two-way airflows exist across the opening. However, experimental data do not have the level of detail needed to establish how and where these flows occur. CFD simulations, on the other hand, can provide vast amount of data and detailed information of the airflow, temperature and water vapor concentration. In particular, CFD results shown in this section provide the airflow patterns across the horizontal openings as shown in Figure 7.1. This figure shows the upward vectors[3] and the temperature distribution in the middle plane of the opening (xy-plane at z = 2.54 m) at different values of $\Delta T/\bar{T}$ and at 0.5 ACH for both ventilation strategies simulated (scenarios II and IV). Figure 7.1 confirms that two-way airflow exist, even in case with an average warmer upper room. In cases with colder upper room, the warm air of the lower room moves up through the opening, while the cold air of the upper

---

[3] Note that the downward airflows are not completely shown in Figure 7.1 because they are covered by the plane showing the temperature distribution across the opening. Downward airflows occur where no upward airflows are shown.

room moves downward. Upward airflows are much stronger when the upper room is colder, while they are very weak for cases with warmer upper room.

No clear pattern of the upward mass airflows across the opening can be observed in Figure 7.1. No correlation of these airflows with $\Delta T/\bar{T}$ and ventilation strategies can be observed. This lack of correlation may be caused by the complex flow pattern in the rooms, and because of the dependency of the airflow pattern on the wall surface temperatures and the heat generation from the baseboard heaters, which are different for different cases to have several values of $\Delta T/\bar{T}$. Figure 7.2 shows the same type of results than Figure 7.1 but at 1.0 ACH instead of 0.5 ACH.

7.3 Influence of ventilation rate on interzonal mass airflow

7.3.1 Evaluation of the influence of ventilation rate on interzonal mass airflow

This section analyzes the influence of the ventilation rates (provided by mechanical ventilation) on the interzonal mass airflow for scenarios II and IV. Cases with ventilation rates of 0.4 ACH, 0.5 ACH, 0.625 ACH, 0.75 ACH, 1.0 ACH and 1.5 ACH were simulated for scenario II, whereas cases with ventilation rates of 0.5 ACH, 1.0 ACH and 1.5 ACH were simulated for scenario IV. Ventilation rates lower than 0.4 ACH were also simulated but results were not satisfactory. At these very low ventilation rates, airflow is driven mainly by buoyancy and may be considered as natural convection flow. Zhang et al. (2007) showed that indoor zero-equation model performs poorly for velocity predictions in indoor environments with natural convection flows. Moreover, Li (2007) demonstrated that the airflow through horizontal openings is highly transient and unstable in this type of flows. He concluded that advanced turbulent models, such as large eddy simulation models, have to be used to simulate the interzonal airflow through the opening.
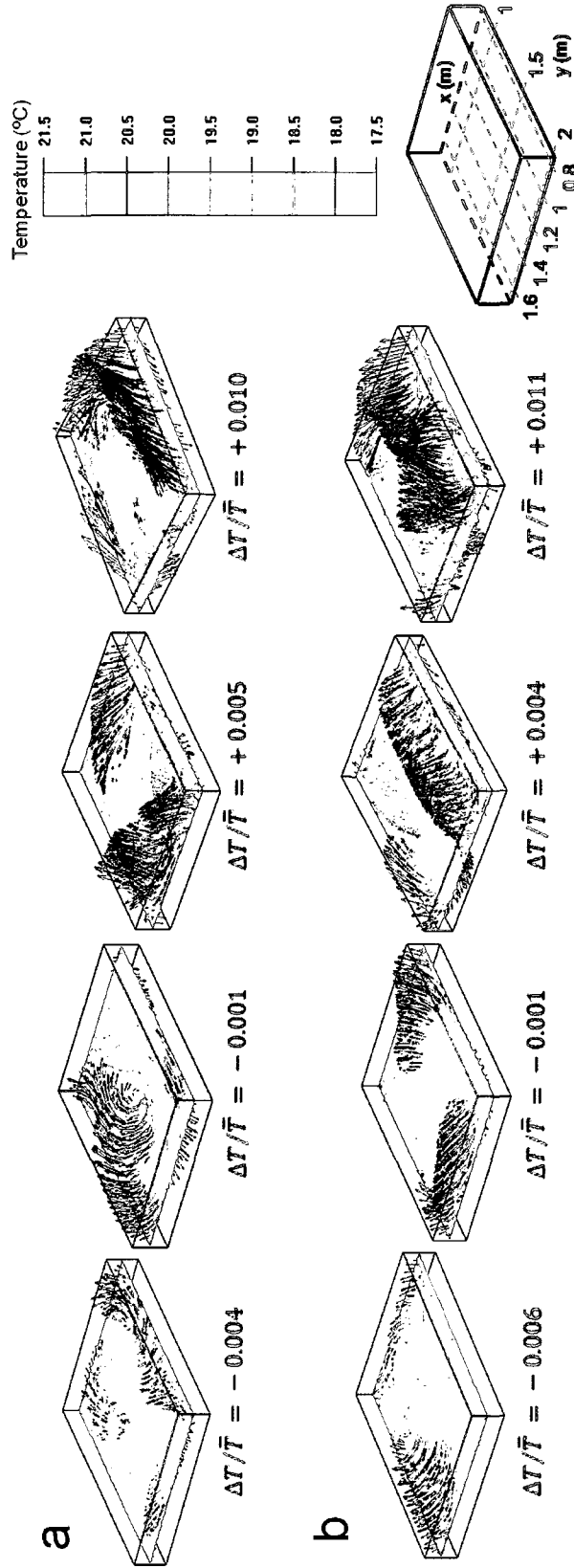
Figure 7.1: Airflow across the horizontal opening at 0.5 ACH at different values of $\Delta T/\bar{T}$: a) single ventilation with downward net flow through the opening (scenario II) and b) independent ventilation in each room (scenario IV).
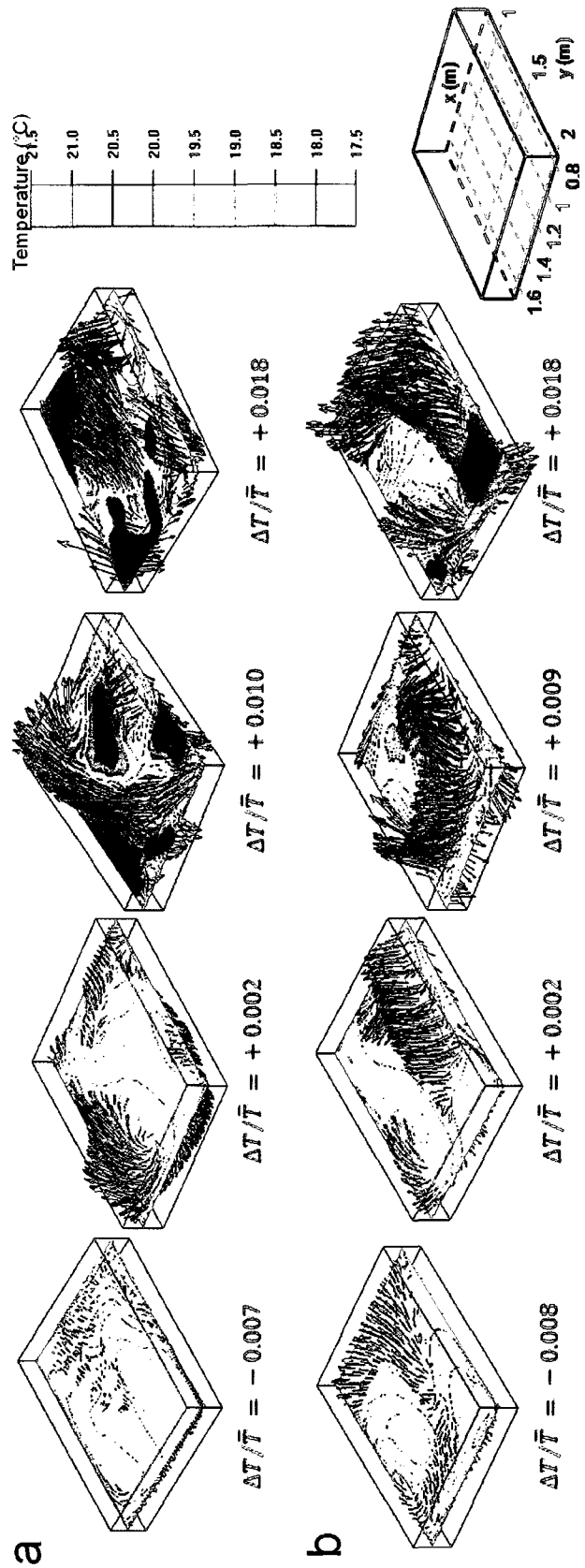
Figure 7.2: Airflow across the horizontal opening at 1.0 ACH at different values of $\Delta T/\bar{T}$: a) single ventilation with downward net flow through the opening (scenario II) and b) independent ventilation in each room (scenario IV).

140

The upward mass airflows obtained from the CFD simulations for scenarios II and IV at different ventilation rates are plotted in Figure 7.3 and 7.4, respectively. The right sides of these figures show the results when the upper room is colder than the lower room. For these cases, power-law regression curves are fitted to the computed results. The left sides of Figures 7.3 and 7.4 show the results when the upper room is warmer. For these cases, it was found that linear fitting curves agree well with the computed results.

The power-law and linear fitting curves represent the upward mass airflow through horizontal openings for combined buoyancy and forced flows. Also, Figures 7.3 and 7.4 show the curve representing the mass airflow through the opening without ventilation (0 ACH) obtained by Peppes et al. (2001) for buoyancy-driven flows through horizontal openings.
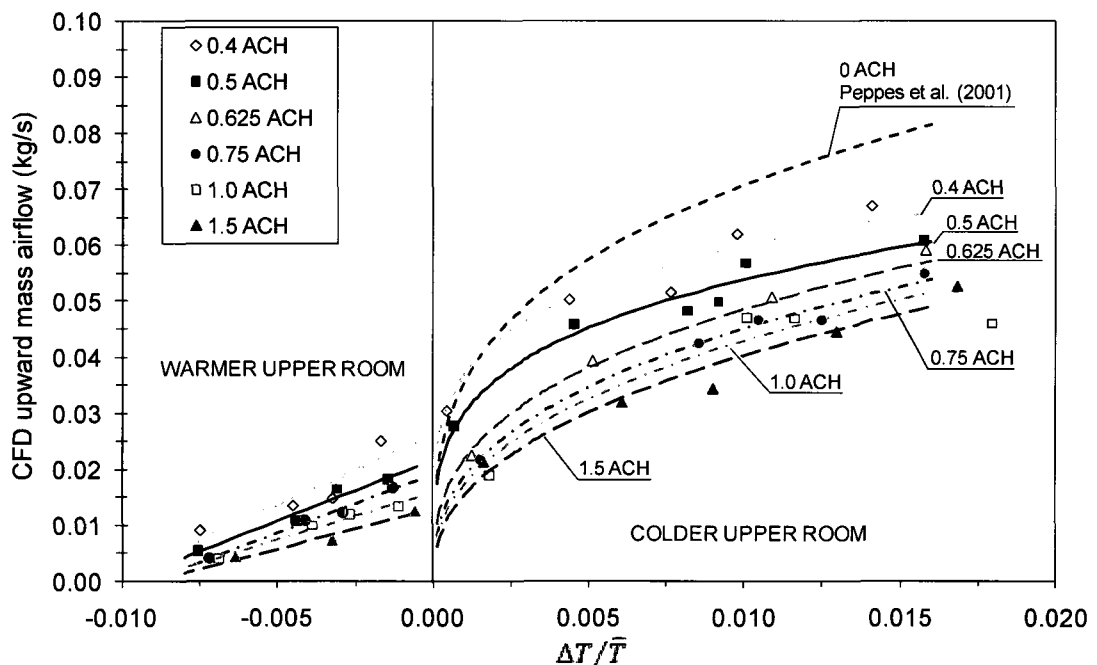
Figure 7.3: Influence of ventilation rates on upward interzonal mass airflow for scenario II.

Figures 7.3 clearly reveal that the upward mass airflow through the horizontal opening is strongly influenced by the ventilation rate for scenario II. Comparing the results for scenario II with the cases without ventilation (0 ACH), it can be observed that mechanical ventilation of scenario II significantly restricts the upward mass airflow, and hence, it would also restrict the moisture exchange between the two rooms.

Figure 7.3 shows that when the upper room is colder, much lower upward mass airflows are observed at higher ventilation rates. The same impact of the ventilation rate on the upward mass airflows can be observed when the upper room is warmer. In scenario II, these results agree well with the fact that higher downward net flow through the opening, due to higher ventilation rates, reduces the upward movement of the warm and moist air of the lower room through the opening.
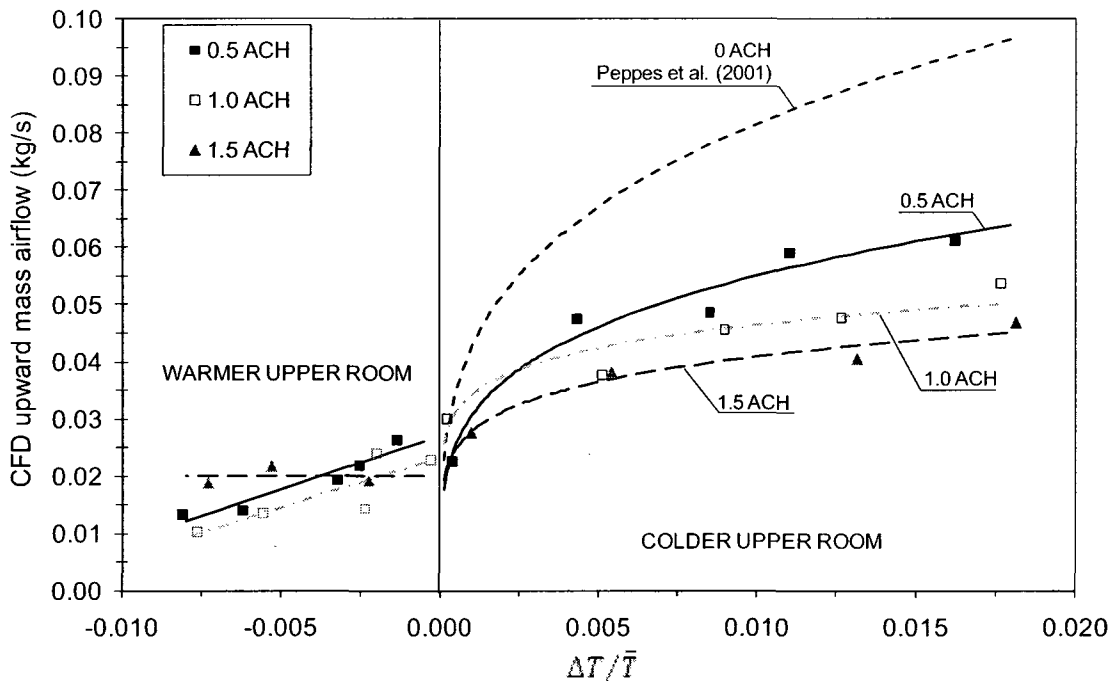
Figure 7.4: Influence of ventilation rates on upward interzonal mass airflow for scenario IV.

Figure 7.4 shows the influence of ventilation rates on upward interzonal mass airflows for scenario IV. The general trends are similar to those found for scenario II

when the upper room is colder than the lower room (right side of Figure 7.4). However, no trend showing the influence of ventilation rate on the upward mass airflow can be observed when the upper room is warmer (left side of Figure 7.4). Linear fitting curves show that the upward mass airflows through the opening at 1.0 ACH are lower than that at 0.5 ACH. Following this trend and the trend found for scenario II, values of F_{12} should be the lowest for 1.5 ACH among the cases simulated for scenario IV. Nevertheless, the data simulated at 1.5 ACH shows a completely different pattern with values of F_{12} higher than that at 0.5 ACH and values between 0.5 ACH and 1.0 ACH.

The influence of ventilation rate on the upward mass airflow is more difficult to explain for scenario IV than that for scenario II. A very small upward net flow through the opening exists in cases for scenario IV, thus the net flow through the openings would not restrict the interzonal mass airflow through the opening. Therefore, the influence of the ventilation rate on the interzonal mass airflow can not be associated directly with the impact of the ventilation rate on the downward net flow. Figures 7.5 and 7.6 show some evidences of the possible reason for the influence of the ventilation rate on the interzonal mass airflows for scenario IV. Figure 7.5 and 7.6 show the airflow field and temperature distribution in the longitudinal plane of the two-story test-hut (x = 1.22 m) at 0.5ACH, 1.0 ACH and 1.5 ACH for scenario II and IV. A strong jet flow from the supply air in the lower room for scenario IV is shown in Figure 7.6, while this supply jet flow in the lower room is absent in scenario II because the air supply was only in the upper room (Figure 7.5). In Figure 7.6, it is observed that the supply jet flow is very weak at 0.5 ACH; however, the supply jet flow is strong at 1.0 ACH and 1.5 ACH so that it extends up to the far side of the opening, and may interfere with the interzonal airflow and hamper the interzonal mass airflow. Therefore, this could be the reason of lower interzonal mass airflows at higher ventilation rates for scenario IV.
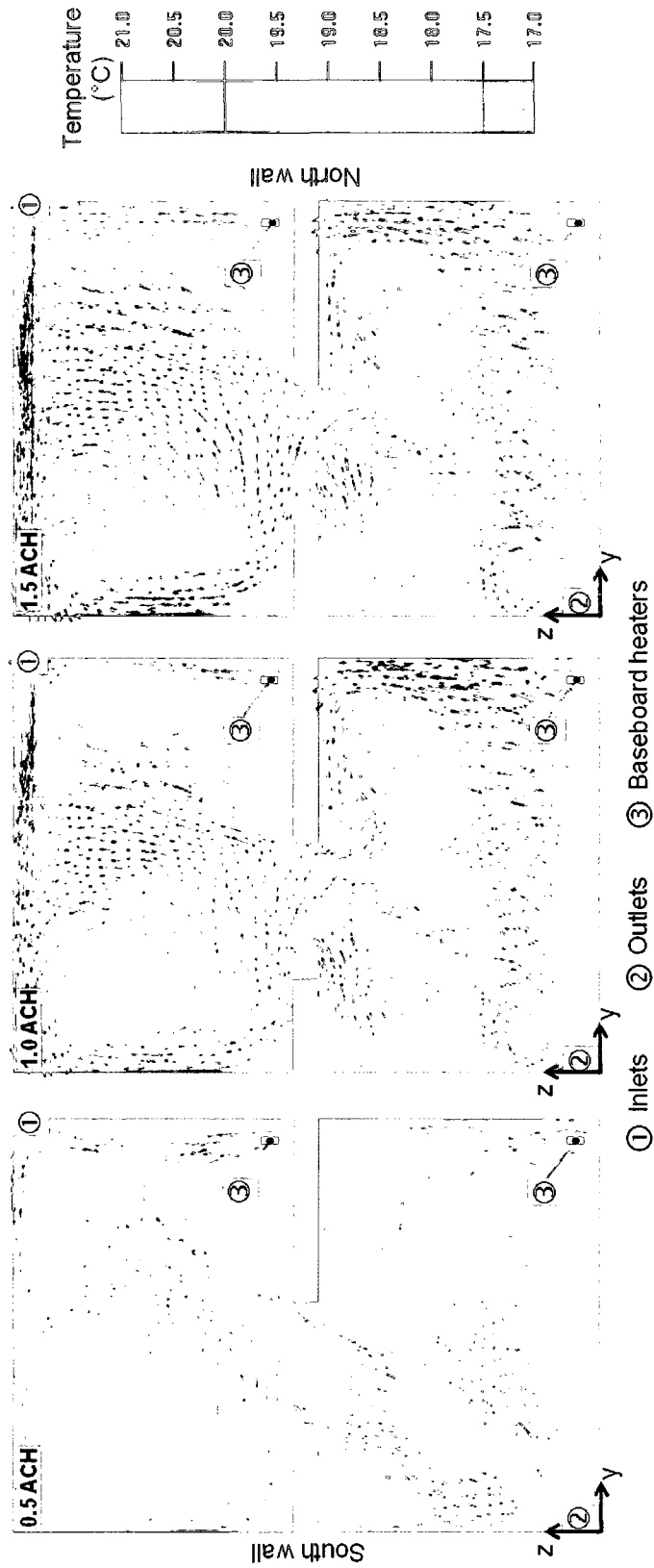
Figure 7.5: Airflow pattern and temperature distribution of cases with ΔT about 1.5°C for scenario II at different ventilation rates.

① Inlets   ② Outlets   ③ Baseboard heaters

144
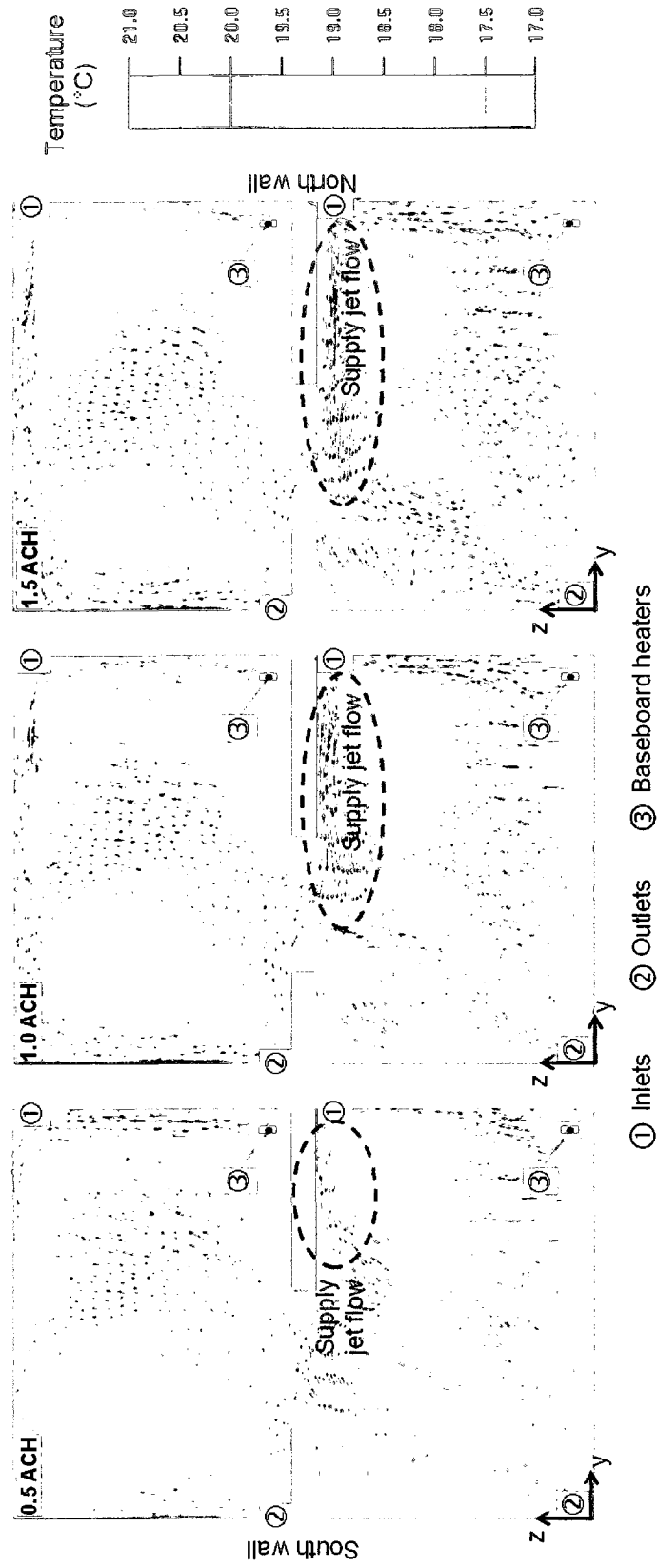
Figure 7.6: Airflow pattern and temperature distribution of cases with ΔT about 1.5°C for scenario IV at different ventilation rates.

① Inlets   ② Outlets   ③ Baseboard heaters

Temperature (°C)

21.0
20.5
20.0
19.5
19.0
18.5
18.0
17.5
17.0

0.5 ACH   1.0 ACH   1.5 ACH

South wall   North wall

Supply jet flow

7.3.2 Empirical equations derived for the upward mass airflow through horizontal openings

Chapter 2 shows that the power-law relationship between the upward mass airflow and $\Delta T/\bar{T}$ applies well for all cases reviewed with buoyancy-driven flows. Also, experimental results of *Chapter 5* show that the same power-law relationship may represent the upward airflow through horizontal opening for cases with mechanical ventilation and with the upper room colder than the lower room. This is confirmed by the CFD results shown in section 7.3.1 for additional ventilation rates. Thus, the upward mass airflow through the opening, when the upper room is colder than the lower room, may be expressed as follows:

$$F_{12} = C\rho_a A\sqrt{gH}(\Delta T/\bar{T})^n \tag{7.1}$$

where ρ_a is the air density (kg/m³), A is the opening area (m²), g is the acceleration due to gravity (m/s²), and H is the opening thickness (m). C is the constant of proportionality which was derived from the geometry of the opening tested (A is 1.08 m² and H is 0.22 m) and ρ_a is equal to 1.2 kg/m³. n is the fitting constant. C and n are given in Table 7.3 for different ventilation rates for scenario II and IV.

Unlike the cases with buoyancy-driven flows through horizontal opening, CFD results shown in Figures 7.3 and 7.4 reveal that non-zero upward mass airflows should exist in the absence of a temperature gradient between the two rooms ($\Delta T/\bar{T}$ = 0) due to upward mass airflows were found when the upper room was warmer. In consequence, the power-law flow equations can not be extended up to $\Delta T/\bar{T}$ = 0 as shown in Figures 7.3 and 7.4.

Similarly to the cases with colder upper room, the upward mass airflow equation when the upper room is warmer may be written as follows:

$$F_{12} = C\rho_a A\sqrt{gH}(\Delta T/\bar{T}) + b \tag{7.2}$$

where ρ_a is the air density (kg/m^3), A is the opening area (m^2), g is the acceleration due to gravity (m/s^2), and H is the opening thickness (m). C is the constant of proportionality which was derived from the geometry of the opening tested (A is 1.08 m^2 and H is 0.22 m) and ρ_a is equal to 1.2 kg/m^3. C and b are given in Table 7.4 for different ventilation rates for scenario II and IV.

Like the cases with colder upper room, in the vicinity of $\Delta T/\bar{T}$ near zero, the interzonal mass airflows across the opening may be unstable and difficult to estimate experimentally and numerically, thus Eq. 7.2 may not apply in this region. Further studies are required to investigate the interzonal mass airflow in this region.

Table 7.3: Values of C and n of Equation 7.1 at different ventilation rates.

	0 ACH	0.4 ACH	0.5 ACH	0.63 ACH	0.75 ACH	1.0 ACH	1.5 ACH
Scenario II							
C	0.147	0.082	0.089	0.126	0.135	0.139	0.149
n	0.300	0.209	0.252	0.348	0.380	0.397	0.419
Scenario IV							
C	0.147		0.092			0.045	0.046
n	0.300		0.255			0.133	0.167

Table 7.4: Values of C and b of Equation 7.2 at different ventilation rates.

	0 ACH	0.4 ACH	0.5 ACH	0.63 ACH	0.75 ACH	1.0 ACH	1.5 ACH
Scenario II							
C		0.1285	1.1321		1.071	0.865	0.729
b		0.026	0.022		0.019	0.016	0.013
Scenario IV							
C			0.972			0.895	
b			0.027			0.023	

7.4 Influence of ventilation strategy on interzonal mass airflow

Besides the influence of the ventilation rate and the temperature difference between the two rooms on the interzonal mass airflow, the ventilation strategy also could influence F_{12} due to its influence on the airflow pattern across the room and on the net flow through the openings. This influence can be seen in Figure 7.7, which shows the characteristic flow curves for the ventilation strategies analyzed, single ventilation with downward net flow through the opening (scenario II) and independent ventilation in each room (scenario IV), at 0.5 ACH, 1.0 ACH and 1.5 ACH.
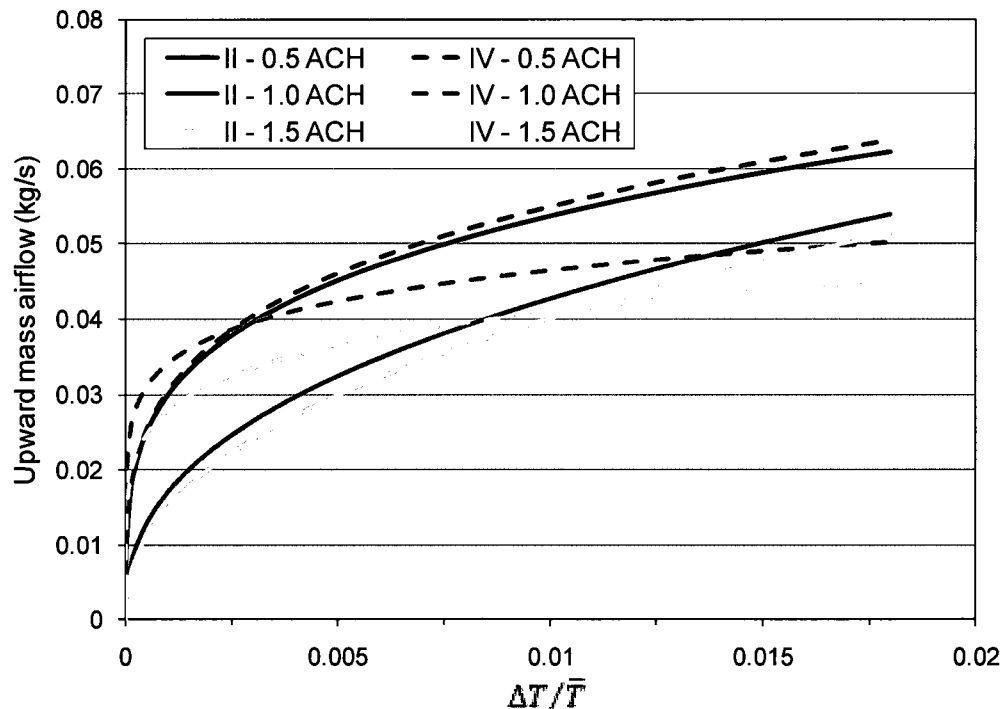
Figure 7.7: Influence of ventilation strategies on upward mass airflow.

First, it can be observed that the upward mass airflow is higher for independent ventilation than that for single ventilation with downward net flow at 0.5 ACH, at 1.0 ACH with $\Delta T/\bar{T}$ below 0.014, and at 1.5 ACH with $\Delta T/\bar{T}$ below 0.011. This result agrees well with the fact that single ventilation with downward net flow through the opening restricts the upward mass airflow, while cases with independent ventilation have negligible net

flow through the opening, which contributes to improve the air exchange between the lower and the upper rooms. This result is also supported by the conclusions obtained from experimental data about moisture exchange between the two rooms, which show that better interzonal moisture exchange occurred with independent ventilation (see section 5.2.2.c and Figure 5.3).

Second, Figure 7.7 shows that the power-law fitting curves for scenario II and IV are very close at 0.5 ACH. However, this situation changes considerably at higher ventilation rates, thus significant differences exist between the curves representing the upward mass airflow through the opening for scenario II and IV at 1.0 ACH and 1.5 ACH. For smaller temperature differences between the two rooms, F_{12} for scenario IV is much higher than that for scenario II at the same $\Delta T/\bar{T}$, but when the upper room is much colder, the opposite occurs. Further research is needed to clarify why F_{12} for scenario II is higher than that for scenario IV at the same $\Delta T/\bar{T}$ when the upper room is much colder.

7.5   Influence of ventilation rate and ΔT on interzonal moisture exchange

Chapter 5 shows that the temperature differences between the lower and the upper rooms influence the interzonal moisture exchange. The interzonal moisture exchange was represented in terms of the difference in the average humidity ratio between the two rooms (ΔHR). Since limited ventilation rates were tested, no conclusion about the influence of the ventilation rates on the moisture exchange was drawn. For this reason this section addresses this issue based on simulation results.

Figures 7.8 and 7.9 plot the relative ΔHR (ratio between ΔHR and the minimum between the average humidity ratio of the lower and the upper rooms) and the dimensionless temperature difference between the two rooms ($\Delta T/\bar{T}$). Higher relative ΔHR values indicate lower interzonal moisture exchange due to higher difference in HR

between both rooms, whereas lower relative ΔHR values mean that higher interzonal moisture exchange exists. Exponential fitting curves were fitted to the simulation results with correlation coefficients above 0.9.

Figures 7.8 and 7.9 show a strong effect of the temperature difference between the two rooms on the interzonal moisture exchange as previously shown from experimental results in *Chapter 5*. Interzonal moisture exchange is very poor when the upper room is much warmer than the lower room (left side of the figures), while the moisture exchange is much better when the upper room is colder than the lower room (right side of the figures). These results agree well with the fact that upward mass airflow are higher when the upper room is colder, thus more moisture is transported upward through the opening from the lower room and the moisture exchange improves.
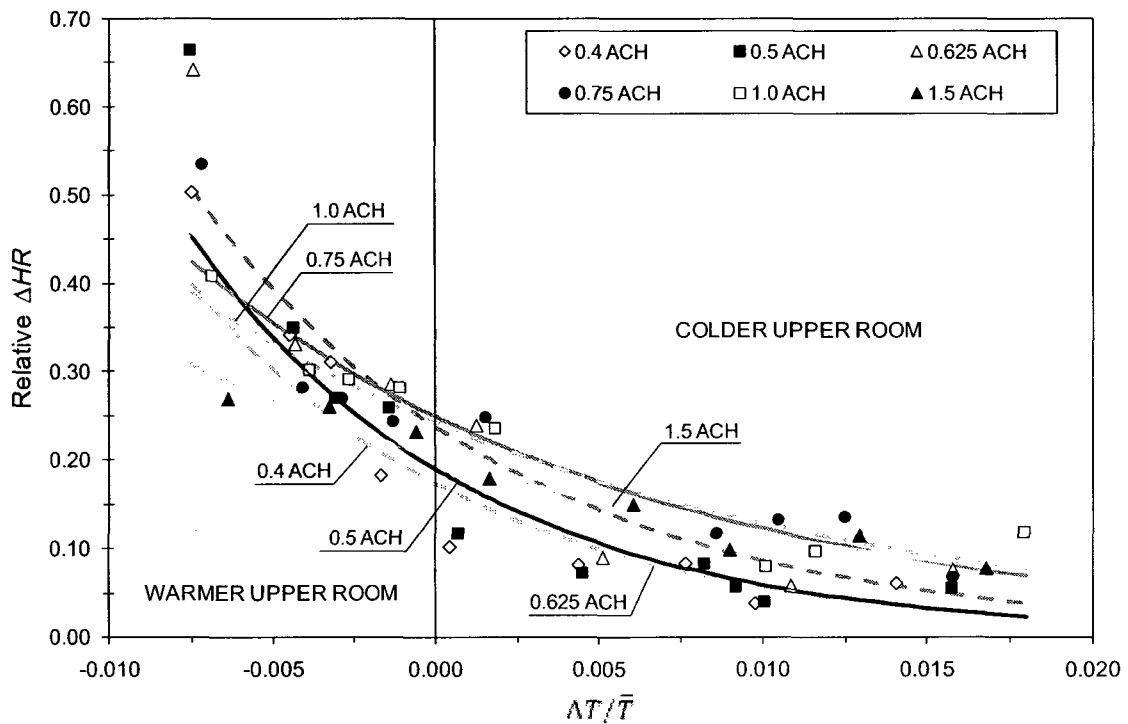
Figure 7.8: Influence of ΔT and ventilation rates on interzonal moisture exchange for scenario II.

150
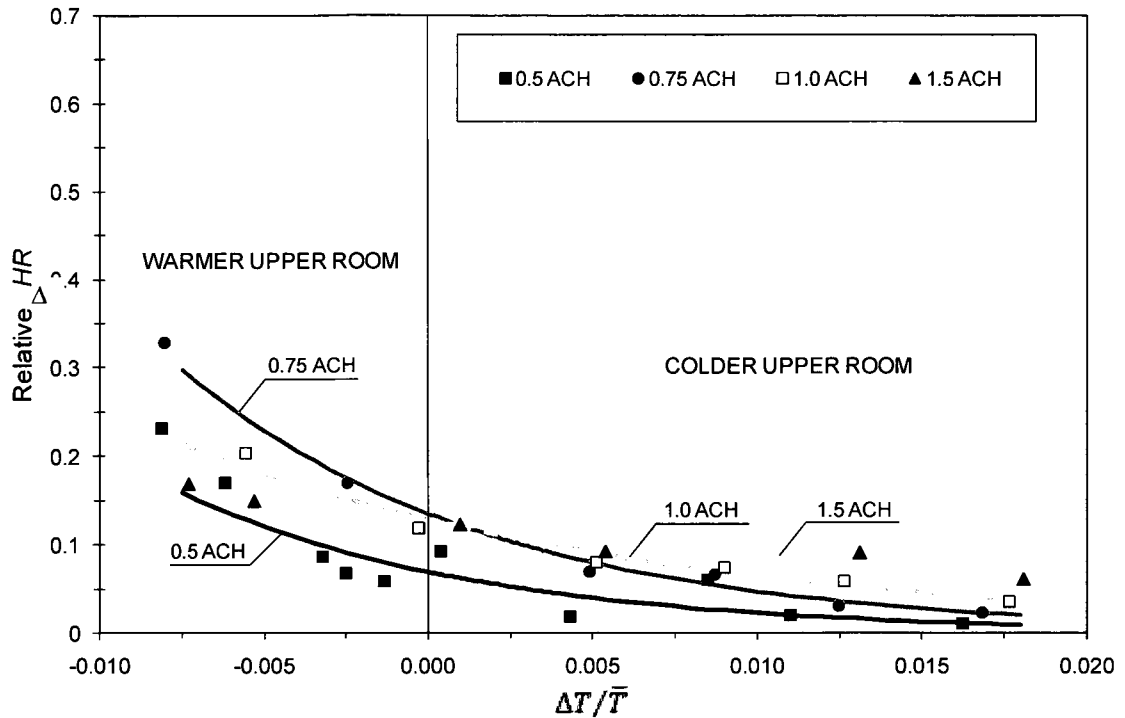
Figure 7.9: Influence of ΔT and ventilation rates on interzonal moisture exchange for scenario IV.

The influence of the ventilation rates on the interzonal moisture exchange is less clear than the influence of ΔT. The general trend shown in Figures 7.8 and 7.9 is that the relative ΔHR is higher at higher ventilation when the upper room is colder. In scenario II, lower relative ΔHR values occur at 0.4 ACH and 0.5 ACH, whereas higher relative ΔHR values are observed at 0.75, 1.0 and 1.5 ACH. However, curves at 0.75 ACH, 1.0 ACH and 1.5 ACH are very close. Therefore, results for scenario II are not conclusive, whereas results for scenario IV show more consistent results when the upper room is colder. Figure 7.9 clearly shows that interzonal moisture exchange improves at lower ventilation rates, while less interzonal moisture exchange occurs at higher ventilation rates.

When the upper room is warmer than the lower room, results lead to no observable influence of the ventilation rates on the interzonal moisture exchange for scenarios II and IV.

7.6 Warm convective currents in cases with warmer upper room

The analysis of experimental results, as well as CFD simulation results, show that smaller upward mass airflows occurred when the upper room was warmer than the lower room, even in the case with no ventilation. In *Chapter 5*, it was assumed that warm convective currents from the baseboard heater and moisture source placed in the lower room may have caused non-uniform temperature distribution above and below the opening that may have driven airflows through the opening. The experiment did not provide detailed data to confirm this hypothesis. On the other hand, visualization of the CFD simulation results may help to understand this phenomenon in this section.

Figure 7.10 shows the temperatures and air velocities at different planes of the test-hut at $\Delta T/\bar{T}$ = -0.001. The upward airflow through the opening occurs mainly close to the east edge of the opening (between x~1.3 m and the east edge of the opening at x = 1.675 m) as shown in Figure 7.10a. Figure 7.10b shows the temperature distribution and velocity field in the longitudinal plane at x = 1.6 m. It can be observed that warm air arises from the baseboard heater placed in the lower room and propagates along the ceiling. Figure 7.10b reveals that this warm current under the platform reaches the opening and flows through it. Also, a thick layer of warm air is formed under the opening and extends beneath the platform reaching the west wall. The temperature of this air layer is higher than the air above the opening, which also drives minor upward airflows. Similar phenomenon occurs due to the moisture generation system (Figure 7.10c), and in other zones with warm air zones beneath the platform and under the opening (Figure 7.10d).
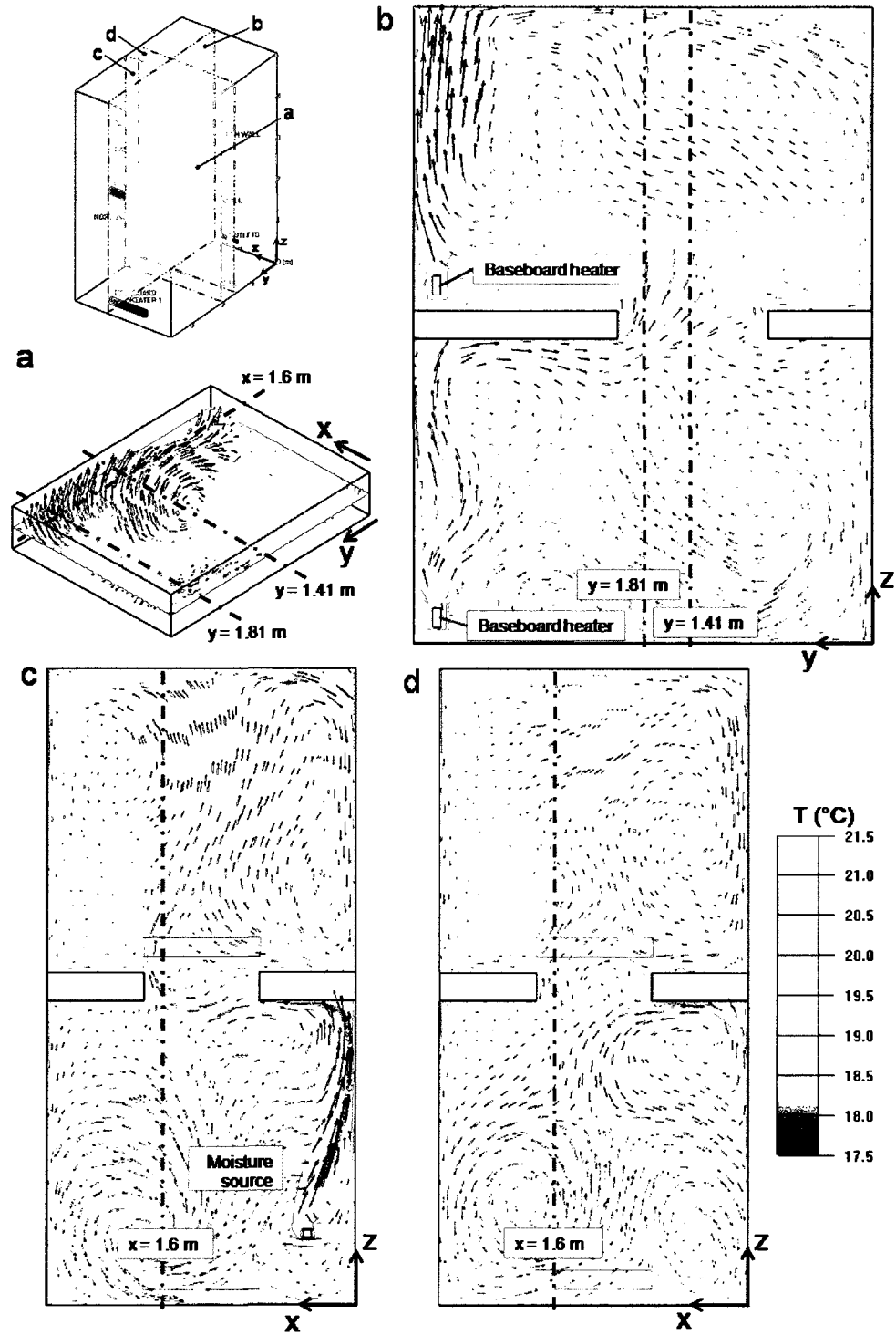
Figure 7.10: Visualization of warm gravity currents for case at $\Delta T/\overline{T}$ = -0.001 and at 0.5 ACH: a) upward airflow through the opening, b) longitudinal cross section at x = 1.6 m, c) elevation cross section at the center of the room (y = 1.81 m) and d) elevation cross section at the center of the opening (y = 1.41 m).

CFD results confirm that warm convective currents under the platform reach the opening. Because these air currents are at higher temperatures than the air above the opening, upward transport of air and moisture through the opening occurs. These warm convective currents occurred also in cases with the upper room colder than the lower room as shown in Figures 7.5 and 7.6. However, the relative contribution of these warm convective currents to the interzonal mass airflows when the upper room is colder is significantly lower than that in cases with warmer upper room because of the larger influence of ΔT on the interzonal mass airflows when the upper room is colder.

7.7 Discussion and closing remarks

The validated CFD model was used to carry out more than 80 simulations at conditions close to those tested experimentally and at new conditions that were not tested experimentally. CFD simulations were performed only for scenario II and IV, which involve buoyancy and forced driven flows (mixed convection). The CFD study allowed expanding significantly the results obtained in *Chapter 5* and analyzing the influence of ventilation rate and additional temperature differences between the two rooms on the interzonal air and moisture exchange. Also, the CFD results allowed the spatial visualization of the air velocity, and of the distribution of temperature and humidity. Thus, it was possible to analyze the airflow field through the opening as well as the existence of warm convective currents in the two-story test-hut.

Conclusive results were obtained about the influence of the ventilation rates on the interzonal mass airflows when the upper room was colder than the lower room for both ventilation strategies simulated (scenarios II and IV). From these results, power-law flow equations were derived for each ventilation rate and ventilation strategy, and they may be applied in whole-building HAM models for better predictions of indoor humidity in multizone buildings.

Also, a strong influence was found of ΔT on the interzonal moisture exchange at any ventilation rate. Moisture exchange is higher at colder upper room, whereas it is lower at warmer upper room. Also it was found that the ventilation rate significantly impact the interzonal moisture exchange at colder upper room; as ventilation rate increases, the moisture exchange between the two rooms decreases..

Finally, it was confirmed that warm convective currents play a significant role in the interzonal mass airflow when the upper room is warmer than the lower room. However, the impact of the heating device type, its operation, and its location in the rooms on the interzonal airflow needs further study.

CHAPTER 8

CONCLUSIONS, CONTRIBUTIONS AND FUTURE WORK

8.1 Conclusions

Indoor humidity in buildings can significantly impact the human comfort, indoor air quality, occupant's health, building durability and energy consumption. Indoor humidity in a room is the results of the room's moisture balance. Several aspects impact the moisture balance in the room, and hence, the indoor humidity level. Some of these aspects are the moisture generation by sources, moisture absorbed or released by hygroscopic indoor finishing materials and furniture, moisture absorbed or released during condensation and evaporation processes, moisture transported through the envelope, moisture transported by air leakage and ventilation, and interzonal moisture transported through doorways and staircase openings. Most of these aspects have been studied but scarce attention has been put on the study and evaluation of the interzonal moisture transport.

Estimation of interzonal moisture transport is essential to predict the humidity level in all zones (rooms) of multizone buildings (e.g. dwellings). Interzonal airflows carry moisture and help transporting it from one room to another. Airflow through vertical openings, such as doorways and windows, is a well understood phenomenon and several empirical equations based on experiments and simulations have been developed to calculate interzonal airflow through large vertical openings. These equations can be used to estimate interzonal moisture transported by air. On the other hand, only a very few studies have been carried out to understand the buoyancy-driven flows through horizontal openings. These flows are caused only by temperature differences between both sides of the opening and the resulting upward and downward airflows through the opening are equal. *Chapter 2* showed that large variations exist

among the interzonal airflows given by empirical equations derived by different researches.

In real buildings, interzonal airflows through horizontal openings are driven not only by buoyancy forces, but also by pressure differentials induced by mechanical ventilation and wind. Under these conditions, buoyancy and forced flows are developed and a net flow through the opening may occur. Unfortunately, these types of flows have not been studied experimentally or numerically except by the single study carried out in a small-scale setup by Klobut and Sirén (1994). Although the temperature difference between both side of the opening, the ventilation rate and the direction of the net flow through the opening were studied by them, no flow equations through the opening were obtained. Without these flow equations it is not possible to calculate the amount of moisture transported through the horizontal opening and no accurate predictions of humidity can be obtained in the different building zones.

Consequently, the aim of this investigation was to study the interzonal air and moisture transport through a large horizontal opening in a full-scale two-story test-hut involving buoyancy driven flows (due to temperature differences only) and combined buoyancy and forced airflows (due to temperature differences and mechanical ventilation). To accomplish this objective a full-scale two-story test-hut was built inside the environmental chamber at Concordia University. The main parameters tested were the temperature difference between the lower and upper rooms, ΔT (between -2.7°C and +3.5°C), and four scenarios (I, no ventilation and moisture source placed in the lower room; II, single ventilation with downward net flow through the opening and moisture source placed in the lower room; III, single ventilation with downward net flow through the opening and moisture source placed in the upper room; and IV, independent ventilation in each room and moisture source placed in the lower room). Air speed, temperature and humidity were monitored across the two rooms and into the opening as

well as other parameters related to the boundary conditions (e.g. ventilation flow rate, wall surface temperature). *Chapter 5* presented and analyzed the experimental results for scenarios I, II, III and IV in terms of two quantities: (*i*) the interzonal moisture exchange (ΔHR), and (*ii*) the measured interzonal mass airflows (F_{12} and F_{21}). The moisture exchange between the upper and the lower rooms is the results of the interzonal mass airflows. Therefore, lower values of ΔHR, that mean higher moisture exchange between the two rooms, are caused by higher interzonal mass airflow.

On the modeling front, steady-state and 3D CFD simulations were performed using Airpak, a commercial CFD software, to extend the conditions tested experimentally for scenario II and IV. The CFD model used the indoor zero-equation model developed by Chen and Xu (1998). Although this model is one of the simplest turbulence models, it was successful in predicting the air speeds, temperatures and HRs across the two rooms as well as the interzonal mass airflow through the horizontal opening for scenarios II and IV.

The main conclusions that can be drawn from the integrated experimental measurements and CFD simulations are presented below.

Airflow and moisture exchange across the horizontal openings

- Experimental and CFD simulation results confirm that two-way airflows exist through the horizontal opening in all cases. In cases with a colder upper room, the warm air of the lower room is transported upward through the opening due to temperature differences between the two rooms, and the cold air in the upper room moves downward through the opening.

- Small upward mass airflows exist when the upper room is warmer than the lower room, even in cases without ventilation. Visualization of the CFD simulation results reveals that the main cause of these flows is the existence of warm convective

currents arising from the baseboard heater in the lower room and from the moisture source.

These warm convective currents propagate under the platform. In some cases, the warm convective currents flow directly upward through the opening, while in other cases they extend under the opening forming zones of warmer air than that above the opening, which also drive warm air upward through the opening.

- Water vapor always moves with interzonal airflows from the room with a higher humidity ratio to the other room. Vapor diffusion through the opening is negligible and two orders smaller than the convective moisture exchange through the opening.

- No correlation was found among the location where interzonal mass airflows occur across the opening, ΔT, ventilation rates and ventilation strategies.

Influence of ΔT, ventilation strategies and ventilation rates on the interzonal air and moisture exchange

- The interzonal moisture exchange and the interzonal mass airflows highly depend on the temperature difference between the two rooms. While smaller ΔHR and higher upward mass airflows occur when the upper room is much colder, higher ΔHR and much smaller interzonal mass airflows exist when the upper room is as warm as or warmer than the lower room.

- Interzonal air and moisture transport through the horizontal opening is also linked to the ventilation strategy. In comparison with cases without ventilation, mechanical ventilation significantly restricts the interzonal mass airflows, which may restrict the moisture exchange between the two rooms.

Comparison between the results for single ventilation with downward net flow through the openings and independent ventilation in each room indicates that

independent ventilation improves air and moisture exchange through the horizontal opening. This conclusion is supported by the smaller values of ΔHR obtained experimentally and higher upward mass airflows obtained via CFD simulation for cases with independent ventilation than those obtained for single ventilation. This result confirms the fact that the strong downward net flow through the opening with single ventilation hampers the upward mass airflows, and hence, the moisture exchange.

- The ventilation rate influences the interzonal mass airflows too. Via CDF simulations for scenarios II and IV, it was observed that at higher ventilation rates, the upward mass airflows are smaller. Also, it was found that higher ventilation rates inhibit interzonal moisture exchange when the upper room is colder. No conclusive trend was found for the influence of ventilation rate on the interzonal moisture exchange when the upper room is warmer than the lower room.

Empirical correlations for the interzonal mass airflow

When the upper room is colder than the lower room, the following results are observed:

- In general, experimental and CFD simulation results show that power-law equations represent well the relationship between the upward mass airflow through the openings and ΔT when the upper room is colder than the lower room.

- Two cases tested experimentally for scenario I (no ventilation with colder upper room) fit very well with the flow equation derived by Peppes et al. (2001) for buoyancy-driven flows through horizontal openings. Thus, interzonal mass airflows can be calculated as $F = C\bar{\rho}A\sqrt{gH}(\Delta T/\bar{T})^n$, where C is 0.1469 and n is 0.3. This equation is similar to the generic form of the orifice flow equation but $\Delta T/\bar{T}$ is powered to 0.3 instead of 0.5.

- Although the mechanical ventilation restricts the upward mass airflow, it can still be represented by the above generic power-law flow equation with different values for C and n, which vary according to the ventilation rate and ventilation strategy and were given in Table 7.3.

Several cases were tested and simulated with warmer upper room condition, but the results were not conclusive. Nevertheless, linear relations describe the dependence of the upward mass airflows through horizontal openings on the temperature differences between the two rooms in such cases.

CFD simulation

The following conclusions can be obtained on the CFD simulation itself:

- It is proven that Chen and Xu's indoor zero-equation model is able to predict air speed, temperature and humidity across the two-story test-hut and in the opening for cases with combined buoyancy and forced driven flows (scenarios II and IV). Moreover, the CFD model has the capabilities to predict interzonal air and moisture exchange through the horizontal opening. In contrast, the model fails to provide reasonable results for cases without mechanical ventilation (scenario I).

- The way that the moisture source and ventilation inlets are modeled is crucial to obtaining good predictions of the airflow pattern and distribution of air temperature and humidity. At least half of the modeling effort used in the simulations was dedicated to properly setting up these two aspects in the CFD model.

- In most of the cases simulated, convergence was reached between 2 and 3 hours. This shows that a simple turbulence model as the one used in this thesis research can provide good results in short time, which makes the validated CFD model suitable to be used for parametric studies in short time.

8.2 Contributions

This thesis research has four main contributions to the understanding of the air and moisture exchanges through large horizontal openings under natural and mechanical ventilation.

- Empirical correlation equations have been developed to represent the interzonal mass airflow through horizontal openings for cases with combined buoyancy and forced driven flows. These equations may be implemented in whole-building HAM models to better predict air and moisture transport, indoor humidity, heat transfer, and contaminant transport in multizone buildings.

- CFD simulations have been successfully applied to study combined buoyancy and forced driven flows in a two-story test-hut with a large horizontal opening. This extends the existing numerical studies on buoyancy-driven only flows in two-story setups.

- A procedure for measuring interzonal air and moisture mass transports through horizontal openings has been developed. This procedure considers water vapor as tracer gas and employs both a steady-state difference algorithm and an integral method. The results correspond well with the air speed measurements in the horizontal opening.

- Extensive and reliable experimental data have been collected that can be used to validate ongoing and future developments of multizone whole-building HAM models for predicting indoor humidity in multizone buildings. Also, the extensive monitoring of indoor air conditions on air speed, temperature and humidity can be used to validate CFD models. Complete experimental datasets for some of the cases included in this thesis have been integrated as part of the final report and CD of IEA Annex 41, *Whole Building Heat, Air and Moisture Performance*.

8.3 Suggestions for future work

Besides the conclusions, non-conclusive or incomplete results as well as question arising from the research are also important because they bring to light needs for future works. Suggestions for future works derived from this thesis are the followings:

- Scenario I (no ventilation) needs to be simulated with more advanced CFD models, such the RNG k-ε model or the three-equation eddy viscosity model (v2f-dav), that are able to capture the highly transient and unstable behaviour of buoyancy-driven flows through horizontal openings (Riffat and Shao, 1995; Li, 2007).

- More experimental scenarios are needed to be tested for cases with a warmer upper room. This research tested few cases and some trends were found but results are not conclusive. The impact of the heating of baseboard heaters and their locations on the warm convective current, and hence, on the interzonal mass airflow and moisture exchange need further investigations

- Experiments and simulations were carried out with non-hygroscopic materials, thus no moisture interaction occurred between the indoor air and interior finishing materials. However, in real conditions, moisture absorbed by indoor finishing materials and furniture may inhibit the interzonal moisture exchange (Woloszyn, 1999) and may significantly influence the moisture distribution. Advances in this field have been carried out by Steeman et al. (2008) who coupled the effective penetration depth model of Cunningham (1992), that account for the moisture buffered by indoor finishing materials, and CFD in Fluent for single rooms. Therefore, it is recommended to extend the validated CFD in this thesis research to account the moisture buffering effect and its influence on the interzonal moisture exchange and moisture distribution.

- It is known from several studies with buoyancy-driven flows that the opening size (Brown, 1962; Peppes et al., 2001) and the ratio between the length and thickness of the opening (Brown, 1962; Epstein, 1988; Li, 2007) influence the interzonal mass airflow. Therefore, extended experimental testing and parametric analyses via CFD simulations including these aspects need to be performed. These studies can provide a better understanding on the influence of these parameters on the interzonal air and moisture transport through horizontal openings for cases with mixed ventilation; and therefore can lead to more general empirical equations for the interzonal mass airflow.

- One of the major successes of the IEA Annex 41, *Whole Building Heat, Air and Moisture Performance*, was the validation of several whole-building HAM models. These models were extensively and successfully validated with experimental data in terms of predicting the indoor humidity variations. However, it may be noted the validation of these models was carried out for single rooms only where interzonal HAM transfer was absent. The absence of interzonal HAM transfer in the validated whole-building HAM models is a consequence from the fact that these models evolved from HAM transfer models focused on the hygrothermal performance of the envelope, thus the interzonal moisture did not play any role. However, in reality, buildings consist of several rooms and interzonal moisture exchange occurs through large internal openings (e.g. doorways, staircase openings). Therefore, one-room whole-building HAM models need to evolve to include more zones and to include interzonal air and moisture flows. Also, whole-building HAM models that already allow modeling multizone buildings (e.g. BSim) need to be validated in terms of the prediction of indoor humidity in all zones.

REFERENCES

Allard, F. and Utsumi, Y. (1992) Airflow through large openings. *Energy and Buildings*, 18(2), 133-145.

Arundel, A.V., Sterling, E.M., Biggin, J.H. and Sterling, T.D. (1986) Indirect health effects of relative humidity in indoor environments. *Environmental Health Perspectives*, 65, 351-356.

ASHRAE (2004) Thermal environmental conditions for human occupancy. ANSI/ASHRAE Standard 55-2004. American Society of Heating, Refrigerating and Air-Conditioning Engineers, Atlanta.

ASHRAE (2005) Handbook Fundamentals. American Society of Heating, Refrigerating and Air-Conditioning Engineers, Atlanta.

Axley, J. and Nielsen, P. (2008) Modeling of ventilation airflow. Ventilation Systems: Design and performance, ed. H. Awbi, Taylor&Francis, London, 155-263.

Barakat, S.A. (1987) Inter-zone convective heat transfer in buildings: A review. *Journal of Solar Energy Engineering Transactions of the ASME*, 109(2), 71-78.

Berglund, L.G. and Cunningham, D.J. (1986) Parameters of human discomfort in warm environments. *ASHRAE Transactions*, 92(2B), 732-746.

Blomqvist, C. and Sandberg, M. (2004) Air movements through horizontal openings in buildings – A model study. *International Journal of Ventilation*, 3(1), 1-10.

Bornehag, C.G., Blomquist, G., Gyntelberg, F., Järvholm, B., Malmberg, P., Nordvall, L., Nielsen, A., Pershagen, G. and Sundell, J. (2001) Dampness in building and health. *Indoor Air*, 11(2), 72-86.

Bornehag, C.G., Sundell, J., Bonini, S., Custovic, A., Malmberg, P., Skerfving, P., Sigsgaard, T. and Verhoeff, A. (2004) Dampness in building as a risk factor for health effect. *Indoor Air*, 14 (4), 243-257.

Brown, W.G. (1962) Natural convection through rectangular openings in partitions-2: Horizontal openings. *International Journal of Heat and Mass Transfer*, 5(9), 869-881.

Brown, W.G. and Solvason, K.R. (1962) Natural convection through rectangular openings in partitions-1: Vertical openings. *International Journal of Heat and Mass Transfer*, 5(9), 859-868.

Burch, D.M. and Chi, J. (1997) MOIST: A PC program for predicting heat and moisture transfer in building tnvelopes. NIST Special Publication 917. Available on-line at: http://fire.nist.gov/fire/firedocs/build97/art005.html on August 2007.

Chen, Q. and Xu, W. (1998) A zero-equation turbulence model for indoor airflow simulations. *Energy and Buildings*, 28(2), 137-144.

Chen, Q. and Srebric, J. (2001) How to verify, validate, and report indoor environment modeling CFD analyses. ASHRAE RP-1133, American Society of Heating, Refrigerating and Air-Conditioning Engineers, Atlanta.

Chen, Q., and Zhai, Z. (2004). The use of CFD tools for indoor environmental design. Advanced Building Simulation, eds. A. Malkawi and G. Augenbroe. New York: Spon Press, 119–140.

Chen, X., Zhao, B. and Li, X. (2005) Numerical investigation on the influence of contaminant source location, occupant distribution and air distribution on emergency ventilation strategy. Indoor and Built Environment, 14(6), 455-467.

Cunningham, M.J. (1992) Effective penetration depth and effective resistance in moisture transfer. Building and Environment, 27(3), 379-386.

Davidson, L., Nielsen, P.V. and Sveningsson, A. (2003) Modification of the $\overline{v^2} - f$ model for computing flow in 3D wall jet. Turbulence, Heat and Mass Transfer, 4, 577-584.

Davies, M., Ucci, M., McCarthy, M., Oreszczyn, T., Ridley, I., Mumovic, D., Singh, J. and Pretlove, S. (2004) A review of evidence linking ventilation rates in dwellings and respiratory health - A focus on house dust mites and mould. International Journal of Ventilation, 3(2), 155-168.

ECBCS (2008) Annex 41: Whole building heat, air and moisture response (MOIST-ENG). Available online at www.kuleuven.ac.be/bwf/projects/annex41/index.htm on December 2008.

El Diasty, R., Fazio, P. and Budaiwi, I. (1993) The dynamic modelling of air humidity behaviour in a multi-zone space. Building and Environment, 28(1), 33-51.

Epstein, M. (1988) Buoyancy-driven exchange flow through small openings in horizontal partitions. Trans. of the ASME, Journal of Heat Transfer, 110(4), 885- 892.

Ergin-Özkan, S., Morhtarzadeh-Dehghan, M.R. and Reynolds, A.J. (1995) Experimental study of natural convection between two compartments of a stairwell. International Journal of Heat and Mass Transfer, 38(12), 2159-2168.

Fang, L., Clausen, G. and Fanger, P.O. (1998a) Impact of temperature and humidity on perception of indoor air quality. Indoor Air, 8(2), 80-90.

Fang, L., Clausen, G. and Fanger, P.O. (1998b) Impact of temperature and humidity on perception of indoor air quality during immediate and longer whole-building exposure. Indoor Air, 8(4), 276-284.

Fazio, P., Athienitis, A., Marsh, C. and Rao, J. (1997) Environmental chamber for investigation of building envelope performance. Journal of Architectural Engineering, 3(2), 97-102.

Fazio, P., Vera, S., Rao, J., Yang, X. and Ge, H. (2008a) Common exercise 6 – Datasets of WBHAM and indoor conditions for single room and two-room setups.

Modelling principles and common exercises, eds. M. Woloszyn and C. Rode. IEA Annex 41 Whole Building Heat, Air and Moisture Response, 201-214.

Fazio, P., Vera, S., Rao, J., Yang, X. and Ge, H. (2008b) Datasets of WBHAM and indoor conditions for single room and two-room setups. Final Report (DVD format). Modelling principles and common exercises, IEA Annex 41 Whole Building Heat, Air and Moisture Response, 212 p.

Ferziger, J.H. and Perić, M. (2002) Computational method for fluid dynamics. 3rd Edition, Springer, 2002.

Finch, G. (2007) The performance of rainscreen walls in coastal British Columbia. M.Sc. Thesis, Department of Civil Engineering, University of Waterloo.

Fluent (2007) Airpak 3.0 User's guide. Fluent, Inc. Lebanon, NH, United States.

Green, G.H. (1982) Positive and negative effects of building humidification. *ASHRAE Transactions*, 88(1), 1049-1061 (cited in ASHRAE 2005).

Haghentoft, C.E. (2002) HAMSTAD – WP2 Modeling, Version 4. Report R-02:9. Gothenburg, Department of Building Physics, Chalmers University of Technology.

Hens, H. (1991) (ed.) Sourcebook. Volume 1 of Annex 14 Energy and Condensation. Energy Conservation in Buildings and Community Systems, 337 p.

Hens, H. (1996) Modelling – Final Report. Volume 1 (Part 1) of Annex 24 Heat, Air and Moisture Transfer in Insulated Envelope Parts. Energy Conservation in Buildings and Community Systems, 90 p.

Hens, H. (2005) Impact of hygric inertia on indoor climate: simple models. Paper A41-T1-B-06-3. IEA Annex 41 Whole Building Heat, Air and Moisture Response (MOIST-ENG), Workshop meeting Trondheim (Sweden), October 26-28.

Hohota, R.S. (2003) Modélisation de l'humidité dans un code CFD (basses vitesses en grande cavité): Comparaison avec l'expérimental. Ph.D. Thesis. CETHIL-INSA de Lyon, France.

Holm, A., Kuenzel, H.M. and Sedlbauer, K. (2003) The hygrothermal behaviour of rooms: Combining thermal building simulation and hygrothermal envelope calculations. Eight International IBPSA Conference, Eindhoven, Netherlands, 499-505.

Holm, A. (2008) Applications: Indoor environments, energy, durability. Volume 4 of Annex 41 Whole Building Heat, Air and Moisture Response. Energy Conservation in Buildings and Community Systems, 177 p.

Huang, J.M., Chen, Q., Ribot, B. and Rivoalen, H. (2004) Modelling contaminant exposure in a single-family house. *Indoor and Built Environment*, 13(1), 5-19.

HUD (2004) Building moisture and durability. Past, present and future work. U.S. Department of Housing and Urban Development, Office of Policy Developments and Research, Washington, DC.

Hukka, A. and Viitanen, H.A. (1999) A mathematical model of mould growth on wooden material. *Wood Science and Technology*, 33(6), 475-485.

Kalamees, T., Vinha, J. and Kurntiski, J. (2006) Indoor humidity loads and moisture production in lightweight timber-frame detached houses. *Journal of Building Physics*, 29(3), 219-246.

Kohal, J.S. (1995) Airflow through horizontal openings. Ph.D. Thesis. University of Nottingham, Institute of Building Technology.

Kolokotroni, M., Saiz, N. and Litter, J. (1992) Moisture movement: A study using tracer gas technique and CFD modeling. *Building Services Engineering Research and Technology*, 13, 113-117.

Klobut, K. and Sirén, K. (1994) Experimental investigation of air flows through large openings in a horizontal partition. Report B35. Helsinki University of Technology. Laboratory of Heating, Ventilating and Air-Conditioning.

Kuenzel, H.M., Karagiozis, A.N. and Holm. A.H. (2001) Chapter 9: A hygrothermal design tool for architects and engineers (WUFI ORNL/IBP). Moisture Analysis and Condensation Control in Building Envelopes. ed. H. Treschel. ASTM, Philadelphia.

Janssen, A. and Vandepitte, A. (2006) Analysis of indoor climate measurements in recently built Belgian dwellings. Paper A41-T3-B-06-10. IEA Annex 41 Whole Building Heat, Air and Moisture Response (MOIST-ENG), Workshop meeting Lyon (France), October 25-27.

Launder, B.E. and Spalding, D.B. (1974) The numerical computation of turbulent flows. *Computer Methods in Applied Mechanics and Energy*, 3(2), 269-289.

Li, Z. (2007) Characteristics of buoyancy driven natural ventilation through horizontal openings. Ph.D. Thesis. Department of Civil Engineering Architectural Engineering. Aalborg University, Denmark.

Liu, J., Aizawa, H. and Yoshino, H. (2002) Experimental and numerical study on simultaneous temperature and humidity distribution. Proceedings of Roomvent'02, Eight International Conference of Air Distribution in Rooms, Copenhagen, Denmark, 168-172.

Liu, J., Aizawa, H. and Yoshino, H. (2004) CFD Prediction of surface condensation on walls and its experimental validation. *Building and Environment*, 39(8), 905-911.

Maref, W., Lacasse, M.A. and Booth, D. (2003) An approach to validating computational models for hygrothermal analysis-full-scale experiments. Available on-line at http://irc.nrc-cnrc.gc/ircpubs on August 2007.

Melikov, A.K., Madsen, T.L. and Langkilde, G. (1998) Impact of velocity and temperature fluctuations on the accuracy of low-velocity measurements indoors by thermal anemometers. *ASHRAE Transactions*, 104(1B), 1519-1528.

Melikov, A.K., Popiolek, Z, Silva, M.C.G., Care, I. and Seftker, T. (2007) Accuracy limitations for low-velocity measurements and draft assessment in rooms. *HVAC&Research*, 13(6), 971-986.

Mendes, N., Oliveira, C.L.F. and dos Santos, G.H. (2003) DOMUS 2.0: A whole-building hygrothermal simulation program. Eight International IBPSA Conference, Eindhoven, Netherlands, 863-870.

Merrill, J.L. and TenWolde, A. (1989) Overview of moisture-related damage in one group of Wisconsin manufactured homes. *ASHRAE Transactions*, 95(1), 405-414.

Miller, S.L., Leiserson, K. and Nazaroff, W.W. (1997) Non-linear least-square minimization applied to tracer gas decay for determining airflow rates in a two-zone building. *Indoor Air*, 7(1), 64-75.

Mokhtarzadeh-Dehghan, M.R., Ergin- Özkan, S. and Reynolds, A.J. (1995) Natural convection between two compartments of a stairwell numerical prediction and comparison with experiment, *Numerical Heat Transfer, Part A*, 27(1), 1–17.

Morhtarzadeh-Dehghan, M.R. (2007) Natural convection between two floors of a building via a horizontal opening – Measurements in a one-half scale model. *International Journal of Heat and Mass Transfer*, 50(15-16), 3141-3151.

Morrison, B.I. 2000. The adaptive coupling of heat and air flow modeling within dynamic whole-building simulation. Ph.D. Thesis, University of Strathclyde, Glasgow, UK.

Mortensen, L.H., Woloszyn, M., Rode, C. and Peuhkuri, R. (2007) Investigation of microclimates by CFD modeling of moisture interaction between air and constructions. *Journal of Building Physics*, 30(4), 279-315.

Nicholas, J.V. and White, D.R. (2001) Traceable temperatures. John Wiley & Sons, Ltd.

Nielsen, P.V. (1974). Flow in air-conditioned rooms. Ph.D. Thesis, Technical University of Denmark, Copenhagen. Denmark (cited in Zhai et al., 2007).

Oldengarm, J. and de Gids, W. F. (1991) Field experiments on airborne moisture transport. *Air Infiltration Review*, 12(2), 8-11.

Oreszczyn, T., Ridley, I., Hon, S.H., Wilkinson, P. and Warm Front Study Group (2006) Mould and winter indoor relative humidity in low income households in England. *Indoor and Built Environment*, 15(2), 125-135.

Padfield, T. (1998) The role of absorbent material in moderating changes of relative humidity. Ph.D. Thesis. Department of Structural Engineering and Materials. Technical University of Denmark.

Patankar, S.V. (1980) Numerical heat transfer and fluid flow. Series in Computational Methods in Mechanics and Thermal Sciences, Taylor&Francis.

Peppes, A.A., Santamouris, M. and Asimakopoulos, D.N. (2001) Buoyancy-driven flow through a stairwell. *Building and Environment*, 36(2), 167-180.

Peppes, A.A., Santamouris, M. and Asimakopoulos, D.N. (2002) Experimental study of buoyancy-driven stairwell flow in a three storey building. *Building and Environment*, 37(5), 497-506.

Plathner, P. and Woloszyn, M. (2002) Interzonal air and moisture transport in a test house: Experiment and modelling. *Building and Environment*, 37(2), 189-199.

Popiolek, Z., Joergensen, F.E., Melikov, A.K., Silva, M.C.G. and Kierat, W. (2007) Assessment of uncertainty in measurement with low velocity thermal anemometers. *Journal of Ventilation*, 6(2), 113–26.

Reinikainen, L.M., Jaakkola, J.J.K. and Heinonen, O.P. (1991) The effect of air humidification on different symptoms in office workers – An epidemiologic study. *Environment International*, 17(4), 243-250.

Ridley, I., Davies, M., Hong, S.H., Oreszcyn, T., Warm Front Study Group (2007) Vapour pressure excess in living rooms and bedrooms of English dwellings: Analysis of the Warm Front Dataset. Paper A41-T3-UK-07-1. IEA Annex 41 Whole Building Heat, Air and Moisture Response (MOIST-ENG), Workshop meeting Florianópolis (Brazil), April 16-18.

Riffat, S.B. (1989) Measurement of heat and mass transfer between the lower and upper floors of a house. *International Journal of Energy Research*, 13(2), 231-241.

Riffat, S.B. and Kohal, J.S. (1994) Experimental study of interzonal natural convection through and aperture. *Applied Energy*, 48(3), 305-313.

Riffat, S.B., Kohal, J.S. and Shao, L. (1994) Measurement and CFD modeling of buoyancy-driven flows in horizontal openings. In *Proceedings of IAQ'94: Engineering Indoor Environments*. American Society of Heating, Refrigerating and Air-Conditioning, Atlanta, 159-166.

Riffat, S.B. and Shao, L. (1995) Characteristics of buoyancy-driven interzonal airflow via horizontal openings. *Building Services and Engineering Research Technology*, 16(3), 149-152.

Rode, C. (1990) Combined heat and moisture transfer in building constructions. Ph.D. Thesis. Technical University of Denmark.

Rode, C. and Grau, K. (2003) Whole building hygrothermal simulation model. *ASHRAE Transactions*, 109(1), 572-582.

Salonvaara, M. and Kariagozis, A. (1994) Hygrothermal behaviour of a brick wall; parametric study on material properties using stochastic modeling. International Energy Agency, Annex 24. Internal report T1-CA-94/3.

Sanders, C. (1996) Environmental conditions – Final Report. Volume 2 of Annex 24 Heat, Air and Moisture Transfer in Insulated Envelope Parts. Energy Conservation in Buildings and Community Systems, 96 p.

Sandwell, D.T. (1987) Biharmonic spline interpolation of GEOS-3 and SEASAT altimeter data, *Geophysical Research Letters*, 14(2), 139-142.

Santamouris, M., Argiriou, A., Asimakopoulos, D., Klitsikas, N. and Dounis, A. (1995) Heat and mass transfer through large openings by natural convection. *Energy and Buildings*, 23(1), 1-8.

Shaw, B.H. (1972) Heat and mass transfer by natural convection and combined natural convection and forced air flow through large rectangular openings in a vertical partition. Symposium on Heat and Mass Transfer by Combined Forced and Natural Convection, Manchester, UK, Vols. 18-19, 31-39.

Shaw, B.H. and White, W. (1974) Air movement through doorways: the influence of temperature and its control by forced airflow. *Building Services Engineer*, 42, 210-218.

Shi, X., Johnson, P. and Burnett, E. (2007) Uncertainty analysis for vapor pressure measurement. *Journal of Building Physics*, 30(4), 317-336.

Shih, T., Liou, W., Shabbir, A., Yang, Z. and Zhu, J. (1995) A new k-ε eddy viscosity model for high Reynolds number turbulent flows. *Computers&Fluids*, 24(3), 227-238.

Simonson, C.J. (2000) Moisture, thermal and ventilation performance of Tapanila ecological house. VTT Research Notes, Technical Research Centre of Finland. ESPOO.

Sørensen, D.N. and Nielsen, P.V. (2003) Quality control of computational fluid dynamics in indoor environments. *Indoor Air*, 13(1), 2-17.

Srebric, J. (2000) Simplified methodology for indoor environment design. Ph.D. Thesis. Department of Architecture, Massachusetts Institute of Technology, MA, United States.

Srebric, J., Chen, Q. and Glicksman, L.R. (1999) Validation of a zero-equation turbulence model for complex indoor airflow simulation. *ASHRAE Transactions*, 105(2), 414-427.

Steeman, H.J., Janssens, A., Carmeliet, J. and De Paepe, M. (2008) Modelling indoor air and hygrothermal wall interaction in building simulation: Comparison between CFD and a well-mixed zonal model. *Building and Environment*, 44(3),572-583

Taylor, B.N. and Kuyatt, C.E. (1994) Guidelines for evaluating and expressing the uncertainty of NIST measurement results. NIST Technical Note 1297, 26 p.

TenWolde, A. (1994) Ventilation, humidity, and condensation in manufactured houses during winter. *ASHRAE Transactions*, 100(1), 103-115.

Teodosiu, C., Hohota, R., Rusaou, G. and Woloszyn, M. (2003) Numerical prediction of indoor air humidity and its effect on indoor environment. *Building and Environment*, 38(5), 655-664.

Toftum, J., Jorgensen, A.S. and Fanger, P.O. (1998) Upper limits of air humidity for preventing warm respiratory discomfort. *Energy and Buildings*, 28(1), 15-23.

Trechsel, H. (ed) (1994) Moisture control in buildings. ASTM, Philadelphia.

Treschel, H. (ed.) (2001) Moisture analysis and condensation control in building envelopes. ASTM, Philadelphia.

Tscuchiya, T. (1980) Infiltration and indoor air temperature and moisture variation in a detached residence. *Journal of the Society of Heating, Air-Conditioning and Sanitary Engineers of Japan*, 54(11), 13-19.

van der Mass, J. (ed.) (1992) Air flow through large openings in buildings. Subtask 2. Annex 20, Air Flow Patterns within Buildings. Energy Conservation in Buildings and Community Systems, 163 p.

Veersteg, H.K and Malalasekera, (1995) An introduction to Computational Fluid Dynamics: The finite volume method approach. Pearson Education Limited.

Vera, S., Yang, X., Rao, J., Ge, H. and Fazio, P. (2007). Moisture interaction between the building envelope and indoor environment: Experimental setup and preliminary results. 12th Symposium for Building Physics, March 29-31, Dresden, Germany, Vol. 2, 955-962.

Vera, S., Fazio, P. and Rao, J. (2009) Estimation of interzonal mass airflows through a large horizontal opening in a full-scale two-story test-hut with forced and buoyancy driven flows. Accepted to be published in the 4th International Building Conference, June 15-18, Istanbul, Turkey.

Woloszyn, M. (1999) Modélisation hygro-thermo-aéraulique des bâtiments multizones: proposition d'une stratégie de résolution du système couple. Ph.D. Thesis, INSA-CETHIL, Lyon, France.

Woloszyn, M. and Rode, C. (2008) Modelling principles and common exercises. Volume 1 of Annex 41 Whole Building Heat, Air and Moisture Response. Energy Conservation in Buildings and Community Systems, 234 p.

Xu, W. and Chen, Q. (2000) Simulation of mixed convection flow in a room with a two-layer turbulence model. *Indoor Air*, 10(4), 306-314.

Yakhot, V. and Horzag, S.A. (1986) Renormalization group analysis of turbulence: I. Basic Theory. *Journal of Scientific Computing*, 1(1), 3-51.

Yang, X., Vera, S., Rao, J., Ge. H, and Fazio, P. (2007) Full-scale experimental investigation of moisture buffering effect and indoor moisture distribution. In CD of *Thermal Performance of the Exterior Envelopes of the Whole Building, X International Conference*, Florida, 8 p.

Zhai, Z. (2006) Application of Computational Fluid Dynamics in building design: Aspects and trends. *Indoor and Built Environment*, 15(4), 305-314.

Zhai, Z., Zhang, Z., Zhang, W. and Chen, Q. (2007) Evaluation of various turbulence models in predicting airflow and turbulence in enclosed environments by CFD: Part I – Summary of prevalent turbulence models. *HVAC&Research*, 13(6), 853-870.

Zhang, Z., Zhang, W., Zhai, Z. and Chen, Q. (2007) Evaluation of various turbulence models in predicting airflow and turbulence in enclosed environments by CFD: Part 2 – Comparison with experimental data from literature. *HVAC&Research*, 13(6), 871-886.

Zhou, L. (2007) Optimization of ventilation system design and operation in office environments. Ph.D. Thesis, Department of Building, Civil and Environmental Engineering, Concordia University, Montreal, Canada.

Zohrabian, A.S., Morhtarzadeh-Dehghan, M.R. and Reynolds, A.J. (1988) A numerical study of buoyancy-driven flows of mass and energy in a stairwell. 9th AIVC Conference, Gent, Belgium, 12-15 September, 183-204.

Zohrabian, A.S., Morhtarzadeh-Dehghan, M.R., Reynolds, A.J. and Marriott, B.S.T. (1989) An experimental study of buoyancy-driven flow in a half-scale stairwell model. *Building and Environment*, 24(2), 141-148.

APPENDIX A: UNCERTAINTY OF PARTIAL VAPOR PRESSURE

This Appendix shows the calculation of the standard uncertainty of the humidity ratio. The procedure shown below is bases on the guidelines given by Taylor and Kuyatt (1994), Nicholas and White (2001) and Shi et al. (2007).

Humidity ratio, w, is a function of the partial vapor pressure, p_v (Pa), as shown in Eq. A.1. Partial vapor pressure depends on RH and the saturated vapor pressure, p_{sat} (Pa), as given by Eq. A.2; and finally, the saturation vapor pressure is a function of the temperature according to Eqs. A.3 and A.4.

$$w = 0.62198 \cdot \frac{p_v}{P - p_v} \tag{A.1}$$

$$p_v = p_{sat} \cdot RH \tag{A.2}$$

$$p_{sat} = e^{f(T)} \tag{A.3}$$

$$f(T) = \frac{C_1}{T} + C_2 + C_3 \cdot T + C_4 \cdot T^2 + C_5 \cdot T^3 + C_6 \cdot \ln(T) \tag{A.4}$$

where P (Pa) is the atmospheric pressure and is equal to 101,325 Pa at sea level; T is the air temperature (°K); and constants $C_1 = $ -5.800220x10^3, $C_2 = $ 1.3914993, $C_3 = $ -4.8640239x10^{-2}, $C_4 = $ 4.1764768x10^{-5}, $C_5 = $ -1.4452093x10^{-8}, and $C_6 = $ 6.5459673.

Since the humidity ratio depends on p_v, p_{sat}, RH and $f(T)$, the uncertainty of the humidity ratio should be inferred from the uncertainties of these quantities. Moreover the uncertainties of p_v, p_{sat} and $f(T)$ should be calculated the uncertainty propagation equation as follows:

$$y = f(x_1, x_2, \dots, x_N), \tag{A.5}$$

$$u_c^2(y) = \sum_{i=1}^{N} \left(\frac{\partial f}{\partial x_i}\right)^2 u^2(x_i) \tag{A.6}$$

The values measured by the RH probes are temperature and RH, which varied among the cases and locations across the test-hut. Here, the combined standard uncertainty of the humidity ratio is calculated for the steady-state average indoor air conditions at the end of the moisture generation period, T = 293.15°K and RH = 60%. Replacing these temperature and RH in Eqs. A.1 to A.4, p_{sat} is 2,338.8 Pa, p_v is 1,403.3 Pa, and w is 8.735 g/kg. The accuracies for T and RH are obtained from Table 4.2. These values correspond to the normal distribution and 95% level of confidence, thus the standard uncertainty (68% level of confidence) for temperature (u_T) is 0.5/1.96 = 0.255°C, while the standard uncertainty of RH (u_{RH}) is 0.02/1.96 = 0.0102. Based on Eq. A.6 and the standard uncertainties of the T and RH, the individual uncertainties of $f(T)$, p_{sat} and p_v are calculated below.

$$u_{f(T)} = \left(\frac{\partial f(T)}{\partial T}\right) u_T = 0.0158 \tag{A.7}$$

$$u_{p_{sat}} = e^{f(T)} u_{f(T)} = 36.95 \; Pa \tag{A.8}$$

$$u_{p_v} = \sqrt{(p_{sat})^2 u_{RH}^2 + (RH)^2 u_{p_{sat}}^2} = 32.5 \; Pa \tag{A.9}$$

Finally, the combined uncertainty of the humidity ratio is:

$$u_w = \left(\frac{\partial w}{\partial p_v}\right) u_{p_v} = 0.2 \; g/kg \tag{A.10}$$

APPENDIX B: WATER VAPOR MASS IMBALANCE IN THE TEST-HUT

An analysis found that the water vapor gains and losses were not completely balanced within and through the boundaries for the enclosure space formed by the test-hut, mechanical ventilation systems and interconnecting ducts. It was also found that this imbalance affect the accuracies of experimental results of the interzonal air and water vapor exchange through the horizontal opening. Although a solution was developed to alleviate this situation, the nature of the imbalance itself deserves examination.

The accumulated water vapor mass imbalance for the whole system over a measurement period of 10 hours, $I(10)$, may be calculated by:

$$I(10) = \begin{pmatrix} Total\ moisture \\ accumulated\ in \\ the\ test - hut \\ air\ volume \\ over\ 10h \end{pmatrix} + \begin{pmatrix} Total \\ moisture \\ leaving\ the \\ test - hut \\ over\ 10h \end{pmatrix} - \begin{pmatrix} Total \\ moisture \\ entering\ the \\ test - hut \\ over\ 10h \end{pmatrix} \quad (B.1)$$

The water vapor imbalance may be caused by:

- Measurement errors of humidity ratios for the room air volume, supply air, exhaust air, and environmental chamber, ventilation airflow rates and moisture generation rates;

- Estimation errors of air leakage; and

- Non-well mixed air conditions within each room.

The relative difference between the measured upward mass airflows using the set of mass balance equations for the lower room (Eqs. 5.3 and 5.5) and the set of mass balance equations for upper room (Eqs. 5.4 and 5.6) may be expresses as:

$$\Delta F_{12} = 100 \frac{|F_{12}^{5.3\&5.5} - F_{12}^{5.4\&5.6}|}{min(F_{12}^{5.3\&5.5},\ F_{12}^{5.4\&5.6})} \quad (B.2)$$

Figure B.1 plots the relative difference of the measured upward mass airflow and the accumulated water vapor mass imbalance. It can be observed that the two quantities are correlated. It can be seen that the relative differences in the calculated upward mass airflows are proportional to the magnitude of the accumulated water vapor mass imbalance. The relative differences are between 0.6% and 11.7% for the upward mass airflow (F_{12}). The linear least square fitting indicates that the moisture imbalance is the cause of 63% of the relative differences in F_{12} estimations. Similar results were found for the measured upward mass airflows (F_{21}).
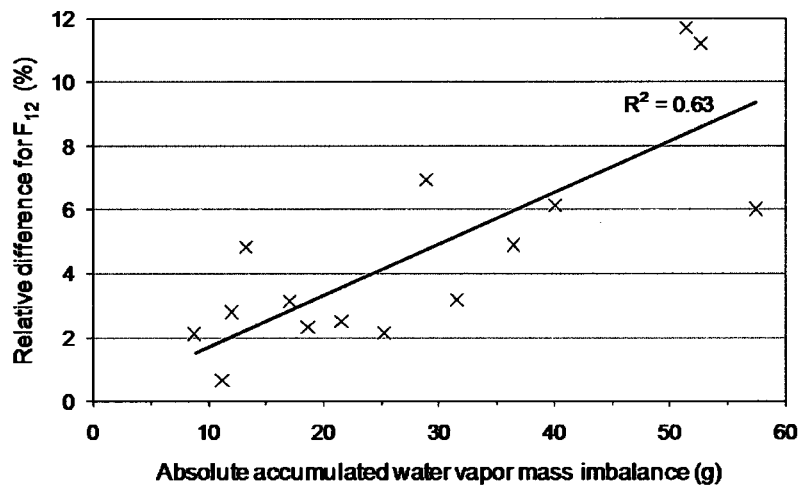
Figure B.1: Relationship between the water vapor mass imbalance and the measured upward mass airflows (Vera et al., 2009).

APPENDIX C: EXPERIMENTAL DATA USED AS INPUT DATA FOR THE VALIDATION OF THE CFD MODEL

This appendix includes tables with the experimental data of cases that were used as input data for the CFD simulations for validating the CFD model.

Table C1: Experimental test conditions for cases in scenario II at 0.5 ACH

Parameters	Case 2-1	Case 2-2	Case 2-3	Case 2-4	Case 2-5
ΔT (°C)	-3.5	-2.7	-1.6	-0.2	+0.7
Moisture generation (g/h)	109.4	109.4	109.4	109.4	109.1
Supply air condition:					
Inlet airflow rate (l/s)	5.920	5.929	5.905	5.896	5.932
Inlet temperature (°C)	17.9	18.0	18.0	18.0	18.3
Inlet humidity ratio (g/kg)	4.95	4.91	4.96	4.96	4.84
Heat sources:					
Hotplate (W)	85	85	85	85	85
Baseboard heater 1 (W)	376	274	252	153	129
Baseboard heater 2 (W)	0	0	91	175	243
Wall surface temperatures[1] - lower room (°C):					
North wall	22.2	20.5	20.3	20.1	20.0
East wall	20.6	18.8	18.8	18.9	19.1
South wall	20.2	18.4	18.6	18.3	18.7
West wall	20.4	18.7	18.7	18.7	18.9
Ground floor	19.6	18.1	18.2	17.9	18.1
Ceiling	23.2	21.2	21.1	21.0	21.1
Wall surface temperatures[1] – upper room (°C):					
North wall	17.0	16.6	16.5	19.3	20.2
East wall	17.3	16.2	17.2	18.5	19.3
South wall	17.1	15.6	16.7	18.0	19.5
West wall	17.3	16.2	17.3	18.5	19.4
Floor	17.9	16.9	17.8	18.9	18.7
Ceiling	17.8	16.8	18.0	19.7	20.6

[1] For simplicity, average temperatures are shown in this table, but measured temperatures distributed along each surface were in fact specified in Airpak.

Table C2: Experimental test conditions for cases in scenario II at 0.75 ACH

Parameters	Case 2-5	Case 2-6	Case 2-7
ΔT (°C)	-2.5	+0.4	+1.3
Moisture generation (g/h)	108.7	108.4	108.6
Supply air condition:			
Inlet airflow rate (l/s)	8.936	8.970	8.932
Inlet temperature (°C)	18.0	18.8	18.0
Inlet humidity ratio (g/kg)	4.916	4.939	4.923
Heat sources:			
Hotplate (W)	85	85	85
Baseboard heater 1 (W)	283	102	112
Baseboard heater 2 (W)	0	185	274
Wall surface temperatures[1] - lower room (°C):			
North wall	19.3	19.5	19.5
East wall	18.2	18.5	18.5
South wall	17.8	18.2	18.2
West wall	18.2	18.5	18.5
Ground floor	17.4	17.2	17.3
Ceiling	20.3	20.5	20.5
Wall surface temperatures[1] – upper room (°C):			
North wall	15.5	18.7	19.6
East wall	15.6	18.1	19.5
South wall	15.2	17.1	19.3
West wall	15.6	18.6	19.4
Floor	16.0	18.8	19.3
Ceiling	16.3	20.0	21.0

[1] For simplicity, average temperatures are shown in this table, but measured temperatures distributed along each surface were in fact specified in Airpak.

Table C3: Experimental test conditions for cases in scenario IV at 0.5 ACH

Parameters	Case 4-1	Case 4-2	Case 4-3	Case 4-4
ΔT (°C)	-1.5	-0.2	+0.8	+2.7
Moisture generation (g/h)	109.4	109.6	105.7	106.5
Supply air condition – inlet lower room:				
Inlet airflow rate (l/s)	3.290	3.295	3.307	3.319
Inlet temperature (°C)	17.8	18.2	17.9	18.2
Inlet humidity ratio (g/kg)	4.820	4.839	4.897	4.909
Supply air condition – inlet upper room:				
Inlet airflow rate (l/s)	2.951	2.88	2.880	2.903
Inlet temperature (°C)	18.0	17.9	18.9	18.0
Inlet humidity ratio (g/kg)	4.9932	5.007	4.782	4.933
Heat sources:				
Hotplate (W)	85	85	85	85
Baseboard heater 1 (W)	175	143	129	120
Baseboard heater 2 (W)	90	166	243	270
Wall surface temperatures[1] - lower room (°C):				
North wall	20.1	20.0	19.0	19.5
East wall	18.8	18.8	18.8	19.0
South wall	18.3	18.3	18.4	18.4
West wall	18.6	18.7	18.7	18.8
Ground floor	17.9	17.9	18.0	18.0
Ceiling	20.9	20.8	20.8	21.0
Wall surface temperatures[1] – upper room (°C):				
North wall	17.8	19.2	20.5	22.3
East wall	17.2	18.4	19.3	21.0
South wall	16.4	17.6	18.6	20.7
West wall	17.2	18.4	19.4	21.0
Floor	17.6	18.6	20.4	21.8
Ceiling	17.9	19.6	20.7	22.8

[1] For simplicity, average temperatures are shown in this table, but measured temperatures distributed along each surface were in fact specified in Airpak.